HAL
open science

Dispositif expérimental pour la diffusion Compton virtuelle dans le régime profondément inélastique dans le Hall A au Jefferson Laboratory

A. Camsonne

To cite this version:

A. Camsonne. Dispositif expérimental pour la diffusion Compton virtuelle dans le régime profondément inélastique dans le Hall A au Jefferson Laboratory. Chimie-Physique [physics.chem-ph]. Université Blaise Pascal - Clermont-Ferrand II, 2005. Français. NNT : 2005CLF21606 . tel-00683591

HAL Id: tel-00683591

https://theses.hal.science/tel-00683591v1

Submitted on 29 Mar 2012

HAL is a multi-disciplinary open access archive for the deposit and dissemination of scientific research documents, whether they are published or not. The documents may come from teaching and research institutions in France or abroad, or from public or private research centers.

L'archive ouverte pluridisciplinaire **HAL**, est destinée au dépôt et à la diffusion de documents scientifiques de niveau recherche, publiés ou non, émanant des établissements d'enseignement et de recherche français ou étrangers, des laboratoires publics ou privés.

Numéro d'ordre : DU 1606 PCCF T0507
EDSF : 462

UNIVERSITE BLAISE PASCAL
(U.F.R. de Recherche Scientifique et Technique)

ECOLE DOCTORALE DES SCIENCES FONDAMENTALES

THESE

présentée pour obtenir le grade de

DOCTEUR D'UNIVERSITE

SPECIALITE: PHYSIQUE CORPUSCULAIRE

par

Alexandre CAMSONNE
Maître ès-Sciences, Diplômé d'Etudes Approfondies

Experimental setup for Deeply Virtual Compton Scattering (DVCS) experiment in Hall A at Jefferson Laboratory

Dispositif expérimental pour la Diffusion Compton Virtuelle dans le régime profondément inélastique dans le Hall A au Jefferson Laboratory

Soutenue publiquement le 4 novembre 2005, devant la commission d'examen:

Président :	M.	A.	BALDIT	
Examinateurs :				
	M.	K.	DE JAGER	Examinateur
	M.	F.	SABATIE	Examinateur
	M.	B.	MICHEL	Directeur de thèse
	M.	P.	GUICHON	Rapporteur
	M.	C.	HYDE WRIGHT	Rapporteur

Acknowledgements

This work takes its root to the simple questions every kid wonders at some point : what is matter made of and what is the force linking everything together. Being born in Caen about the same time when the Grand Accelerateur d'Ions Lourds (GANIL Large Heavy Ion Accelerator) was built certainly inspired me for my future. Indeed a way to to address these previous interrogations is well known to any kid : when you want to determine what is something made of you smash it and look at the small pieces which were part of it. That is in first approximation what is done in at an accelerator. I had heard about quarks in protons, neutrons and strong interaction pretty early. But going beyond those words proved to be difficult : protons, neutrons and radioactivity were mentioned in high school books but nucleon structure was simply not dealt with. Indeed much to my dismay but in some way that what makes it interesting the strong interaction, especially how the nucleon structure can be described in term of hadronic degrees of freedom still remains to be fully understood. The strong interaction has as main property the confinement which results in the impossibility to see free quarks in ordinary matter and thus to study them directly. The spin crisis proved that the nucleon is a complex relativistic system and that gluonic contributions and quarks orbital momentum had to be taken into account rather than a static system comparable to a nucleus. The nucleon still is something we need to look inside to understand it and for me detectors and accelerators are similar to building powerful microscopes to do so. This is what eventually lead me to the USA to work at Jefferson Laboratory, one of the laboratory dedicated to study strong interaction. I was lucky to have the opportunity to work on the first dedicated DVCS experiment. Oddly for me physics always meant experimental physics where one would do the experiment and draw conclusions from it. Compared to the larger ones this experiment had a smaller scale allowing to work the old fashioned way and to see it almost from the conception up to an almost final result. The subject was interesting and new equipment had to be built so conditions were ideal to learn about physics on both experimental side and theoretical sides. I always have been curious about Data Acquisition (DAQ) and electronics so I was happy to receive the responsibility for the integration of the LPC Clermont-

Ferrand custom electronics in the experiment. I had a lot to learn so I wish to thank the people who got me started on the DAQ namely Yves Roblin, Robert Michaels, David Abbott and Michel Brossard for their patience and availability. One could think that a physics thesis work would be a rather lonely task sitting behind his computer for hours, it actually sometimes is but this also a huge team work and I was lucky to get to interact with many people and whom I wish to thank for their help. Without them this experiment would not have been possible or as successful as it was. So here is the list of people to whom I wish to give credit, it is long but I will try not to forget anyone. Firstly I want to thank my jury members Kees De Jager, Franck Sabatie, Alain Baldit and the rapporteur Charles Hyde-Wright and Pierre Guichon. A special thank to the foreign members I was very honored to have them attending the thesis defense coming from so far. I also wish to thank people from Clermont-Ferrand :

- Jean-Francois Mathiot for accepting in the Clermont-Ferrand physics master which led to this thesis
- on the doctoral school side Pierre Henrard for the administrative organization Eliane Passemard for their help with this thesis which mostly took place away from France
- the LPC Clermont director Alain Baldit and former director Bernard Michel for allowing to be part the laboratory for this work, the LPC electronics division in particularly Eric Sahuc, Christian Fayard and Michel Brossard.
- the mechanical workshop Guy Savinel and François Daudon

Many other institutions and many people contributed to the experiment :

- The CEA Saclay designer Jean-Claude Saudemont for detector and mechanical structure design and his help site.
- On the other side of the Atlantic Ocean for the Hall A Jefferson Laboratory : the Hall A leader Kees de Jager for the trust he put into my work, Heather Ashley for handling all our administrative needs and Sirish Nanda as Jefferson Laboratory contact person for the experiment.
- The Hall A technical staff John (Jack 7242) Segal who keeps Hall A ticking and who always manage to have what is needed on hand. Ed Folts, Heidi Fansler, Scott Spiegel, Gary Dezern for their professionalism in setting up everything.
- The people of the data acquisition group Dave Abbott for all the support , Ed Jastrembski for the help with the hardware. My deepest thanks Robert

Michaels for postponing his vacations to be able to help me getting everything running before the experiment start.

- The Jefferson Laboratory designer team : Al Gavalya, Ravi Anumagalla, Joyce Miller and Susan Esp
- The Jefferson Laboratory workshop people Dave Mac Kay, Casse Appeldorn
- The Electronics Group Chris Cuevas, Fernando Barbosa, Jeff Wilson for their work on the gain monitoring system and gladly offering space and tools for testing our electronics

During my first years at Jefferson Laboratory, I was able to learn about Hall A by taking shifts on different experiment, so I wish to thank them for their time teaching me about Hall A, their experiments and for taking shifts later on the experiment :

- Helium 3 team, Jian-Ping Cheng, Xiaochao Zheng, Kevin Kramer, Vincent Sukolsky, Patricia Solvignon, Karl Slifer
- HAPPEX and Compton polarimeter team David Lhuillier, Antonin Vacheret, Brian Moffit, Lisa Kaufman
- Big Bite and Short Range Correlation collaboration Douglas Higginbotham, Peter Monaghan, Eli Piasetzky, Ramesh Subedi

and particularly the DVCS collaboration

- Old Dominion University Tom Hartlove, Gagik Gavalian, David Hayes for their work on the proton array
- the Rutgers University Kathleen Mc Cormick, Ronald Ransome the lead-fluoride calorimeter specialists.
- the DVCS core people : the spokepersons Franck Sabatie, Charles Hyde-Wright, Eric Voutier
- the DVCS graduate students Carlos Munoz (Mr DVCS analysis guru) , and neutron DVCS student Malek Mazzouz (Mr I have a question ...).
- a special thank you to my advisor Pierre Bertin who started all of this and gave me precious advices along with his trust all along these years getting ready for the experiment. His extraordinary enthusiasm for the experiment as and Physics in general even if officially retired during the experiment. I fully profited from his experience and his skills in whatever we worked on : physics analysis, detector tests, electronics and even drilling a hole or soldering.

- The DVCS summer students Astrid Chantelauze, Jean Marc Fieschi and Matthieu Beaumel for their help in the experiment setup.

All the Jefferson Laboratory community :

- My roommates Emmanuel Busato, Pierre Moussiegt, Issam Qattan, Peter Monaghan, Olivier Destin, Astrid Chantelauze for surviving a stay at my place. This were a great time for me.

- French institution colleagues from Grenoble : Serge Kox, Guillaume Batigne, Benoit Guillon, from Orsay : Michel Guidal, Hyonsuk Jo , Sylvain Bouchigny,Marion Mc Cormick, Dominique Marchand, Jason Lenoble. CEA Saclay Michel Garcon, Francois Xavier Girod. Some French "locals" :Alexandre Deur, Matthieu Guillo, Julie Roche, Yves Roblin, Frederic Bonnet, Olivier Gayou

- and the american locals : Paul King, Rikki Roché, Douglas Higginbotham, Marcy Sturzman, Joe Grames and many others I only know by face.

for maintaining a nice mood all around the place during all those years spent in Newport News.

The LPC graduate students for the many discussions about especially the DEA colleagues Xaviez Lopez, Geoffroy Guibert, Matthieu Petit, Sebastien Gadrat for their welcoming for the few days I spent back in France, also Sebastien Binet for the computer geek talks, Arnaud Robert my "Doctoriales" comrade, Fabien Courtine, Benjamin Labonne, Fabrice Tissandier, David Borras, Vincent Giangiobbe, Fabien Guerin : the doctors or soon to be doctors I wish them good luck for their graduation and post graduate work.

My family for all the support and understanding for these many years away from home. Now I understand how difficult it must have been for you but this was something I had to do.

Overall this extended stay in Newport News was pretty busy and a very good personal experience to get acquainted with another lifestyle and culture. I guess the only regrets I have are that I was not able to work on all the aspects of the experiment but in order to finish it in a timely manner work has to be split among people so I had to let the simulation part and most of the analysis software development and the spectrometer analysis but hopefully those skills can be practiced later and we managed to get a preliminary result with the data we took for the π^0 electroproduction. In more I mostly worked on getting the experiment to run and I am very grateful that people trusted me to give me such big responsibilities. To conclude these already too long acknowledgments, I will say that this thesis and this experiment is a kid dream come true proving that with perseverance a lot of things can become possible.

Résumé en français

Bien que l'interaction forte qui gouverne la structure interne des nucléons, semble pouvoir être décrite par la Chromo-dynamique Quantique (QCD). Certaines de ses propriétés restent incomprises. En effet sa principale caractéristique est le confinement : expérimentalement les constituants des hadrons, les quarks n'ont pu être observés à l'état libre. Ce qui se traduit pour QCD par une valeur de la constante de couplage de l'interaction qui varie selon la distance d'interaction : celle-ci croît rapidement avec la distance empêchant en général les calculs perturbatifs similaires à l'électrodynamique quantique.
L'interaction forte est aussi caractérisée par la liberté asymptotique, à faible distance la constante de couplage s'affaiblit : les expériences de plus haute énergie qui sondent des distances courtes de l'ordre du fermi sont dans le régime QCD dit perturbatif pQCD : les calculs perturbatifs étant alors possibles ces expériences ont montré un accord avec les résultats prédits par pQCD confortant la théorie QCD comme description de l'interaction forte. Ainsi la diffusion d'électrons a permis de sonder les nucléons permettant d'observer différentes propriétés de ceux-ci telles que les facteurs de forme pour la diffusion élastique. Ce type d'expérience donne accès à la distribution de charge du nucléon dont les facteurs de forme sont la transformée de Fourier. A plus haute énergie, elle a permis de mettre en évidence la sous-structure des nucléons dans les expériences dite de diffusion profondément inélastique (deep inelastic scattering DIS) : par des mesures inclusives en ne détectant que l'électron diffusé, il a pu être montré que l'interaction était analogue à une diffusion élastique sur un des composants du nucléon appelés partons. Mais ces deux types d'expériences montrent aussi tout le paradoxe et la difficulté de l'étude de la structure du nucléon : la diffusion élastique donne une distribution spatiale du nucléon sans informations sur sa structure interne alors que le DIS donne des informations sur les densités de partons au contraire sans aucune information spatiale. Les expériences étudiant la structure en spin du nucléons cherchent à déterminer les différentes contributions la composant. Les expériences EMC, SMC au CERN et E142, E143, E154 et E155 du SLAC ont montré que la contribution du spin des quarks $\frac{1}{2}\Delta\Sigma$ ne représentait qu'une fraction du spin total du nucléon, le reste provenant du spin et du moment orbital des

gluons et du moment orbital des quarks qui restent donc à déterminer. Avec les progrès réalisés dans le domaine des accélérateurs, l'étude de réactions exclusives est devenue possible. La réaction de diffusion Compton Virtuelle permet d'obtenir de nouvelles informations sur le nucléon. Cette réaction est la production d'un photon réel à partir d'un photon virtuel sur le proton. Elle est une des réaction exclusive contibuant au Deep Inelastic Scattering dans le cas où le proton reste intact dans l'état final. Un nouveau formalisme a permis d'interpréter ce type de réaction exclusive : les distributions de partons généralisées. Ces distributions permettent de faire le lien entre les facteurs de forme et les distributions de partons qui en sont des cas limites. Les distributions de partons ordinaires donnent accès aux éléments diagonaux du tenseur hadronique qui représentent une densité de quarks alors que les GPDs donnent accès aux éléments non diagonaux du tenseur hadronique : ce sont des fonctions de corrélations entre les différents quarks ce qui permet d'obtenir des informations supplémentaires en particulier une information spatiale qui permettrait de déterminer le moment angulaire des quarks au sein du nucléon. L'expérience du Hall A est la première expérience dédiée à la diffusion Compton Virtuelle dans le régime profondément inélastique (Deeply Virtual Compton Scattering (DVCS)). Deux nouveaux détecteurs ont été construits pour être associés au spectromètre à haute résolution du Hall A : un calorimètre électromagnétique constitué de 112 blocs de fluorure de plomb arrangés dans une matrice de 12x11 et un détecteur de proton constitué d'un anneau de scintillateurs de 20 modules couvrant un angle azimutal de 270 degrés. Chaque module comporte cinq blocs de scintillateurs plastique couvrant chacun un angle polaire de 4 degrés. Le fait d'utiliser un spectromètre à très faible acceptance nécessite d'utiliser une haute luminosité. Ce qui constitue la majeure difficulté de l'expérience : faire fonctionner le calorimètre et le détecteur de proton qui ont une large acceptance dans des conditions de bruit de fond particulièrement hostile du fait de cette luminosité. Une des solutions déjà avancée dans la proposition d'expérience a été l'utilisation d'une électronique dédiée qui a constitué, avec la mise en place du calorimètre la majeure partie de ma contribution à l'expérience. Le travail s'est donc divisé en quatre parties : l'étude du bruit de fond et les mesures prises pour en limiter l'effet, la mise en place de l'expérience : installation du système d'échantillonnage dans l'acquisition du Hall A, montage et tests du calorimètre, prise de données et enfin analyse des données après l'expérience pour l'étude de l'éléctroproduction de pions.

Analyse du bruit de fond Les simulations et les tests en faisceau ont effectivement montré que les détecteurs seraient soumis à des conditions de bruit de fond extrêmes. Plus précisément ce bruit de fond se manifeste sous deux formes :

- bruit de fond de haute énergie entraînant l'empilement de signaux parasites

sur les signaux physiques

- bruit de fond de très basse énergie produisant un courant d'anode en continu sur les photomultiplicateurs.

Pour limiter l'effet du courant continu sur la charge débitée par le PM directement liée à sa durée de vie. Le gain des photomultiplicateurs a été réduit en reduisant la haute tension appliquée à ceux-ci. Cela a été compensé par une amplification des signaux permettant de reduire le courant d'anode. Ce courant a été surveillé en continu. La chambre de diffusion a été modifiée pour limiter les réactions secondaires pouvant se produire après la cible. Elle conçue pour servir de blindage des détecteurs par l'intermédiaire de son épaisseur de 1 cm d'aluminium. Enfin pour régler le problème de l'empilement nous avons eu recourt a une électronique dédiée effectuant un échantillonnage du signal à la freǵuence de 1 GHz permettant de discriminer et traiter les événements avec empilement plus tard durant l'analyse des données ce qui n'est pas possible avec une électronique conventionnelle.

Mise en place de l'expérience et prise de données

Electronique et acquisition de données Pour pouvoir gérer le bruit de fond dans les détecteurs, deux modules électroniques dédiés ont été développés pour l'expérience par Michel Brossard du laboratoire LPC Clermont Ferrand :

- un module de déclenchement pour déterminer la présence d'un photon et réaliser une coïncidence entre le spectromètre et le calorimètre. Ce module comporte un "Flash ADC" encodant chaque voie de calorimètre sur 7 bits. Le signal du spectromètre est utilisé pour générer la porte de ceux-ci. Une fois toutes les voies du calorimètre numérisées le module effectue les sommes de toutes les combinaisons de quatre blocs adjacents. Si l'une de ces sommes est au dessus d'un seuil fixé au préalable un signal photon est géneré. Puisque le codage et le calcul des sommes commencent quand le module reçoit le signal électron du spectromètre, ce signal correspond à une coïncidence électron photon et sera utilisé comme signal de déclenchement de l'expérience.

- un système d'échantillonnage basé sur le principe de la mémoire analogique du circuit ARS développé par le CEA. Le signal d'entrée est stocké en continu sur une série de 128 condensateurs montés circulairement à une fréquence de 1 GHz. Ce processus d'échantillonnage peut être interrompu ce qui permet de conserver effectivement 128 nanosecondes de signal sous forme analogique. Une fois l'échantillonnage stoppé l'encodage peut être

déclenché par un deuxième signal dans ce cas chaque échantillon est numérisé sur un ADC 12 bit à une fréquence de 1 MHz dans le cas contraire l'échantillonnage reprend après 1 microseconde permettant de limiter la phase lente d'encodage aux événements intéressants et ainsi de réduire le temps mort.

Intégration à l'acquisition du Hall A : trigger de l'expérience et lecture des modules L'acquisition standard du Hall est située pour la partie électronique dans la hutte blindée des détecteurs qui est reliée aux ordinateurs de la salle de comptage par l'intermédiaire d'un réseau Ethernet. Le trigger standard d'un spectromètre est généré par deux plans de scintillateurs, une particule issue du spectromètre passe en général par ces deux plans, d'où l'utilisation de la coïncidence de ces deux plans pour générer le trigger spectromètre. Le trigger calorimètre décrit précédemment a donc été ajouté à l'acquisition standard du spectromètre. Ceci a nécéssité l'adjonction de deux châssis VME à l'acquisition standard du Hall A un pour chaque détecteur en suivant la convention des noms utilisée par le systême d'acquisition CODA :

- ROC 17 pour le calorimètre. Il contenait module de déclenchement du calorimètre et les ARS pour l'enregistrement des données. Le signal qui sert au déclenchement de la prise de données est générée aussi dans ce châssis sur un module dédié.
- ROC 18 est lui dédié à la lecture des scintillateurs du détecteur de proton et du veto de proton, ce châssis n'a été utilisé que pour enregistrer les signaux des détecteurs de protons et du veto de protons et n'a pas joué de rôle au niveau du déclenchement, la triple coïcidence étant réalisées au moment de l'analyse.

Test des détecteurs L'électronique de l'expérience et les détecteurs ont été montés dans la salle blanche du Jefferson Laboratory dés juillet 2004. Cela a permis de tester le dispositif dans une configuration proche des conditions expérimentales finales. Le calorimètre a été le centre des tests avec la mise en place :

- du détecteur et de son électronique associée
- du trigger calorimètre
- du système de diodes pour le monitorage du gain

Cette période a permis le développement et la validation du systeme d'échantillonnage et de trigger du calorimètre. La mise au point du système de monitorage du gain. Et finalement les calibrations des différents détecteurs avec les rayons cosmiques ont pu être effectuées..

Prise de données La prise de données a été effectuée de septembre a décembre 2004 pour les deux expériences E00-110 sur cible d'hydrogène liquide et E03-106 sur cible de deutérium pour étudier le DVCS sur le neutron. Les principales cinématiques sont résumées dans le tableau suivant.

Cinématique	Durée	e angle	e impulsion	Calo angle
1	9 jours	15.58	3.55	22.29
2	15 jours	19.32	2.95	18.25
3	14 jours	23.91	2.35	14.8
nDVCS	26 jours	19.32	2.35	18.25

Quelques jours avec le spectromètre en polarité positive ont aussi été dédiés pour la calibration du calorimètre avec la diffusion élastique électron proton en detectant le proton dans le spectromètre et l'électron dans le calorimétre et les mesures pour l'efficacité des détecteurs aux neutrons avec la réaction $ep \rightarrow en\pi^+$.

Analyse des données

Analyse en forme Pour tirer parti du système d'échantillonnage nous avons développé une méthode pour extraire une impulsion ayant subit un empilement. Le signal expérimental est ajusté comme une combinaison linéaire de

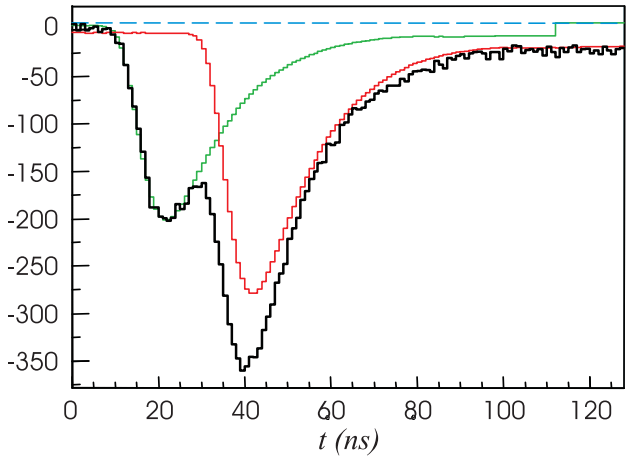

Figure 1: Signal avec empilement

formes de référence préalablement déterminée à partir des données de calibration déplacées dans le temps. En effectuant une minimisation pour les cas contenant 0,1 ou 2 signaux, il est possible d'extraire la bonne amplitude et le bon temps d'arrivée du signal recherche comme sur l'exemple Fig. 1.

Electroproduction de π^0 Après la prise de données DVCS, nous nous sommes rapidement intéressés à la réaction d'électroproduction de π^0. Cette réaction est en effet facilement identifiable par la présence de deux photons en coïncidence dans le calorimètre, ce qui a permis de vérifier la calibration du calorimètre en utilisant la masse du pion comme référence. Un échantillon d'événements à deux photons enregistrés pour le point cinématique à $Q^2 = 2.32GeV^2$ a donc été utilisé pour déterminer la section efficace d'électroproduction de π^0. L'échantillon duquel les différentes fortuites sont soustraites contient déjà une majorité de π^0 exclusifs contaminés par des évènements à deux pions dans l'état final. Les pions exclusifs ont donc été extraits en utilisant la simulation pour modéliser les différentes réactions en corrigeant des effets d'acceptance et de corrections radiatives. Par une méthode d'ajustement de ces différentes contributions, nous avons pu obtenir la section efficace d'electroproduction de π^0 en fonction du moment de transfert t..

Conclusion Nous avons montré qu'un type différent d'expérience de diffusion Compton Virtuelle était possible avec l'usage d'un spectromètre à haute résolution associé à une luminosité de $10^{37}cm^{-2}s^{-1}$. Le fait d'avoir à utiliser une haute luminosité a impliqué de nombreux développements pour limiter l'effet du bruit de fond que ce soit au niveau du blindage, de la conception des détecteurs et de l'électronique. Les résolutions obtenues à partir du spectromètre et du calorimétre permettent déjà l'étude de réactions exclusives uniquement en utilisant les données de ces deux détecteurs tout en permettant de vérifier l'exclusivité avec le détecteur de proton s'il s'en avère nécessaire. Ces méthodes d'analyse nous ont permis d'extraire les sections efficaces d'électroproduction de π^0 dans le cadre de cette thèse et de la différence de sections efficaces DVCS dans le cadre de la thèse de C. Munoz Camacho. Cette première mesure est donc très prometteuse puisqu'elle est la première mesure de section efficace donnant un accès plus direct aux distributions de partons généralisées pour le DVCS et permettra d'accéder à une autre combinaison linéaire de GPDs dans le cas de l'électroproduction de π^0. Les expériences exclusives de ce type ou utilisant des détecteurs à grande acceptance sont donc vouées à un bel avenir puisque de nombreux points cinématiques et expériences différentes doivent être menés pour séparer et déterminer les différentes GPDs : les expériences de DVCS sont programmées a Hermes, Compass et au Jefferson Laboratory dans les années qui viennent.

Contents

Acknowledgements **iii**

Résumé en français **vii**

1 Introduction **1**

2 Generalized Partons Distributions (GPDs) **5**
2.1 Electromagnetic probe 5
2.2 Elastic scattering : form factors 6
2.3 Deep Inelastic Scattering : parton distribution 7
2.4 Generalized parton distributions (GPDs) 10
2.4.1 Hard scattering and factorization 11
2.4.2 Definition of the GPDs 11
2.4.3 Limit properties of GPDs 12
2.5 Exclusive reactions and GPDs 14
2.5.1 Deeply Virtual Compton Scattering 14
2.5.2 Meson electroproduction crossection 17
2.6 Experimental difficulties 18
2.6.1 Physical background 18
2.6.2 Experimental background 19
2.7 First evidences of DVCS events 19
2.7.1 HERA 19
2.7.2 HERMES 20
2.7.3 Hall B 20
2.8 New set of experiments ensuring the exclusivity of the reaction . . 21
2.8.1 Exclusivity 21
2.8.2 Hermes 21
2.8.3 Jefferson Laboratory Hall B 21
2.8.4 Compass 21
2.9 Summary of the experiments features 22

3 DVCS in Hall A **25**
3.1 Overview of Jefferson Laboratory accelerator 25
3.1.1 Accelerator 25
3.1.2 Injector 26
3.2 Hall A standard equipement 27
3.2.1 Beamline equipement 27
3.2.2 Target 29
3.2.3 Hall A spectrometer 30
3.3 Specific equipment 35
3.3.1 Detectors design 35
3.3.2 Electromagnetic calorimeter 36
3.3.3 Proton Array 39
3.3.4 Mechanical assembly 39
3.3.5 Hall A DVCS specific background issues in Hall A 43
3.4 Experimental background distribution 47
3.4.1 March 2002 test run 47
3.4.2 Rate determination 48
3.4.3 Accidental studies in DVCS data 49
3.4.4 Designs for handling the background 50
3.5 Conclusions 51

4 Electronics and data acquisition **61**
4.1 Data acquisition basics 61
4.2 Standard Hall A DAQ 62
4.2.1 Jefferson laboratory data acquisition package CODA . . . 62
4.2.2 CODA implementation of the Left spectrometer DAQ . . . 64
4.2.3 Trigger setup 64
4.2.4 CODA configuration of the spectrometer read-out 66
4.3 Experiment specific electronics and CODA setup 67
4.3.1 Experiment requirements 67
4.3.2 DVCS trigger logic 67
4.3.3 DVCS data readout 74
4.3.4 Dead time and electronics performances 80
4.4 Experiment slow control 84
4.4.1 Standard Hall A slow control 85
4.4.2 DVCS IOC 85
4.4.3 High Voltage 85
4.4.4 DC monitoring 85
4.4.5 Gain monitoring system 86
4.4.6 EPICS event in data stream 86
4.5 DAQ commissioning 86

4.6 DAQ possible improvement 87
4.7 Conclusion 89

5 Detectors tests and comissioning 91
5.1 Calorimeter 91
5.1.1 Cosmics data taking : calorimeter balancing 91
5.1.2 LED system 92
5.1.3 Continuous scans 95
5.1.4 Calorimeter LED configuration 96
5.1.5 Calorimeter LED monitoring 100
5.1.6 Radiation damage 100
5.1.7 Conclusion 100

6 Analysis 103
6.1 Analysis strategy and software organization 103
6.2 Waveform analysis 105
6.2.1 Waveform analysis algorithm 105
6.2.2 Reference shape 105
6.2.3 Loop on the number of pulses 105
6.2.4 Pulse fitting function 106
6.2.5 Minimzation in the case only one pulse is fitted 106
6.2.6 Minimization on the amplitude : case of 2 pulses and constant background 106
6.2.7 Parameter settings 109
6.2.8 Software implementation 109
6.3 Electron arm analysis 111
6.3.1 Available spectrometer information 111
6.3.2 Particle identification 114
6.4 Calibrations and corrections 115
6.4.1 Deadtime 115
6.4.2 Absolute charge determination, luminosity monitoring . . . 116
6.5 Calorimeter analysis 120
6.5.1 Clustering algorithm 120
6.5.2 Position reconstruction 120
6.5.3 Elastic scattering calibration 120
6.5.4 Calorimeter trigger 127
6.5.5 Trigger read-out topology 127
6.5.6 Calorimeter corrected coincidence time : timing resolution 129
6.5.7 DVCS data : photon vertex reconstruction 130
6.6 Radiation damages : accumulated dose 132
6.6.1 Background from DVCS data on calorimeter 132

6.6.2 Calorimeter recalibration method 134
6.7 Pion electroproduction 135
6.7.1 Kinematic 135
6.8 Data analysis 137
6.8.1 Run selection 137
6.8.2 π_0 events selection 139
6.8.3 Accidentals 142
6.8.4 More than two clusters events 144
6.9 Background identification and estimation 145
6.10 Extraction 145
6.11 Simulation 147
6.11.1 Event generation 147
6.11.2 Resolution adjustment of the simulation 148
6.11.3 Extraction method 150
6.11.4 Extraction of TL part of the cross section 153

7 Conclusions and outlook 155
7.1 Experiment summary 155
7.1.1 Proton array 155
7.1.2 Calorimeter 155
7.2 Mapping GPDs 156
7.2.1 DVCS cross section measurement 156
7.2.2 Interference term measurement 157
7.2.3 Double polarized experiments 158
7.2.4 Deeply Virtual Meson production 159
7.2.5 Double DVCS 159
7.2.6 Neutrino DVCS 160
7.2.7 DVCS on nuclei 160
7.2.8 Inverse DVCS : photo-production of lepton pairs 160
7.3 Conclusions 160

List of Figures

1 Signal avec empilement xi

2.1 Definition of the leptonic plane kinematic 6
2.2 Deep inelastic scattering 8
2.3 Deep inelastic scattering amplitude 10
2.4 Handbag diagram for Hard Scattering Reactions 13
2.5 Bethe-Heitler process diagram 15
2.6 Electroproduction simulated cross section by Guichon et al. [46] . 16
2.7 Definition of ϕ the angle between the leptonic and hadronic plane 16
2.8 Example of some exclusive processes within the Deep Inelastic Scattering from data from Hall B CLAS detector 18
2.9 DVCS kinematical coverage with available facilities 23

3.1 Accelerator setup 26
3.2 Hall A layout 27
3.3 Moeller polarimeter setup 28
3.4 Compton polarimeter setup 29
3.5 Spectrometer magnet layout 32
3.6 Spectrometer detector stack 33
3.7 Histograms of main physics variables after all analysis cuts for the kinematical point. 36
3.8 Typical signal from the calorimeter recorded with the sampling system 38
3.9 Foreseen angular proton distribution 39
3.10 Corresponding proton angle versus photon angle 40
3.11 DVCS stand in Hall A 41
3.12 Side view of the DVCS stand 42
3.13 Typical pile-up events 43
3.14 Rate dependence versus angle 45
3.15 Rate dependence versus angle 46
3.16 Simulated DC current generated by the background 52

3.17 AC coupled signal as seen by the electronics 53
3.18 Counting rates with 1/2 inch of Aluminum shielding and 1/2 inch of Lucite 54
3.19 Counting rates with 1/2 inch of Aluminum shielding and 1 inch of Lucite 55
3.20 Energy distribution of accidentals in the calorimeter 56
3.21 Singles accidental rates by block in calorimeter 57
3.22 Accidentals rates by block of energy higher than 1 GeV 58
3.23 Accidental rates by block of energy lower than 1 GeV 59
3.24 Improvement from the beam pipe enlargement 60

4.1 Example of CODA configuration 63
4.2 Single arm trigger 65
4.3 DVCS trigger summary 68
4.4 DVCS validation 70
4.5 elements added for the DVCS coincidence trigger 72
4.6 Coincidence peak taken from run 2807(B) and 2809 (A) generated with the ARS, trigger signal coming from S2m was delayed by 10 ns, the run was taken in the configuration for pions : $\pi+$ were taken in the left spectrometer and electrons in the calorimeter . . 74
4.7 Event distribution by logic module type 75
4.8 ADC spectrum of the Cerenkov sum depending on the type from the logic module 76
4.9 Timing of the ARS for LED all 7 LED combinations of 3 LEDs . 81
4.10 Calorimeter left spectrometer corrected time coincidence spectrum for kinematic Q^2=2.32 GeV^2 82

5.1 Cosmics which generated a trigger for the calorimeter 92
5.2 Plot of the pulse integral distibution for all calorimeter blocks with selection on vertical events 93
5.3 Vertical scan of one calorimeter column 96
5.4 Relative gain variation with DC current at HV=700V for Hamamatsu PMT R7700 99
5.5 Gain variation with DC current 101
5.6 Gain variation day by day with LED on the whole calorimeter . . 102
5.7 Gain variation day by day for block 126 102

6.1 Results of the 0,1 or 2 pulses fit 105

6.2 The reference pulse is translated in the time window by one nanosecond and a linear fit is performed for each of this steps. The result is the fit which has the minimal χ^2. The χ^2 variation depending on the time position of the reference pulse is schematically represented. 108
6.3 Clock used to determine the running time versus the recorded clock and the current 116
6.4 Ratio of Faraday cup current over I0L02 BCM current versus delivered 117
6.5 Online results of Compton Polarimeter using the electron detector 119
6.6 Elastic lines for the 3 elastics settings 122
6.7 Calorimeter resolution determined from the elastic scattering data 126
6.8 Thresholds on calorimeter tower 128
6.9 Number of blocks read out by event 128
6.10 Calorimeter left spectrometer corrected time coincidence spectrum for kinematic Q^2=2.32 GeV^2 129
6.11 Trigger pedestal for block 6 (23 degrees) block 66(15 degrees) and block 126 (7 degrees) 130
6.12 DC current distribution on the calorimeter 132
6.13 Kinematical variables 135
6.14 Raw invariant mass reconstructed from two photons in the calorimeter with a cut on the energy at 1.2 GeV 137
6.15 Number of events normalized by the beam current 138
6.16 Spectrometer angle conventions 140
6.17 Electron angular distribution 140
6.18 Electron angular distribution after R-function cut 141
6.19 Number of clusters by event distribution 142
6.20 Arrival time of first cluster versus arrival time of the second cluster axis are in ns. We can see 144
6.21 Missing mass of the reaction $ep \rightarrow e\pi^0 X$ with no background subtraction, one can see the different background contributions 145
6.22 Invariant mass spectrum of the two photons in the calorimeter with subtracted accidentals 146
6.23 Missing mass of the reaction $ep \rightarrow e\pi^0 X$ with background subtraction 147
6.24 Pion invariant mass 149
6.25 Missing mass vs pion invariant mass from simulation 150
6.26 Missing mass vs pion invariant mass from data 150
6.27 Missing mass squared $ep \rightarrow ep\pi^0 X$ in GeV^2 153
6.28 t distribution at vertex 154
6.29 Pion electroproduction cross section integrated over ϕ as a function of t 154

List of Tables

3.1 Main design characteristics of the Hall A High Resolution Spectrometers. The resolution values are for the FWHM. 31

5.1 Number of photoelectrons by ARS channel for the calibration setting 97

6.1 Run period used for efficiencies determination 111
6.2 Pedestal width depending on the block 131
6.3 Number of events going through the set of given cuts 143

Chapter 1

Introduction

The underlying components of matter have for a long time been a subject of interest. The atom concept has existed already since antiquity but little was known about those atoms and the forces that were binding them together had still to be understood. Progresses in this domain had to wait for the twentieth century which was one of the most prolific century as far as experimental and theoretical physics were concerned. It indeed saw fundamental discoveries such as the nucleus, neutron, quantum mechanics ... and eventually quarks. Deep Inelastic Scattering of electrons on protons (DIS)[19] at the Stanford Linear Accelerator (SLAC) experiments showed the substructure of the nucleons built up from quarks. Yet the strong interaction binding the quarks in the nucleon remains a puzzle. It has indeed two main characteristics. It has a running coupling constant which increases when the distance between quarks grows, this explains why no free quark could ever be seen. This phenomenon is known as confinement. The other one is asymptotic freedom : the strong interaction decreases when quarks are close together. Since higher energies allow to probe shorter distance, this fact is characterized by what is called scaling : the scattered electron behaves as if it was interacting with a single free quark. The DIS and the meson spectroscopy led to the Gell Mann SU(3) [41] model of the proton and to Feynman's parton distributions. The theory which could reconcile those two features came out later with Quantum Chromodynamics (QCD). QCD is a gauge theory adding to the flavor SU(3) group another SU(3) symmetry : the quantum number "color". By stating that all systems build-up of quarks have to be colorless in order to be stable this explained why no single quark could ever be seen. The non abelian nature of this theory was able to account for the running of the strong coupling constant. QCD could be confirmed thanks to high energy experiments. The number of colors was for example determined at LEP [17] and since α_s is smaller than 1 at these energies perturbative calculations (pQCD) are possible : pQCD successfully predicts the scaling violation in DIS. But α_s being larger

than one in the nucleon at rest this prevents from any perturbative techniques as used in QED. Though non perturbative numerical methods such as lattice QCD are possible, a complete calculation on the nucleon is till being worked out. The major problem with DIS experiments is since we see quarks as free single particles we lose information about their behavior relative to each other in the nucleon. The most famous example is the so-called "spin crisis" coming from the first polarized experiments carried at SLAC and EMC [9] experiment which showed than unlike the simple proton description where its spin would be the sum of the spins of its three constituent quarks, the contribution of the quarks was only a fraction of the total spin of the proton hinting at a more dynamical view of the inside of the nucleon. Recently a new formalism the Generalized Parton Distributions (GPDs) [56] was designed to parametrize the nucleon non perturbative physics (often referred as soft to be opposed to pQCD at high energy). Similarly to physical statistics and thermodynamics, they describe the nucleons at the parton level allowing to compute "macroscopic" observables such as form factors but also the correlations between partons. Their definition and properties will be presented in the chapter 2 of this document. These GPDs are accessed by measuring exclusive reactions on nucleons. Experimentally this kind of measurement is more difficult since the final state has to be detected unlike DIS measurement where only the scattered electron was detected. The Deeply Virtual Compton Scattering (DVCS) is the simplest exclusive reaction that can be studied[46]. It is characterized by consisting in only a proton and a real photon in the final state and was the process chosen to be studied for this experiment which ran from September to December 2004 in Hall A at Jefferson Laboratory. The main challenge was running at high luminosity up to $10^{37} cm^2 s^{-1}$ to study the Deeply Virtual Compton Scattering process while still being able to detect the three particles of the final state. This condition implied to add two new detectors in Hall A : an electromagnetic calorimeter and a recoil proton. The use of a calorimeter in Hall A had two previous experiment precedents the G_{E_p} measurement (E99-007) [39] and Real Compton Scattering [26] (E99-114) but these calorimeters were located at angles from the beam larger than 20 degrees and at distances larger than 5 meters. DVCS experiment took one step further by adding detectors down to an angles with respect to the beam of 14.8 degrees for the calorimeter (the closest blocks going up to 8 degrees) and 18 degrees for the scintillator array at distance respectively of 110 cm and 80 cm from the target. So the work was to prove the experiment was feasible and to have a strategy to handle the background. This will be developed in the chapter 3 which presents the experimental setup and deals with the experimental aspects of the experiment : the study of the background which drove the design of the detectors. The chapter 4 deals with the electronics. Custom electronics specifically developed for this experiment were added. I was responsible for all the components added to Hall A

standard equipment : the ARS sampling system and the calorimeter trigger as well as the implementation of LED gain monitoring system. The chapter 5 summarizes the tests on the detector focusing on the calorimeter. The chapter 6 deals about the data analysis from the detector calibration, charge and luminosity and a preliminary analysis on the electroproduction of π^0. The π^0 electroproduction is interesting to be studied in order to subtract it for the DVCS analysis and by itself since few data on exclusive π^0 production is available in this kinematical range. I will conclude in chapter 7 with a summary of the experiment and the outlooks on the future DVCS measurements.

Chapter 2

Generalized Partons Distributions (GPDs)

2.1 Electromagnetic probe

The scattering of leptons in general and in our particular case with electrons is a powerful probe. Leptons are indeed to the best of our knowledege elementary particles and their electro-weak interactions with matter at energies below the TeV are well understood. The dimensionless coupling constant of the electromagnetic interaction is $\alpha \approx 1/137$. Since α is small , accurate perturbative calculations are possible by taking into account only the first term of the perturbative development. Depending on the energies available, electron scattering allowed to unravel different kind of information about the nucleon. Historically, the first information that could be extracted was the proton radius through elastic scattering by Hofstadter [51]. Later and at higher energy the substructure of the nucleon was discovered with the first deep inelastic experiment carried on by Kendall, Friedman and Taylor [19]. I will focus on electroproduction reaction involving virtual photons since in the range of energy of Jefferson Laboratory reactions involving weak interaction are negligible. In this section I will use the four-vectors defined with the metric tensor (+,-,-,-). I will denote the space component of the associated four-vector with a vector arrow above the quadrivector name. We define the incident electron four momentum k and the scattered electron k'. Since energies are of the order of 1 GeV for this experiment the electron mass will always be neglected . In the laboratory frame, we define by θ the angle between $\vec{k}$ and $\vec{k'}$ as shown in Fig. 2.1. We then define the four-momentum of the virtual photon q :

$$q = k - k' \tag{2.1}$$

$$Q^2 = -q^2 = -(k-k')^2 = 4EE' \sin^2(\frac{\theta}{2}) \tag{2.2}$$

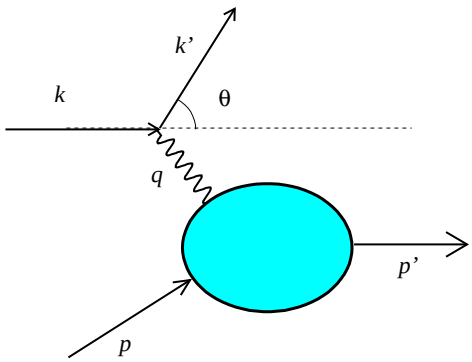

Figure 2.1: Definition of the leptonic plane kinematic

Q^2 is the virtuality of the photon. This variable is interesting because it is related to the space-time scale which is probed. Using the associated wavelength $\lambda = \frac{\hbar c}{q}$ this scale is of the order 10^{-16} m for $Q^2 = 1GeV^2$ which is a typical value reachable at Jefferson Laboratory.

2.2 Elastic scattering : form factors

The elastic cross section of the electron scattering can be represented in the Born approximation (to the first order in α) by the diagram Fig. 2.1. The cross section for the scattering from a point-like charge is given by the Mott cross section [50]: E the incident electron energy, θ the angle between the incoming and outgoing electron $v = k/E$

$$\left(\frac{d\sigma}{d\Omega}\right)_{point} = \left(\frac{d\sigma}{d\Omega}\right)_{Mott} = \frac{\alpha^2 E^2}{4k^4 \sin^4 \frac{\theta}{2}} \left(1 - v^2 \sin^2 \frac{\theta}{2}\right) \tag{2.3}$$

An extended charge distribution (of a spin zero target) is taken into account by adding a form factor (FF) :

$$\left(\frac{d\sigma}{d\Omega}\right) = \left(\frac{d\sigma}{d\Omega}\right)_{Point} |F(q)|^2 \tag{2.4}$$

The proton magnetic and electric form factors were first measured by R. Hofstadter [51] in 1955. They allow to determine the proton size since form factors

are the Fourier transform of the magnetic or electric charge distribution. Since the recoil of the proton has to be taken into account we add the 4-momenta p and p' for the momentum of the proton before and after the interaction. Using the cross section and knowing how to compute the electron part we gain access to information about the proton.
The transition amplitude for the process represented on Fig 2.1 is thus :

$$T_{fi} = -i \int j_\mu \left(-\frac{1}{q^2}\right) J^\mu d^4x \tag{2.5}$$

With j_μ the current associated to the leptonic part :

$$j_\mu = -ie\bar{u}\gamma_\mu u \tag{2.6}$$

And the current for the hadronic part :

$$J_\mu = -ie\bar{u}\left[F_1\left(q^2\right)\gamma_\mu + \frac{\kappa}{2M}F_2\left(q^2\right)\sigma_{\mu\nu}q^\nu\right]u \tag{2.7}$$

with κ the anomalous magnetic moment of the proton. F_1 and F_2 are the Dirac proton form factors. These were extracted from elastic scattering data. Another kind of form factors, the Sachs form factor defined in Eq. 2.8, are usually used. Writing the cross section using these form factors allow to identify directly the electric and the magnetic contributions in the elastic scattering cross section.

$$G_E = F_1 + \frac{\kappa q^2}{4M^2}F_2 \tag{2.8}$$

$$G_M = F_1 + \kappa F_2 \tag{2.9}$$

2.3 Deep Inelastic Scattering : parton distribution

Going to higher energies in electron scattering probes shorter distances allowing to reach the inner structure of the proton [18]. In the case where both Q^2 and the virtual photon energy $\nu = E - E'$ go to infinity while keeping the ratio $x_B = \frac{Q^2}{2M\nu}$ finite : we find ourselves in the Deep Inelastic Scattering (DIS) regime. In this regime the final state X is most of the time not a proton any more which leads to a parametrization of the hadronic tensor in the most general way. This reaction is inclusive : only the scattered electron is detected. Studying the cross section of the process can thus extract information about the proton structure. In order to do so we define the diagram associated to this process in Fig. 2.2

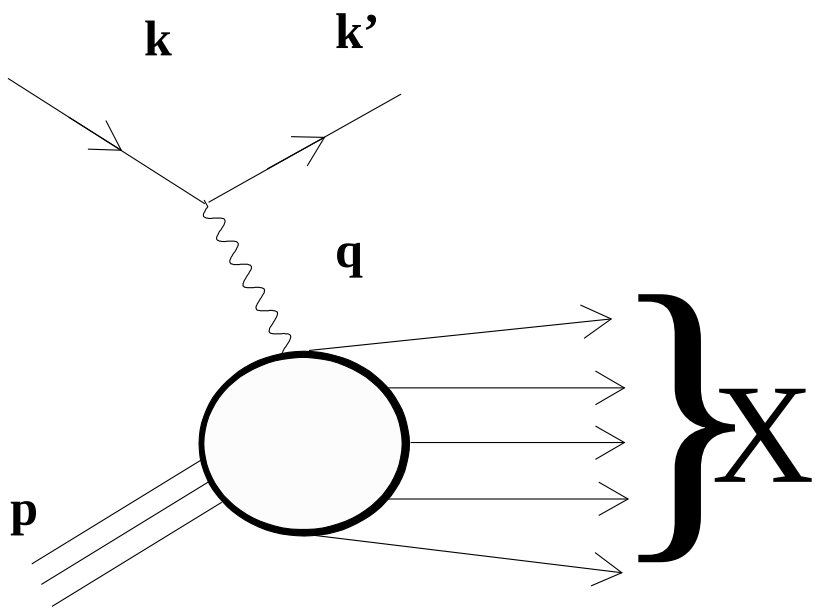

Figure 2.2: Deep inelastic scattering

If we define the transition matrix element for a final state X with an initial state P(p) corresponding to a proton of momentum p, associated to the Feynman diagram 2.2 :

$$M(X,P) = \bar{u}\left(k'\right)\gamma_\mu u\left(k\right)\frac{1}{q^2}\left\langle X\left(p_X\right)\left|j_\mu\left(0\right)\right|P\left(p\right)\right\rangle \tag{2.10}$$

where $j_\mu(0)$ is the hadronic current and we have the current for the incoming electron : the DIS cross section which is then the product of $L_{\mu\nu}$ the leptonic tensor and the hadronic tensor $W_{\mu\nu}$ the most general tensor that can be constructed with the 4-momenta q, q' :

$$d\sigma \sim L^e_{\mu\nu}W^{\mu\nu} \tag{2.11}$$

Using symmetry arguments, gauge invariance and the QED conservation laws it can be expressed as :

$$\begin{aligned} W_{\mu\nu} = W_1(Q^2,\nu)(-g_{\mu\nu} + \frac{q_\mu q\nu}{q^2}) + \frac{W_2}{M^2}(Q^2,\nu)(p_\mu - \frac{p.q}{q^2}q_\mu)(p_\nu - \frac{p.q}{q^2}q_\nu) \\ +G_1(Q^2,\nu)Mi\epsilon_{\mu\nu\lambda\sigma}q^\lambda s_h^\sigma + \frac{G_2(Q^2,\nu)}{M}i\epsilon_{\mu\nu\lambda\sigma}q^\lambda(p.qs_h^\sigma - s_h^\sigma.qp^\sigma) \end{aligned} \tag{2.12}$$

with $s_h^\sigma \approx hk^\sigma/m$.

W_1 and W_2 are the spin independent structure functions and G_1 and G_2 the spin dependent ones. The structure functions are also commonly expressed in the form :

$$MW_1 = F_1(Q^2, \nu) \tag{2.13}$$

$$\nu W_2 = F_2(Q^2, \nu) \tag{2.14}$$

$$\frac{\nu}{(p \cdot q)} G_1(Q^2, \nu) = g1(Q^2, \nu) \tag{2.15}$$

$$\tag{2.16}$$

In the naive parton model, we consider that the nucleons are constituted by three quarks. The parton distributions have an intuitive interpretation in the infinite momentum (frame in which the proton has been boosted to infinite momentum). In this case the DIS can be interpreted as elastic scattering on a free quark carrying a momentum fraction x_{Bj} of the total longitudinal proton momentum. Using this assumption we define the partons distributions :

$$F_1(Q^2, \nu) = \sum_{i=1}^{3} e_i q_i = \sum_{i=1}^{3} e_i (q_i^\uparrow + q_i^\downarrow) \tag{2.17}$$

$$g_1(Q^2, \nu) = \sum_{i=1}^{3} e_i \Delta q_i = \sum_{i=1}^{3} e_i (q_i^\uparrow - q_i^\downarrow) \tag{2.18}$$

$$\tag{2.19}$$

where $q(i)^\uparrow$ is the density of parton the parton of charge e_i with the spin up and $q(i)^\downarrow$ the density of parton the parton of charge e_i with the spin down when the nucleon target is polarized.

The cross section of the DIS can be computed using the optical theorem. It states that the amplitude of the process is equal to the imaginary part of the forward Compton amplitude as shown in Fig. 2.3.

The hadronic tensor can be written as :

$$\begin{aligned} W_{\mu\nu} &= \frac{1}{4\pi} \sum_X < N(p)|j_v(0)|X >< X|j_\mu(0)|N(p) > (2\pi)^4 \delta^{(4)}(p + q - p_x) \\ &= \frac{1}{2\pi M} \Im[T_{\mu\nu}] \end{aligned} \tag{2.20}$$

$$T_{\mu\nu} = i \int d^4 z e^{i(q \cdot z)} \langle N(p,s)| T \{J^\mu(-z/2), J^\nu(z/2)\} |N(p,s)\rangle \tag{2.21}$$

where $T_{\mu\nu}$ is forward Compton amplitude. This Compton Amplitude can be computed as a virtual photon interacting with a single quark. The DIS is described

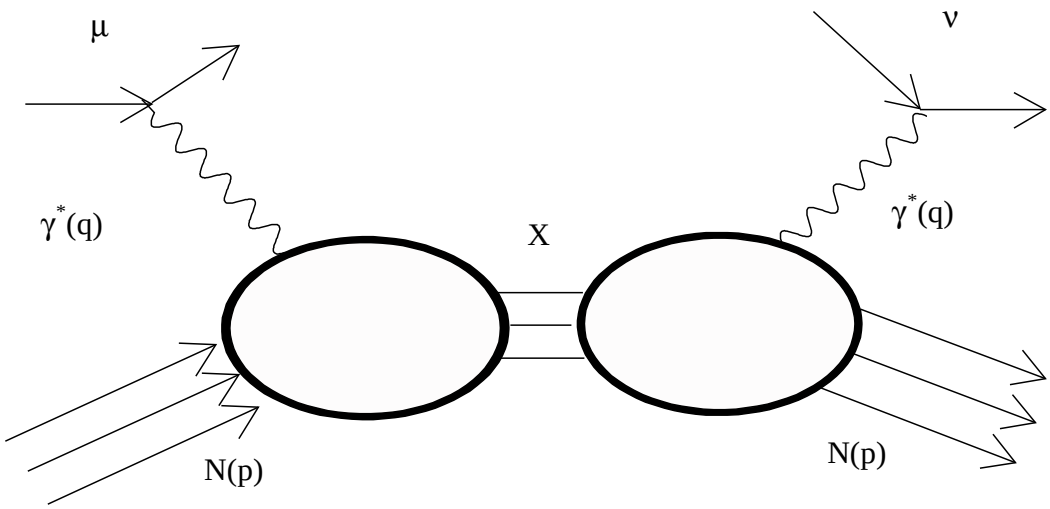

Figure 2.3: Deep inelastic scattering amplitude

by the diagonal elements of the Compton Amplitude matrix elements. We can interpret these diagonal matrix elements as the contribution to the cross section of the absorption of the virtual photon flux when interacting with a quark.

2.4 Generalized parton distributions (GPDs)

We have seen that nucleons could be described by either form factors or partons distributions. But both are limit cases : with the form factor we get to know about the spatial distribution of the charge for the proton but we have no information about its inner structure. While for the DIS we learn about the inner composition of the proton sacrificing the spatial distribution information and the correlations between those constituents. The General Parton Distributions (GPDs) are more general objects linking those two quantities. GPDs are indeed analog to the parton distribution related to the transition matrix but in this case the final state is different than the initial one allowing to access non diagonal elements of the transition matrix. Those give access to correlations between quarks.

2.4.1 Hard scattering and factorization

The factorization theorem was proved by Collins et al. [27] for Hard Scattering Reactions. It states that in the Bjorken limit and at moderate value of t the transverse momentum the amplitude of a Hard Scattering reaction can be expressed as a product of a part calculable with pQCD and a soft part containing the non perturbative information. A hard scattering reaction allows to probe the nucleon. Goeke [42] gives a good picture of the process : like the DIS a high virtuality photon will interact with a single quark of a nucleon. But unlike in DIS the struck quark will radiate a part of its energy in the form of a photon or a meson allowing to keep the nucleon in the final state. This explains the link with elastic form factors. In the Deep Inelastic regime the Virtual Compton Scattering comes out as making Compton Scattering on a single quark : in this kinematical regime the handbag diagram is dominant Fig. 2.4 [74]. This factorization theorem is fundamental since it allows to extract the non perturbative part of the reaction parametrized by the GPDs when measuring hard scattering reactions.

2.4.2 Definition of the GPDs

It is interesting to introduce the light cone coordinates in which the GPDs have an intuitive interpretation . I will use the notation defined in Ji's paper [56]. We define the quantities :

$$P = \frac{p+p'}{2} \qquad q_M = \frac{q+q'}{2} \tag{2.22}$$

$$\Delta = p - p' \tag{2.23}$$

$$t = (p-p')^2 = \Delta^2 \tag{2.24}$$

$$s = (p+q)^2 = W^2 \tag{2.25}$$

$$\bar{M}^2 = P^2 = M^2 + t/4 \tag{2.26}$$

$$\tag{2.27}$$

with M the proton mass. We place ourselves in a frame where the spatial component of P is collinear with the real photon. We then define the light cones vectors :

$$p^\mu = \frac{\Lambda}{\sqrt{2}}(1,0,0,1) \quad n^\mu = \tfrac{1}{\Lambda\sqrt{2}}(1,0,0,-1) \tag{2.28}$$

with Λ a normalization parameter which will be chosen here as $\Lambda = P^+ = P \cdot n$. We can decompose the four-vectors defined in 2.22 on this vectors since the transverse components are null in this frame with ξ.

$$\bar{P}^\mu = p^\mu + (\bar{M}/2)n^\mu$$

$$q^\mu = -\xi p^\mu + (Q^2/2\xi)n^\mu$$
$$\Delta^\mu = -\xi(p^\mu - (\bar{M}^2/2n^\mu)$$
$$k^\mu = (k\cdot n)p^\mu + (k\cdot p)n^\mu$$
$$\xi = \frac{\bar{P}^\mu \cdot q + \sqrt{(\bar{P}^\mu \cdot q)^2 + Q^2\bar{M}^2}}{\bar{M}^2}$$

Expressed in the light cone coordinate ξ is also the ratio of the projection of transfered momentum Δ and of the projection of P along the p^μ vector : $\xi = \frac{\Delta^+}{P^+}$. Since a Lorentz boost only multiply the component along the light cone coordinates by a scalar we can see that ξ is a Lorentz invariant. It can also be expressed in function of the experimental four vectors (appendix B.1 of [13]):

$$\xi = \frac{\Delta \cdot q_M}{P \cdot q_M}$$

We can define the GPDs similarly to the way the structure functions coming from the decomposition of the hadronic tensor for the DIS, were introduced in Ji's article[56]. Let us introduce the generalized quark distribution :

$$\int \frac{d\lambda}{2\pi} e^{i\lambda x} < p'|\bar{\psi}(-\frac{-\lambda n}{2})\gamma^\mu \psi(\frac{\lambda n}{2})|p >$$
$$= \overline{U}(p')\left[H^q(x,\xi,t)\gamma + E^q(x,\xi,t)(p')\frac{i\sigma^{+\alpha}\Delta_\alpha}{2M}\right]U(p)$$
$$\int \frac{d\lambda}{2\pi} e^{i\lambda x} < p'|\bar{\psi}(-\frac{-\lambda n}{2})\gamma^\mu \gamma_5 \psi(\frac{\lambda n}{2})|p >$$
$$= \overline{U}(p')\left[\tilde{H}^q(x,\xi,t)\gamma^\mu\gamma_5 + \tilde{E}^q(x,\xi,t)\frac{i\gamma_5\Delta}{2M}\right]U(p)$$

with U the spinor associated to the proton.

We should note the additional freedom introduced by the variable ξ. ξ has values between [-1,1]. Depending on the sign of $x-\xi$ and $x+\xi$, we are probing correlation between two quarks or antiquarks if the $|\xi| < x$ and between a quark and an antiquark if $|\xi| > x$.

2.4.3 Limit properties of GPDs

By definition GPDs in the forward limit case : $t \to 0$ and $\xi \to 0$ reduce to the ordinary parton distributions :

$$H^q(x,\xi=0,t=0) = q(x)\,, \tag{2.29}$$
$$\widetilde{H}^q(x,\xi=0,t=0) = \Delta q(x)\,, \tag{2.30}$$

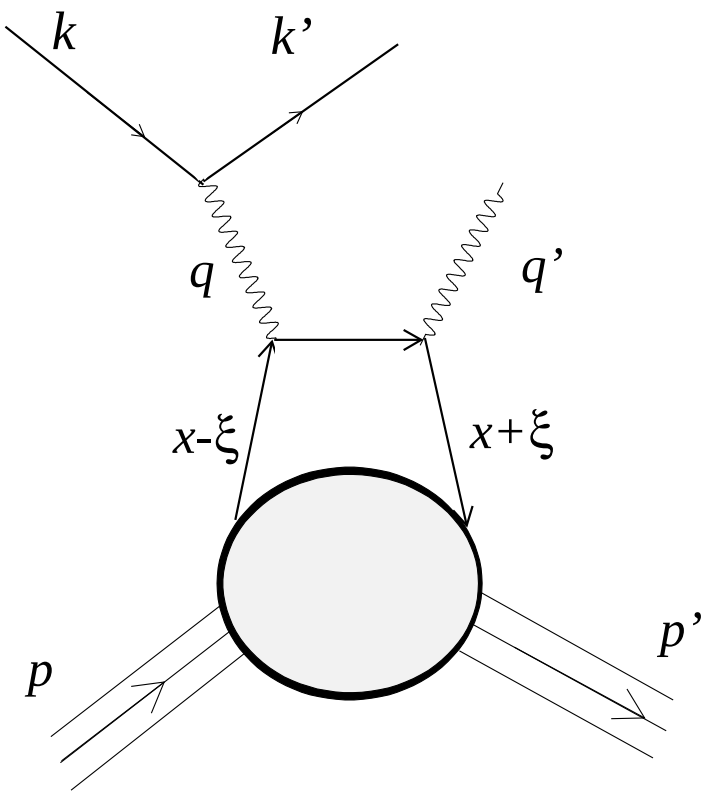

Figure 2.4: Handbag diagram for Hard Scattering Reactions

Integrating the GPDs over x, one recovers the FF :

$$\int_{-1}^{+1} dx H^q(x,\xi,t) = F_1^q(t)\,, \quad \int_{-1}^{+1} dx E^q(x,\xi,t) = F_2^q(t)\,, \tag{2.31}$$

$$\int_{-1}^{+1} dx \widetilde{H}^q(x,\xi,t) = G_A^q(t)\,, \quad \int_{-1}^{+1} dx \widetilde{E}^q(x,\xi,t) = G_P^q(t)\,, \tag{2.32}$$

where F_1 and F_2 are the usual Dirac Pauli Form Factors, $G_A^q(t)$ the axial-form factor and $G_P^q(t)$ the pseudo-scalar form factor.

Orbital momentum From the GPDs one can access to angular momentum of the quarks :

$$J^q = \frac{1}{2}\left[A^q(0) + B^q(0)\right] = \frac{1}{2}\Delta\Sigma^q + L^q$$

where $A_q(t)$ and $B_q(t)$ can be accessed via the GPDs.

$$\int_{-1}^{1} xdx\,[H^q(x,\xi,t) + E^q(x,\xi,t)] = A_q(t) + B_q(t)$$

.

$\Delta\Sigma = \sum_q \Delta\Sigma^q$ is the contribution of the spin of a quark which can be measured in polarized deep inelastic scattering. If we take the limit where t goes to 0, this would allow to access to the quark orbital momentum which would complete the nucleon spin structure decomposition.

2.5 Exclusive reactions and GPDs

2.5.1 Deeply Virtual Compton Scattering

Virtual Compton Scattering (VCS)

The Deeply Virtual Compton Scattering is the simplest exclusive reaction allowing to study the GPDs :

$$\gamma^* p \to \gamma p \tag{2.33}$$

We use the scattering of electrons as a source of virtual photons. So experimentally we study the electroproduction of photon reaction :

$$ep \to ep\gamma \tag{2.34}$$

Electroproduction of real photons

Bethe and Heitler process The Bethe Heitler process consists of the elastic scattering of an electron on a proton where a real photon is radiated by the incoming or the outgoing electron. It has the same final state as DVCS, so these two processes will interfere. The Feynman diagrams associated to this process are shown in figure 2.5. These 2 diagrams Fig. 2.5 have to be summed at the amplitude level with the DVCS diagram of Fig. 2.4 in order to have the electroproduction cross section. Depending on the kinematic and mostly on the incident beam energy this process can dominate over the DVCS. Looking at figure 2.6 for lower energy such as the ones available at Jefferson Laboratory, it is dominant at smaller angle DVCS. However if we are interested in the interference term only we can take advantage of the huge BH contribution: since BH term can have large crossection when going close from the BH pole the interference term of the two processes also has its crossection amplified allowing to access the DVCS amplitude even if it is small by measuring the difference of crossection for the two different helicities of electron : the BH being helicity independent disappear in this difference leaving the interference term $BH \cdot DVCS$ and the squared DVCS

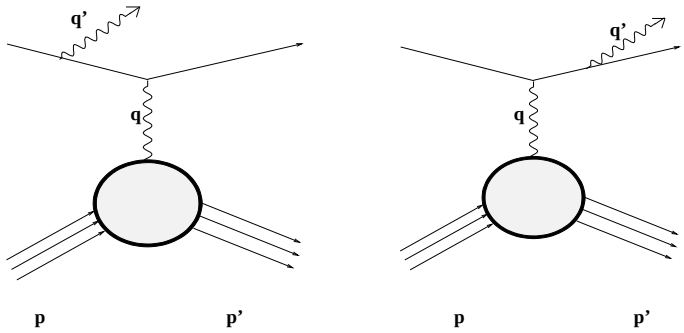

Figure 2.5: Bethe-Heitler process diagram

amplitude which is negligible. On the other hand when going to larger scattering angles (around ±5 degrees around the virtual photon) BH is not overwhelmingly large as close from the beam, so a measurement with enough precision would allow to extract the real part of the DVCS amplitude by subtracting the BH but the price to pay is counting rates decreased by a factor 10.

Electroproduction of real photon cross section To describe the VCS, we define in Fig. 2.7 the leptonic plane containing the incoming k and outgoing k' electron four momentum and the virtual photon q and the hadronic plane containing the scattered proton and the real photon. ϕ is the angle between those two planes.

$$T_{Electroproduction} = T_{DVCS} + T_{BH}$$

The $ep \rightarrow ep\gamma$ cross section is given by:

$$\frac{d^5\sigma^{lp\rightarrow lp\gamma}}{dQ^2 dx_B dt d\varphi} = \frac{\alpha_{em}^3}{8\pi} \frac{1}{4x_B M_p^2 E_{lab}^2} \frac{1}{\sqrt{1+4x_B^2 M_p^2/Q^2}} \left|\mathcal{T}_{BH} + \mathcal{T}_{VCS}\right|^2 \tag{2.35}$$

$$\left|\mathcal{T}_{BH} + \mathcal{T}_{VCS}\right|^2 = (\mathcal{T}_{BH}+\mathcal{T}_{VCS})*(\mathcal{T}_{BH}+\mathcal{T}_{VCS}) = \mathcal{T}_{BH}^2+\mathcal{T}_{VCS}^2+\mathcal{T}_{BH}^*\mathcal{T}_{VCS}+\mathcal{T}_{BH}\mathcal{T}_{VCS}^*$$

The differents terms can be expressed in terms of a linear combination of Compton Form Factor. Using the same notation as Diehl [29] equation (356), in

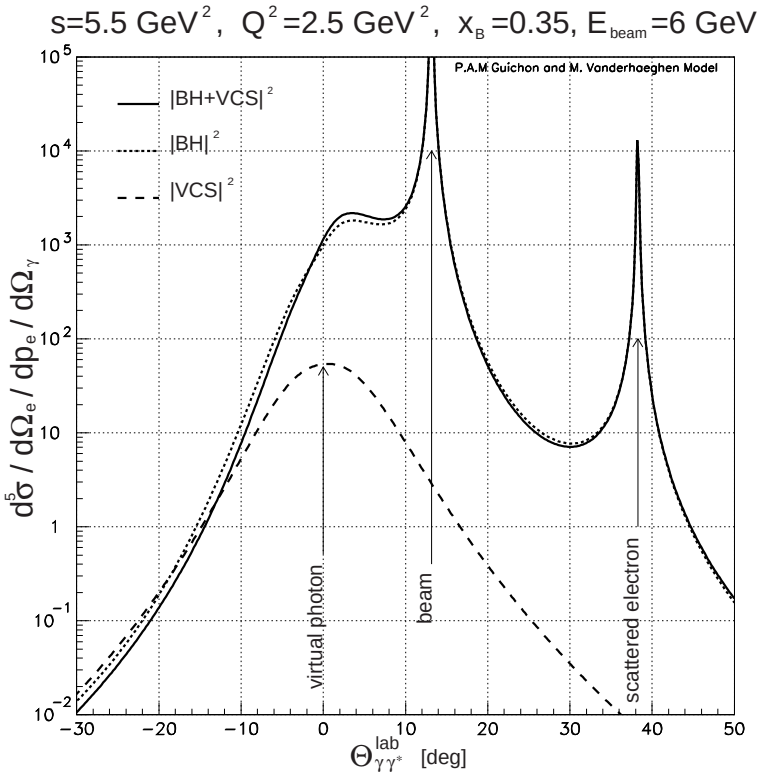

Figure 2.6: Electroproduction simulated cross section by Guichon et al. [46]

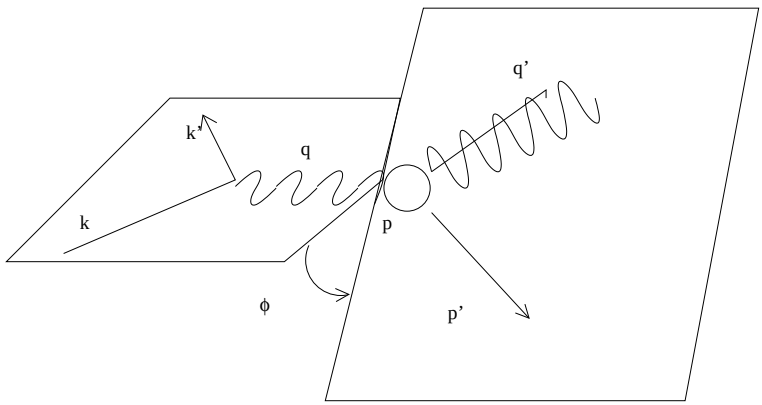

Figure 2.7: Definition of ϕ the angle between the leptonic and hadronic plane

our case we look at the interference term :

We define s' and u' coming from the progators of the Bethe and Heitler diagrams.

$$
\begin{aligned}
y &= \frac{k.p}{q.p} \\
s' &= \frac{Q^2}{y}\left[1 - \frac{2\sqrt{1-y}\sqrt{t_0 - t}}{Q}\sqrt{\frac{1-\xi}{1+\xi}}\cos\phi\right] + O(t, m^2) \\
-u' &= \frac{Q^2}{y}\left[1 - y + \frac{2\sqrt{1-y}\sqrt{t_0 - t}}{Q}\sqrt{\frac{1-\xi}{1+\xi}}\cos\phi\right] + O(t, m^2) \\
P &= \frac{-s'u'}{(1-y)y^{-2}Q^4} \\
P(cos\phi)\frac{d\sigma_{INT}(ep \to ep\gamma)}{d\phi dt dQ^2 dx_B} &= \\
& c_0 + c1\cos\phi + c2\cos 2\phi + c3\cos 3\phi + P_l(s_1\sin\phi + s_2 sin2\phi)
\end{aligned}
\tag{2.36}
$$

We see from 2.36 that by making the difference of cross sections for two beam helicities denoting $\vec{\sigma}$ when the electron spin is in the same direction as the electron momentum and $\overleftarrow{\sigma}$ we access to the interference term.

$$
\begin{aligned}
P(\cos\phi)\left[\frac{d\vec{\sigma}}{d\phi\, dt\, dQ^2\, dx_B} - \frac{d\overleftarrow{\sigma}}{d\phi\, dt\, dQ^2\, dx_B}\right] &= \\
& A\sin(\phi) + B\sin(2\phi)
\end{aligned}
\tag{2.37}
$$

The factor A is a linear combination of GPDs and B allows to determine the higher twists contribution.

2.5.2 Meson electroproduction crossection

The Deep Meson Electroproduction is similar to the DVCS but with a meson in the final state instead of the real photon. The electroproduction of meson is a rich reaction, it is sensitive to the flavor decomposition of the GPDs. The drawback is that they introduce the additional hadronic function of the produced meson making the extraction of the GPDs less straightforward. Several estimations of pions cross sections are available for π^0, $\pi^{\pm}$, ω and ρ [45] and many experiment in Hall B at Jefferson Laboratory have studied some of the reactions ω production [68] and ρ [48] production.

2.6 Experimental difficulties

2.6.1 Physical background

Depending on the experimental setup different kind of background. Since we are in the DIS (Deeply inelastic Scattering) regime many particles can be produced in the final state so the measurements in DIS are inclusive where only the scattered electron is detected. With the progresses made in detectors and in the accelerator field allowing higher luminosities, it has become possible to focus on one particular final state of the DIS by making an exclusive measurement of all the particles in the final state. A good example of this statement can be found for example in figure 2.8 from [22] which illustrates some exclusive processes selected among the Deep Inelastic Scattering.

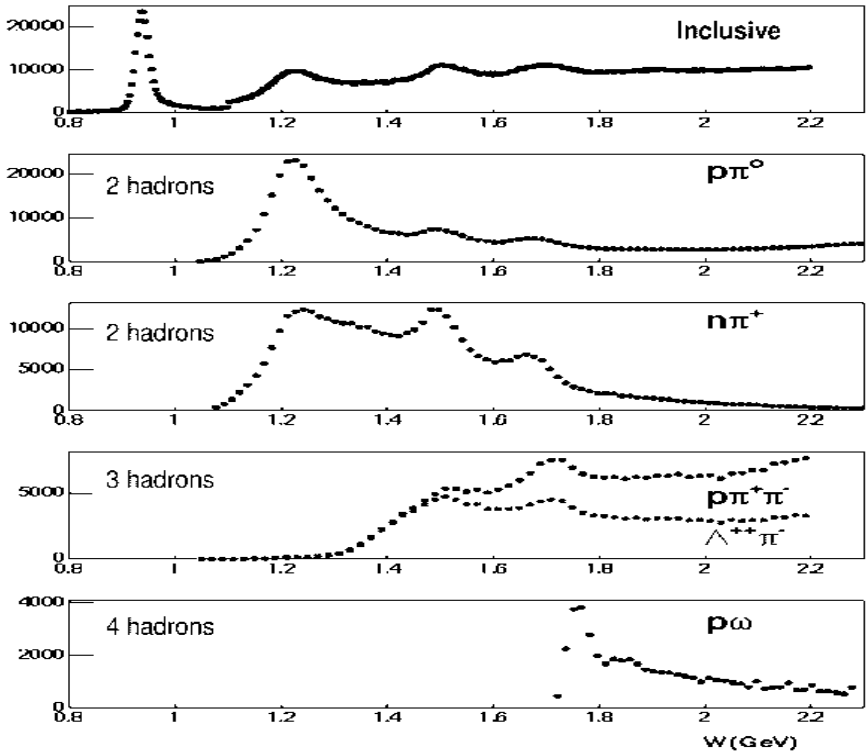

Figure 2.8: Example of some exclusive processes within the Deep Inelastic Scattering from data from Hall B CLAS detector

Since we are interested in the DVCS process all other reactions can be considered as a physical background which has to be dealt with. Particularly,

- π_0 production is a background difficult to handle especially when the missing particle is the photon which mass is 0. When one photon from its decay is not detected, the second photon can be misidentified with a DVCS photon.
- Associated pion production is similar to the DVCS process but with an excited state of the proton in the final state which re-decays into a proton and the emission of a pion (π^0or π^+)

$$ep \rightarrow e\gamma \quad \Delta \tag{2.38}$$
$$\hookrightarrow \quad \pi N \tag{2.39}$$
$$\tag{2.40}$$

  The major problem for this reaction is like the DVCS it has an associated Bethe Heitler process which enhances its crossection. So the detection of all the particles of the final state is a necessity to discriminate them from the real DVCS events if the resolution on the missing particle is not sufficient.

2.6.2 Experimental background

Since we are mostly interested in the interference term of the BH and the DVCS, it is interesting to look close from the BH pole in order to benefit from the crossection increase to maximize the counting rates. This means that the more forward the particles are detected the better. The drawback is background is also increasing when going at forward angles, especially coming from electromagnetic processes such as Moller scattering making the measurement of DVCS a challenge.

2.7 First evidences of DVCS events

The German laboratory Deutsch Elektronen Synchrotron (DESY) has several experiments running. Two experiments on the HERA electron proton collider H1, ZEUS and the HERMES experiment were able to detect DVCS events among the data. Another feature of HERA is the availability of a positron beam allowing to look at the beam charge asymmetry.

2.7.1 HERA

HERA is the first electron proton collider using 27.6 GeV electron on 820 GeV proton beams giving a center of mass energy of about 300 GeV. The integrated

luminosity reached $1.5 * 10^{-31} cm^{-2} s^{-1}$. Detailed informations can be found in Rainer Stamen thesis [77] for the H1 experiment. The two detectors H1 and ZEUS, located at one proton-electron interaction point have a similar design with an almost 4π acceptance. At these energies DVCS events occur at very low values of $x_{bjorken}$ ($10^{-2}...10^{-4}$). In such kinematics DVCS protons get very low transverse momentum and escape from the detector along the beam line. Measurements gave the trend for the Q^2 and W evolution of the electroproduction cross section. A complete description of the analysis and of the detectors can be found in Iwona Grabowska-Bold's thesis [43] for ZEUS.

2.7.2 HERMES

HERMES is located at DESY but unlike H1 and ZEUS uses a fixed polarized gas target. So HERMES spectrometer is a forward spectrometer very well equipped to detect electromagnetic particles but like on HERA the proton could not be detected. More information about the detector can be found in James Ely thesis [33]. HERMES experiment is the only facility featuring a positron beam allowing to access the beam charge asymmetry. HERMES published the asymmetry done selecting DVCS events[5] this work was one of the first DVCS result.

2.7.3 Hall B

The Hall B at Jefferson Laboratory is equipped with the 4π spectrometer CLAS (Cebaf Large Acceptance Spectrometer). Using large drift chambers [65] and different detectors associated with toroidal magnetic field the CLAS detector can detect charged particles and neutral particles. Hall B can either work with a tagged photon beam or with electrons. On the electron data taken with a rather loose trigger, one can investigate any final state offline. But the standard CLAS configuration is not optimized for DVCS especially because of the lack of calorimetry at forward angle where most of the real photons coming from DVCS are. So the DVCS process was studied without detecting the photon by using the missing mass technique. The moderate resolution of CLAS made it difficult to separate the DVCS photons from the π^0 background. But using a fit on the two distributions and simulation, a first DVCS asymmetry could be extracted.

E1d in Hall B ran from February 4th to March 2nd 2000. It was the subject of Gagik Gavalian thesis [38]. Since CLAS has a toroidal magnetic field associated with wire drift chamber it is very well suited to detect charged particles. So an analysis was made to study the DVCS with the photon as the missing particle. Due to the resolution the photons were contaminated by the π^0 but using a fit method the DVCS signal was extracted. And the article about this analysis [78] was published at the same time as the HERMES ones.

2.8 New set of experiments ensuring the exclusivity of the reaction

2.8.1 Exclusivity

These experiments had very encouraging results but since the exclusivity could not be assured, there is no way to be sure that non exclusive reaction such as Delta VCS production or accidental with one photon from a π^0 do not contribute. A good way to sort out the DVCS events is to over constrain the reaction by detecting all the particle on the final state.

$$e + p \rightarrow e + \gamma + X$$

Making sure that the missing particle is in the same plane as the virtual photon and the real photon will ensure that only one particle is produced since the additional particle will most likely change the acoplanarity.

2.8.2 Hermes

After the first results a proton recoil detector has been added to the HERMES detector for the 2005 2007 data taking period. It consists of a two layer silicon detector associated with scintillating fiber and a photon detector more information about this detector can be found in [76]. Recoil protons momentum will range 0.1 GeV/c to 1.5GeV/c.

2.8.3 Jefferson Laboratory Hall B

The experiment E01-113 [80] ran from March 2005 to May 2005. It added specific elements to the existing CLAS detector : a forward lead tungstate calorimeter of 424 blocks covering angle from 3 degrees to 12 degrees and a solenoidal superconducting magnet. This allowed to ensure the exclusivity Hall B was lacking in the previous data taken and also to run at an increased luminosity of $2 \cdot 10^{34}$ while also detecting the real photon. This experiment took full advantage of the CLAS 4π detector allowing a large kinematical coverage.

2.8.4 Compass

The Compass experiment is the successor of SMC at CERN. It uses a muon beam with energies of 100 or 190 GeV associated with the COMPASS detector. The DVCS at COMPASS [28] will use the muon beam energy at energies of 100 or 190 GeV. This experiment has many advantages :

- DVCS becomes dominant over the BH allowing a direct measurement of the DVCS cross section.
- the energy allows a good kinematical coverage : Q^2 in [1.5,7] GeV^2 range and x in [0.03,0.25] range.
- the muon beam can be available in both charges and two polarizations this would allow to make a direct measurement of the real part of the DVCS amplitude

Expected luminosity is $10^{32} cm^{-2} s^{-1}$. An extensive work by Laurent Mosse on simulations and test for the COMPASS setup is available in his thesis [69] The experiment would start after the completion of the COMPASS experiment [3] in 2010.

2.9 Summary of the experiments features

The same way as it took several years and experiments to measure the unpolarized and polarized structure functions, constraining the GPDs will need many different measurements in order to disentangle all of them. The different features of the DVCS experiments are summarized in the following table.

Facility	Beam	Target	T Pol	Lum $cm^2 s^{-1}$	Energy GeV	x_B	$Q^2(GeV^2)$ (GeV^2)
HERMES	e^+e^-	H,D	Yes	10^{32}	27	0.3-0.5	2-4
HERA	e^+e^-	ep $collider$	no	10^{30}	$27GeVe^-$ $860GeVp$	$10^{-4} - 10^{-2}$	$2 - 20$
JLab Hall A	e^-	H,D	no	$2 \cdot 10^{37}$	5.75	0.35	1.5-2.32
JLab Hall B	e^-	H,D	NH3	10^{34}	5.75	0.1-0.6	1-4
Compass	$\mu^+\mu^-$	H	no	10^{32}	100-190	0.03-0.25	1.5-7

As we can see the study of the DVCS requires to find a balance between luminosity, acceptance and kinematical coverage. So two different approaches are possible :

- Large acceptance detectors : Hall B for example has a large coverage but a lower luminosity and a moderate resolution on the detected particles. This allows to cover large kinematical range with moderate statistic though.
- small acceptance and high luminosity experiments such as the one in Hall A give. This allows to make measurements with high statistics but on points with small kinematical coverage : for example 3 measurements at the same x_B were made at 3 different values of Q^2 during this experiment.

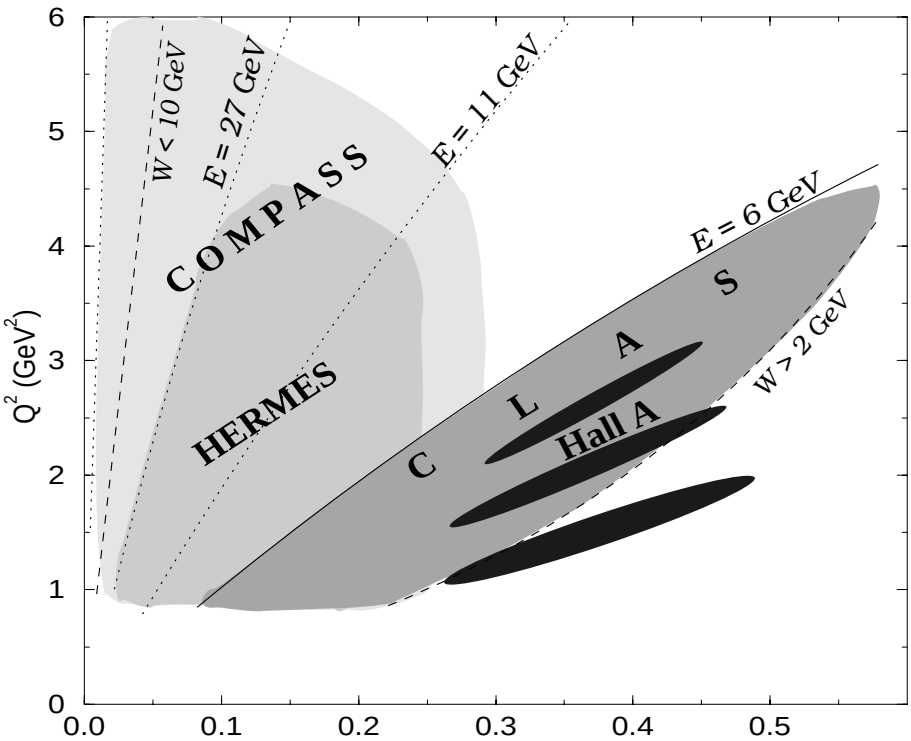

Figure 2.9: DVCS kinematical coverage with available facilities

The DVCS was explored already in a pretty broad kinematical range of experiments. And more are to come since the extraction of all the GPDs will require many different measurements.

Chapter 3

DVCS in Hall A

The experiment E00-110 was the first dedicated experiment to study DVCS and was setup in Hall A at Jefferson Laboratory. After introducing the major features of the laboratory and Hall A, I will discuss about the detector design and the specific background issues for the experiment.

3.1 Overview of Jefferson Laboratory accelerator

Jefferson Laboratory (JLAB) is located on the Eastern Coast of the United States in Newport News (Virginia) about 300 kilometers south from Washington DC. This laboratory hosts an accelerator and three experimental physics halls : the two high luminosity halls equipped with high precision - small acceptance spectrometers for inclusive and semi-inclusive measurements : Hall A [6] with two identical high resolution spectrometers (HRS) and Hall C with the high momentum spectrometer (HMS) [10] and the short orbit spectrometer (SOS) [53]. Hall B with the CLAS detector a nearly 4π detector [24] [65] [64] particularly well suited for exclusive measurement such as meson spectroscopy.

3.1.1 Accelerator

JLAB is one of the first continuous electron beam facility using superconducting cavities. The accelerator is constituted by two linear accelerators (LINAC) and 5 recirculation magnetic arcs allowing to deliver from 1 to 5 times the energy of the linac into any of the three experimental halls. Unlike room temperature cavities where the beam has to come by bunch in order to leave time for the klystron to store energy for the next bunch the superconducting cavities allow to run at a frequency of 1497Mhz which can be considered as continuous regime.

This translates into a higher duty cycle and less transient states giving a very stable beam. The beam is distributed at the beam switch yard (BSY) where it is separated between the three experimental Halls. Each of them thus effectively receives electrons bunches at a 499 MHz frequency.

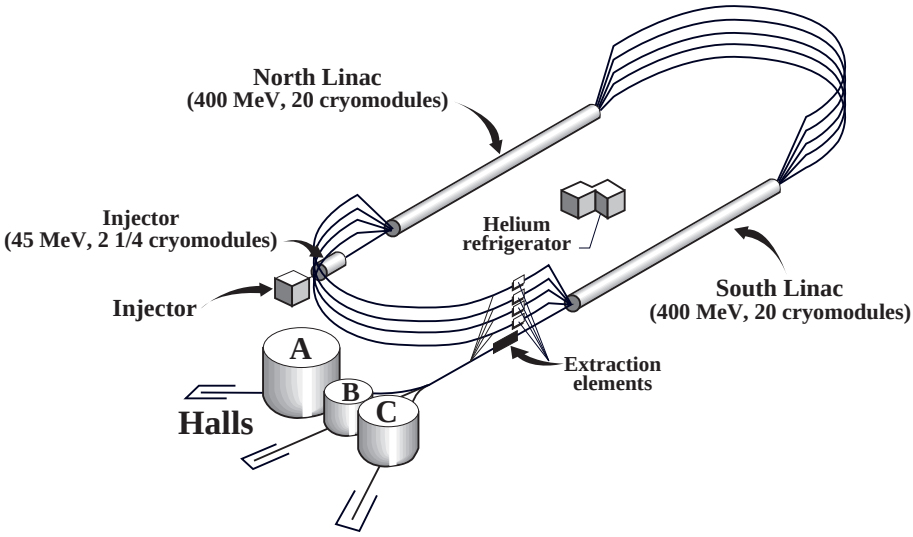

Figure 3.1: Accelerator setup

3.1.2 Injector

This high duty cycle allows to study reaction with low cross section in a reasonable time. A typical luminosity value in Hall A is $10^{38} cm^{-2} s^{-1}$ allowing measurement such as hypernuclear spectroscopy, parity violation or virtual Compton scattering. Another feature of Jefferson Laboratory is the polarized electron source which allows to obtain longitudinally polarized electron beam. Depending on the photocathode used polarization values can reach up to 85%. But the highest polarization source being still in development, the quantum efficiency was a problem so the regular strained layer As-Ga was used since Hall C needed high current : so polarization of the electron beam for this experiment was around 77%. The electrons are produced by using the polarized light of a laser on a photocathode at the injector, details about the injector can be found in parity violation thesis such as Maud Baylac's thesis [12]. In order to reduce the sytematics error for experiments using polarized beam and limits depolarization effects for polarized target experiments. The laser polarization is reverted at 30 Hz frequency using a pockel cell. The beam polarization is thus flipped at the same frequency. This signal is sent to the different counting house to be recorded.

3.2 Hall A standard equipement

Hall A at Jefferson Laboratory is one of the two high luminosity hall. It is equipped with two high resolution spectrometers. It is dedicated to experiments requiring a excellent resolution on one of the outgoing particle (10^{-4} on momentum).

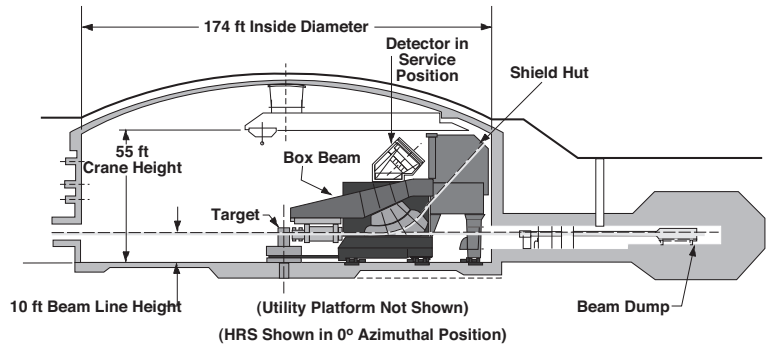

Figure 3.2: Hall A layout

3.2.1 Beamline equipement

Energy measurement ARC measurement [6] Berthot et al. [16] this measurement uses the dipoles from the arcs which deliver the beam to Hall A. By measuring the deflection of the beam one can access to the energy with an accuracy of 6.8.10-5 at 4 GeV.

Beam position monitor The beam position monitors are four antennas placed around the beam. They provide a relative mesurement of the beam position. They are calibrated with respect to the HARP.
The HARP are thin wires that can be moved into the beam. Their absolute position being measured absolutely by the mean of survey they allow to deduce the beam position.

Beam current measurement (BCM) The BCM is a passive cavity similar to the one from the accelerator. The beam going into it excites it and generates a voltage proportionnal to the current. Two cavities are used in Hall A for measurement of the beam current. Their voltages are converted to frequencies and sent to scalers to be recorded in the data.

Polarimetry

Moller polarimeter The Moller polarimeter Fig. 3.3 is using a foil of iron polarized through a magnetic field. The measured asymetry of the Moller scattering allows to determine the beam polarization. The Moller Polarimeter has

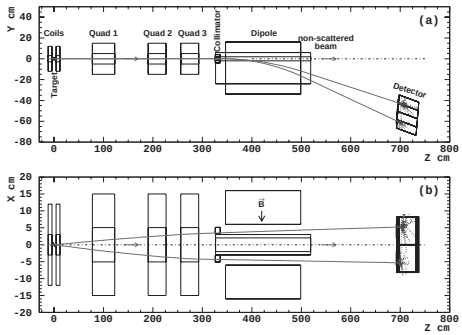

Figure 3.3: Moeller polarimeter setup

to run at low current around 0.5 μA and needs a dedicated run, but has the advantage to be sensitive to the sign of the polarization.

Compton polarimeter The Compton polarimeter [34, 11] uses the backscattering of electrons from photons. It can be decomposed into different parts :

- a magnetic chicane
- a high finess Perot Fabry cavity associated with a laser
- a silicon strip electron detector
- a lead tungstate calorimeter

The magnetic chicane is constitued by four dipoles mounted into a chicane allowing to take the electron beam vertically out of the horizontal plane without changing the beam properties on the target. It allows to tune the electron beam in order to cross the point of the cavity where the amplified light has the maximum power (around 1200 Watts) optmizing the Compton counting rates. After going through the cavity the electron beam is brought back to regular beamline. The last dipole set also acts as a spectrometer for the electron, indeed electron which have interacted with a photon have lost energy and will be more deflected than the initial electron beam : these electrons will be detected by the electron detector. The Electron detector is made of 4 planes of silicon strips detectors which allow

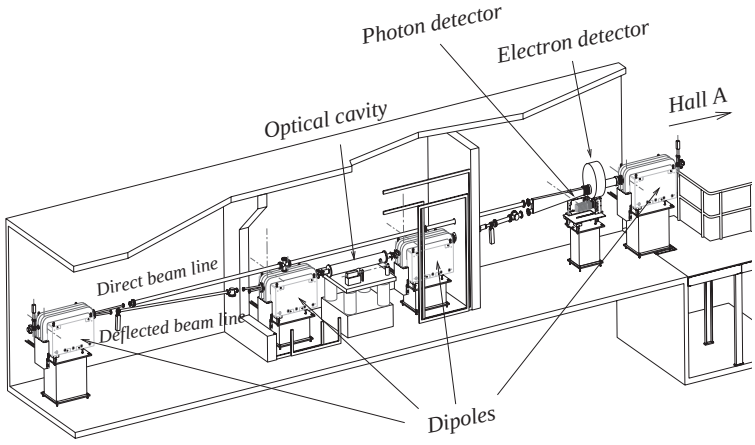

Figure 3.4: Compton polarimeter setup

to determine the electron energy. The scattered photon will be boosted forward and detected into a 5 by 5 lead tungstate calorimeter.

This allows a continuous measurement of the beam polarization during the experiment.

3.2.2 Target

cryogenic liquid hydrogen target The Hall A has 3 different standard targets available the Waterfall target for experiment on Oxygen, the polarized Helium 3 target for the study of the neutron spin structure and the cryogenic target. For this experiment we used the cryogenic target. This target has 3 cryogenic loops available but for space constraints reasons with the new scaterring chamber only 2 were available for the DVCS experiment. One was used for liquid hydrogen and the other one for liquid deuterium. Using the motorized target ladder we have a vertical motion allowing to switch from one target to the other. Target configuration for the experiment was :

Target
4 cm LD2
15 cm LD2
4 cm LH2
15 cm LH2
Optics seven 1 mm thick carbon foils
4 cm dummy $\pm 2cm$ Al foils
15 cm dummy $\pm 7.5cm$ Al foils
Cross hair Al 1 mm thick
BeO viewer 1mm thick
C 1 mm thick carbon foil
Empty target

For all the cryogenic loops and dummy target the windows are in aluminium with a thickness of 0.102±0.02 mm for the entrance window and 0.127±0.02 mm. The liquid hydrogen target si operated at the temperature of 19K with a pressure of 0.17MPa giving a density of 0.0723 g/cm^3 [2]. This target receives enough cryogenic cooling power to receive up to 600W power deposition by the beam since it can take up current up to 120 μA using a rastered beam reduce target fluctuations. For the DVCS experiment we ran at a maximum current of 3μA which allowed us to run without raster since boiling effects are negligible with such a low beam current. With this parameters we can compute the instantaneous luminosity :

$$Lu = \frac{I}{e} L_{targ} * \mathcal{N} * \frac{\rho_H}{M_p} = 2.5 \cdot 10^{-6}/1.6 \cdot 10^{-19} * 6.02^{23} \cdot 0.07229 \cdot 15 = 10^{37} cm^2 s{-}1$$

3.2.3 Hall A spectrometer

Description and characteristics

The spectrometers in Hall A consists in superconducting magnets : 3 quadrupoles (Q) and the dipole (D) in a configuration QQDQ. This configuration allowed to reach the required performances for the spectrometer :

For the DVCS experiment the Left Arm was used to detect the scattered electrons and thus defines the kinematic of the virtual photon.

Detector stack

The detector stack of the spectrometer has two purposes : the reconstruction of the particles trajectory in order to reconstruct the interaction point and the particle momentum and to perform the particle identification.

Table 3.1: Main design characteristics of the Hall A High Resolution Spectrometers. The resolution values are for the FWHM.

Configuration	QQD$_n$Q Vertical bend
Bending angle	45°
Optical length	23.4 m
Momentum range	0.3 - 4.0 GeV/c
Momentum acceptance	-4.5% < δp/p <+4.5%
Momentum resolution	1×10^{-4}
Dispersion at the focus (D)	12.4 m
Radial linear magnification (M)	-2.5
D/M	5.0
Angular range HRS-L	12.5° - 150°
HRS-R	12.5° - 130°
Angular acceptance: Horizontal	±30 mrad
Vertical	±60 mrad
Angular resolution : Horizontal	0.5 mrad
Vertical	1.0 mrad
Solid angle at δp/p = 0, y_0 = 0	6 msr
Transverse length acceptance	±5 cm
Transverse position resolution	1 mm

Trigger scintillator The triggering is made by two scintillator planes.

S1 S1 array is constituted by 6 scintillator paddles of 5mm thick BICRON 408 scintillator

S2m S2m is a scintillator array made of 16 BICRON plastic scintillator paddle of dimensions. Each paddle is read-out by a PMT at both ends.

Vertical Drift Chamber The spectrometer resolution depends directly on the quality of the tracking of the particle. The trajectory of the particle is reconstructed by the Vertical Drift Chamber. The VDC has two UV planes for a total of 368 wires [6]

Particle identification

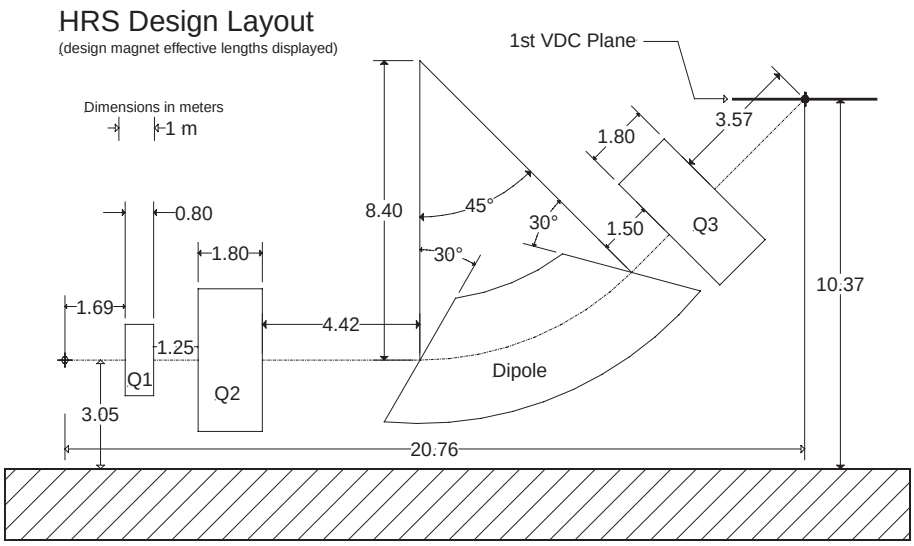

Figure 3.5: Spectrometer magnet layout

Gas Cerenkov Each spectrometer of Hall A can be equipped with different types of Cerenkov detector. In order to discriminate the pions from the electrons the CO_2 Gas Cerenkov counter was used in the electron arm. It is constitued of a 150 cm long CO_2 radiator and 10 spherical mirrors collect the light from the Cerenkov cone and each focuses it on a PMT. More details can be found in [52]. The CO_2 has a refractive index n=1.00041 giving a cerenkov threshold for the electrons of 0.017 GeV/c while it goes up to 4.8 GeV/c for pions. Since light output was determined to be 9 photoelectrons the signal of the 10 PMTs is summed analogically. A discriminator on this signal produces the cerenkov signal.

Pion rejector The pion rejector is situated at the back of the left spectrometer detector stack. It is made of 2 layers of 34 Lead glass blocks. Using the energy loss in these two layers, we can discriminate between electrons which will shower in the detector yielding a large amount of energy in the detector and pions which will only make energy loss in the detector.

DVCS spectrometer configuration For the DVCS experiment we used the two HRS, the left spectrometer was used mostly for electrons with the following configuration.

- VDC

- S1
- Long Gas Cerenkov
- S2m
- Pion rejector

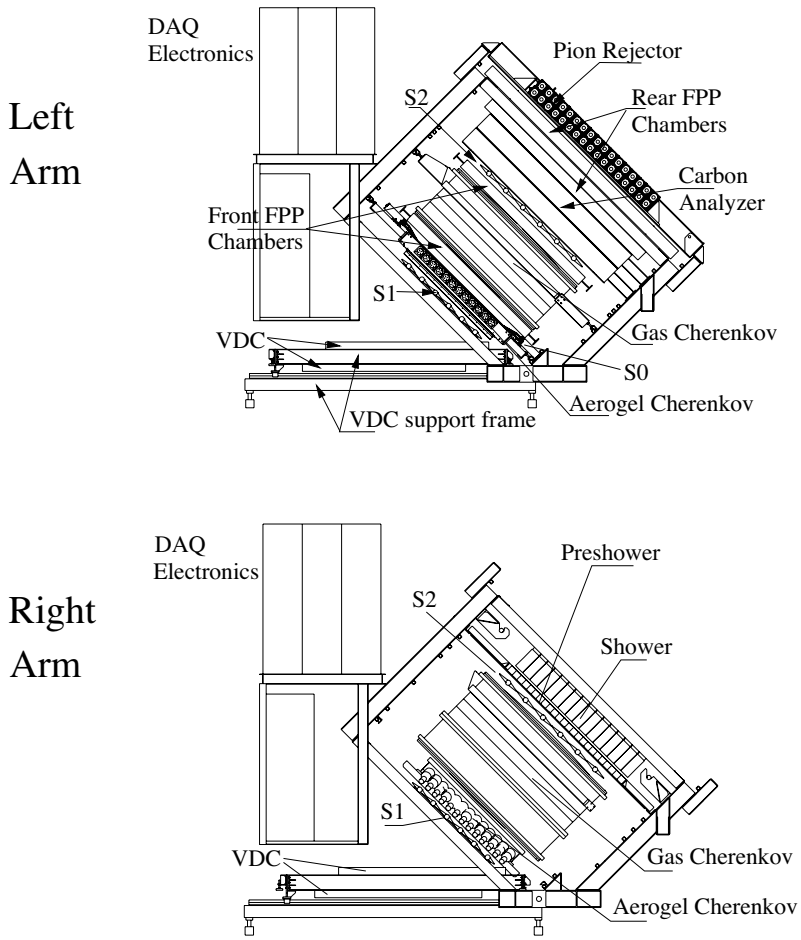

Figure 3.6: Spectrometer detector stack

This configuration allowed good pion electron rejection.

The right arm only had the VDC and the trigger scintillators S1 and S2m. This was sufficient since it was used as luminosity detector so only triggers counting rates were used.

Hall A was chosen for the DVCS in order to have a high accuracy on the scattered electron and to be able to select particular kinematic points allowing to accumulate a good statistic there. Moreover the angular resolution of the calorimeter depends on the determination of the vertex so the spectrometer performances also improve the resolution on the real photon.

3.3 Specific equipment

3.3.1 Detectors design

The design of this experiment has a different approach from what was done previously. All the previous experiment were using large acceptance detectors. Even though the DVCS reaction is mostly interesting for events being out of the scattered electron plane the 4π detectors are often limited in luminosity. For this experiment a compromise on the acceptance for the outgoing photon and proton was made in order to be able to optimize the luminosity and the acceptance of both detectors. Simulation were carried out in order to determine the acceptance needs. This has driven both the designs for the calorimeter and the proton array. I will summarize in this section the physics and practical constraints which drove the detector design.

Simulation

The following simulation made for the DVCS experiment proposal [35] is summarizing the parameters which drove the designs of the calorimeter and the proton array.

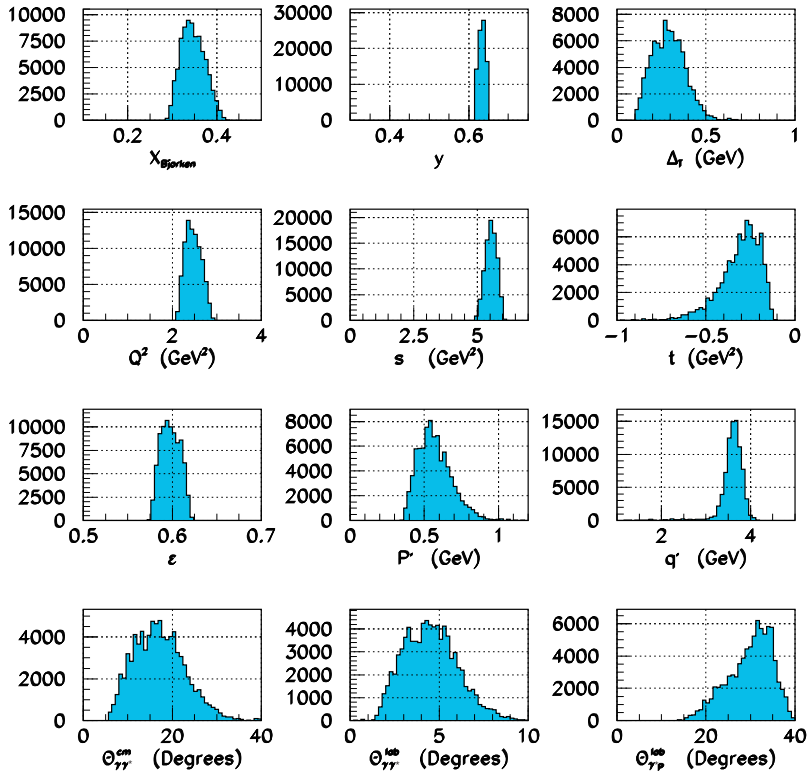

Figure 3.7: Histograms of main physics variables after all analysis cuts for the kinematical point.

The kinematical parameters of the simulation for these plots are : s=5.5 GeV^2, Q^2=2.5 GeV^2. $x_{\rm Bjorken} \equiv x_B = Q^2/(2M_p\nu)$; $y = \nu/k$; Δ_T = component of $\vec{p}' - \vec{p}$ transverse to $(\vec{p}' + \vec{p})/2$; $Q^2 = -q^2 = (k - k')^2$; $s = (q + p)^2$; $t = (q - q')^2$; $\epsilon = 1/[1 + 2(\vec{q}^2/Q^2)\tan^2(\theta_e/2)]$ = virtual photon polarization; p' = recoil proton laboratory momentum; q' = final photon laboratory energy; $\theta^{\rm cm}_{\gamma\gamma^*}$ = angle between final photon and $\vec{q}$ direction in CM frame of final photon and proton; $\theta^{\rm lab}_{\gamma\gamma^*}$ = angle between final photon and $\vec{q}$ direction in lab frame; $\theta^{\rm lab}_{\gamma' p}$ = angle between final proton and $\vec{q}$ direction in lab frame.

The most interesting parameters for the detector design are the angular distributions for the real photons and the protons.

3.3.2 Electromagnetic calorimeter

In the original proposal the DVCS experiment was supposed to use the Real Compton Scattering calorimeter experiment but for different reasons such as space

constraint, solid angle, granularity and we had time on hand since the schedule would not allow to run the experiment due to the incompatibility on beam energy with the G0 experiment, we choose to build a dedicated calorimeter.

Lead fluoride calorimeter

Calorimeter requirements The calorimeter is the central part of the DVCS experiment since its resolution is the major limiting factor on the experiment resolution. The calorimeter had to fit the following requirements :

- good energy resolution
- good radiation hardness
- compactness
- sensitivity to background
- mechanical simplicity and ease for alignment

Two types of crystals are available : lead tungstate and lead fluoride (PbF_2 have similar physical properties.

Density	7.77 $g.cm^3$
Radiation length X_0	0.93
Moliere radius	2.2 cm
Refraction index	2.05

The lead fluoride PbF_2 is very dense crystal allowing a very compact calorimeter. The length of the blocks was taken to 20 radiation lengths giving a total length of 18.6 cm. PbF_2 emits light only from Cerenkov process unlike Lead Tungstate which is a scintillator. This has two advantages : it makes it insensitive to background of particle of $\beta < \frac{c}{n} = \frac{1}{2.05} = 0.487$ corresponding to electrons of energy lower than 80 KeV which cuts a part of the low energy background. Moreover the light pulse is much shorter than for scintillators making easier pulse separation in case of pile-up as shown in fig. 3.8. Following the study done by Kozma [58] we choose to get lead fluoride crystals from Shanghai Institute of Ceramics, Chinese Academy of Sciences (SICCAS) which seemed to show the best radiation hardness.

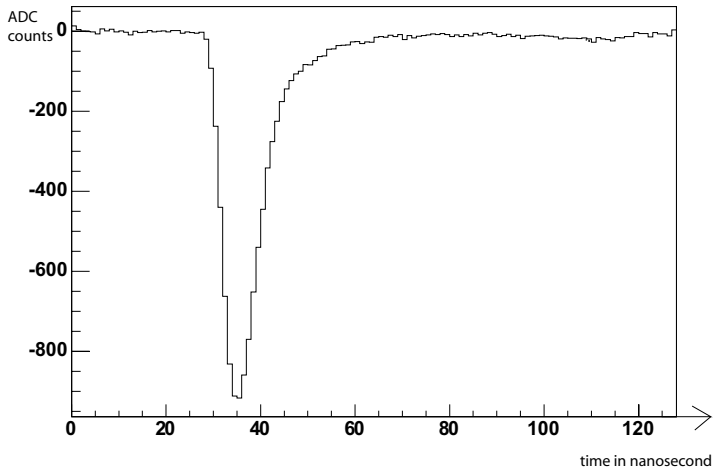

Figure 3.8: Typical signal from the calorimeter recorded with the sampling system

Calorimeter geometry

From the simulation we see that real photons coming from the DVCS are emitted in the laboratory frame from 1.5 degrees to 10 degrees from the virtual photon which points in the center of the calorimeter. For the calorimeter we choose Hamamatsu R7700 8 stages PMT. For reference these PMTs are a 8 stages version of the R5900 U PMT which is declined in several multianodes versions. These PMTs have the advantage of being very compact and very fast, they come in a form factor 25.7mmx25.7mmx22 mm, so with the conventional choice of 20 radiation lengths to contain the shower this has fixed the block size to (3cmx3cmx18.6cm). To facilitate the mechanical design of the device, the geometry was chosen rectangular in an 11 columns by 12 rows of PbF_2 blocks. This size covers an angle $\theta_{\gamma\gamma*}$ up to 8.5 degrees at the designed distance of 1.1 meters from the target which covers most of the DVCS photons phase space.

The calorimeter was designed modularly, each block was coupled to a PMT using a tightening fixture in brass. This fixture was constituted by :

- a copper cubic carved piece to hold the PMT and the block in place.
- a front face plate with a hole to leave the light from the gain monitoring system passing through.
- a brass foil to link which was soldered to the front and the back piece

Each PbF_2 block was wrapped with one layer of Tyvek [57] and another one of black tedlar and encased in the brass part and tightened. Once the block were all

assembled they were stacked into the calorimeter box. A small bus was designed for each calorimeter column in order to supply the HV, the DC current for the amplifier, the monitoring of the anode current and a support for the signal cable. HV, DC voltage and anode current monitoring were carried out using flat ribbon cables.

3.3.3 Proton Array

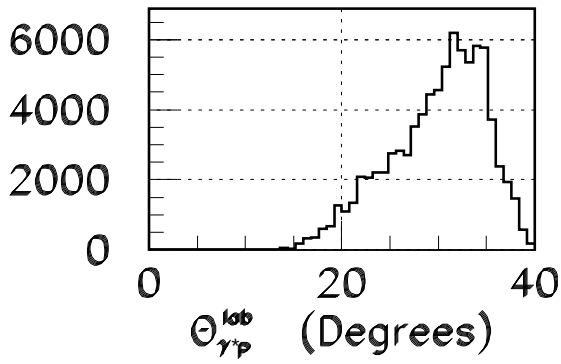

Figure 3.9: Foreseen angular proton distribution

Detector design The proton array was designed to detect most of the DVCS protons without interfering with the calorimeter. The detector covers angle $\theta_{\gamma * p}$ from 18 to 38 degrees. It is composed of 20 modules (which will be referred as tower) covering an angle phi of 270 degrees : though protons go beyond this angle a part of the phi angular acceptance had to be cut in order to leave room for the beam pipe. Each module is constituted by 5 scintillator blocks. At the smallest angle kinematic the blocks closer to the beam will be at an angle θ of 15 degrees. The blocks used were scintillator from Eljen technology EJ400 coupled to Photonis XP2972 phototubes each block covering an angle of 4 degrees in theta.

3.3.4 Mechanical assembly

Calorimeter box and support The two detectors were mounted together by the mean of an aluminum support structure allowing to have the proton array and the calorimeter centered. This plate made the connection of the calorimeter

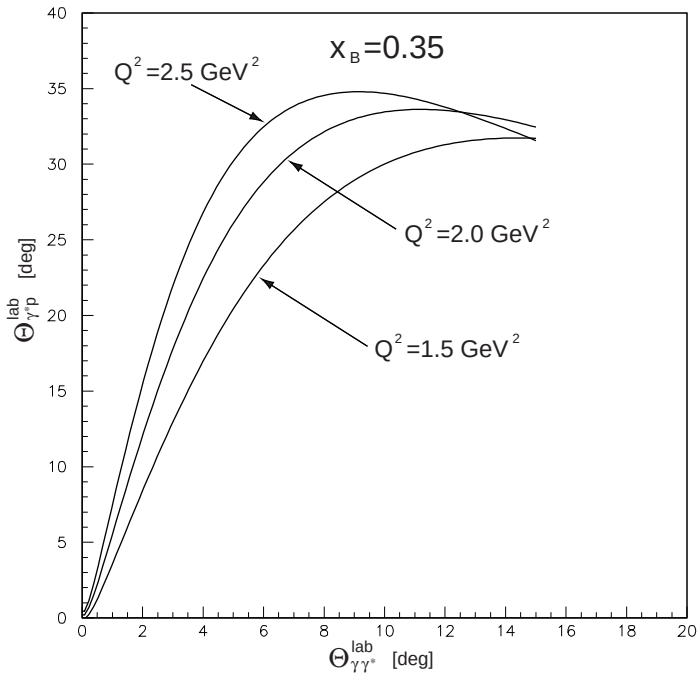

Figure 3.10: Corresponding proton angle versus photon angle

support and the proton array. The kinematic of the virtual photon being defined by the spectrometer makes its direction pointing toward the center of the detector. The plate was bolted to the support structure which constituted the black box for the calorimeter and was holding the support of the calorimeter. The black box support also hosted the LED system which will be developed in part 5.1.2. In order to have the maximum solid angle covered by the calorimeter it had to be as close as possible from the scattering chamber leaving no room for the gain monitoring system. The LED system was installed on the supporting aluminum plate and a linear motion was allowed in order to be able to move back the calorimeter. In this position the LED could move in front of the calorimeter at a distance of 4.5 mm from the surface of the face of the calorimeter.

Proton array assembly Each scintillator block was glued with RTV to an aluminum piece which holds the PMT with the scintillator block. Once glued the scintillator was wrapped and the PMT could be put in place with the mu-metal. Once all the blocks were glued and wrapped they were put together in tower : 5 modules were put together on a long piece of aluminum held together by a belt. This piece was designed to support the 5 scintillators blocks and to be bolted on the central piece.

Support structure In order to allow the calibration of the calorimeter using elastic events the detector was placed on rails allowing a motion along the z-axis allowing to match the spectrometer acceptance. The DVCS detector was fitted on the stand designed for another standard spectrometer in Hall A called Big Bite. It allowed an accurate positioning of the DVCS detector.

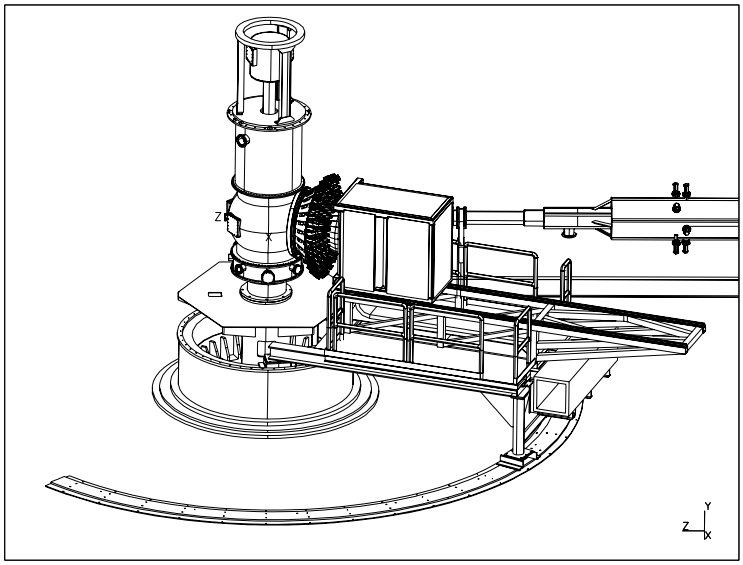

Figure 3.11: DVCS stand in Hall A

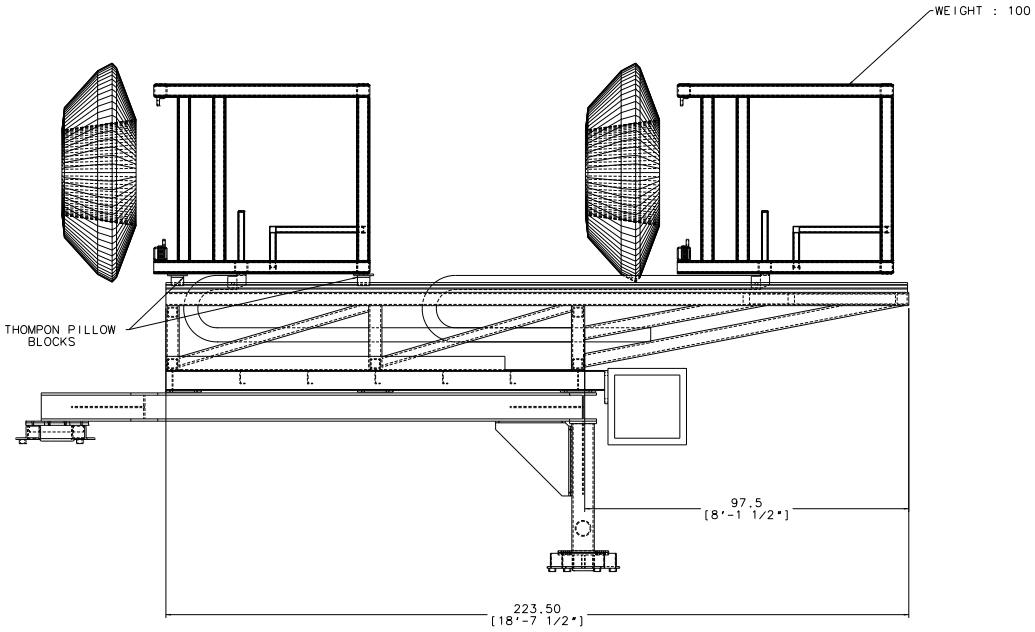

Figure 3.12: Side view of the DVCS stand

3.3.5 Hall A DVCS specific background issues in Hall A

The background is the major issue for DVCS. This is especially the case for Hall A DVCS experiment since it was designed to run at a luminosity of $10^{37} cm^{-2} s^{-1}$. Usually only small acceptance spectrometers are used in Hall A so background was never really an issue. For this experiment large acceptance detectors are in direct view of the target making them very sensitive. Background was studied through simulations, in beam tests and in the final data themselves. Equipment were designed keeping in mind they would run in a hostile environment.

Background effect

Two different kinds of background affect the detectors. High energy background produces pile-up events with the real signal so this has also to be taken care in order to extract the correct energy. The solution chosen was instead of using regular integrating ADC to use a sampling system. A custom electronics was developed allowing to sample at 1 GHz rate up to 128 ns : this allows to actually record the whole waveform of the signal coming out from the PMT the same way as a digital oscilloscope allowing to perform off-line waveform analysis in order to process the pile-up events. This will be developed in 6.2.1 Simulations on

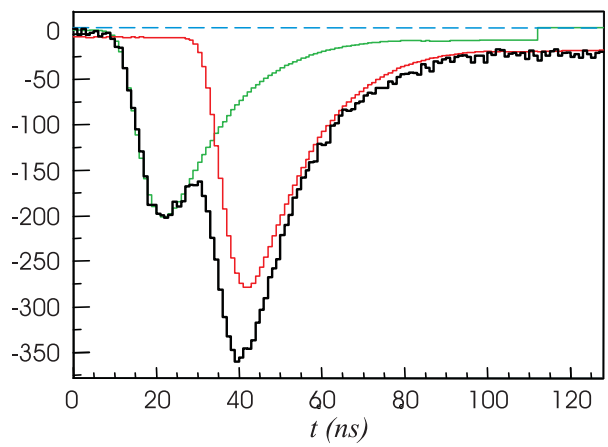

Figure 3.13: Typical pile-up events

this high energy pile-up were made to estimate the occupancy of the detectors depending on the angle this can be seen in figure 3.17. On the other hand the most damaging for the detector comes from low energy particles : Moeller electrons and low energy photons. All of these low energy particles have rates of the order

of several megahertz which are piling-up. The light they produce is equivalent to a continuous component of light similar to a light leak. This constitutes the main problem since this light produces a DC current which is directly proportional to the gain of the PMT. This has two effects :

- It can change the gain since it can induce a voltage drop on the voltage divider which powers the PMT. A study of the variation of the gain with the DC current showed that this was not a problem for DC current lower than 1100 μA the gain variation was less than 4 %.
- Most importantly the lifetime of the PMT is directly related to the charge (which is about 10 Coulombs) drawn from the last dynode. So the DC current has to be monitored and limited in order to ensure the lifetime of the PMT for the whole duration of the experiment.

Simulations

Different simulations were made to study the background. It used a DVCS event generator (L. Mossé DVCS library) associated with Geant to model the DVCS geometry for the different devices of the experiment :

- LH2 target
- scattering chamber
- calorimeter
- proton array

Only electromagnetic processes were included. Another one was made by P. Degtiarenko to evaluate the background distribution in the Hall A configuration

Kinematic	Angle DVCS	Closest angle proton in degrees	closest angle calo in degrees
1	22.29	16	13.75
2	18.25	16.5	9.7
3	14.80	15	6.26

calorimeter simulation In order to estimate the expected counting rates a more thorough simulation was carried out using the data from the two previous simulations taking into account the calorimeter trigger. This allowed to evaluate the behavior of the DC component coming from low energy particles as well as the higher energy pile-up. Background was modeled with the following processes :

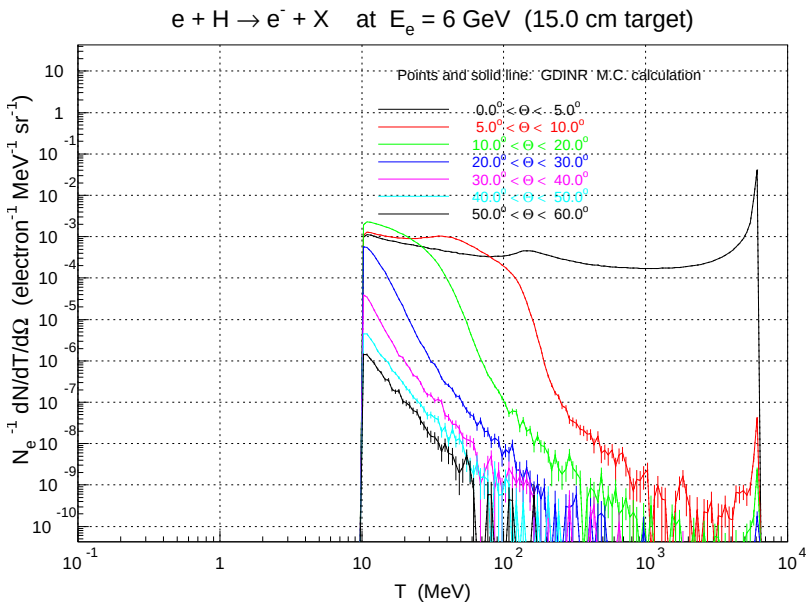

Figure 3.14: Rate dependence versus angle

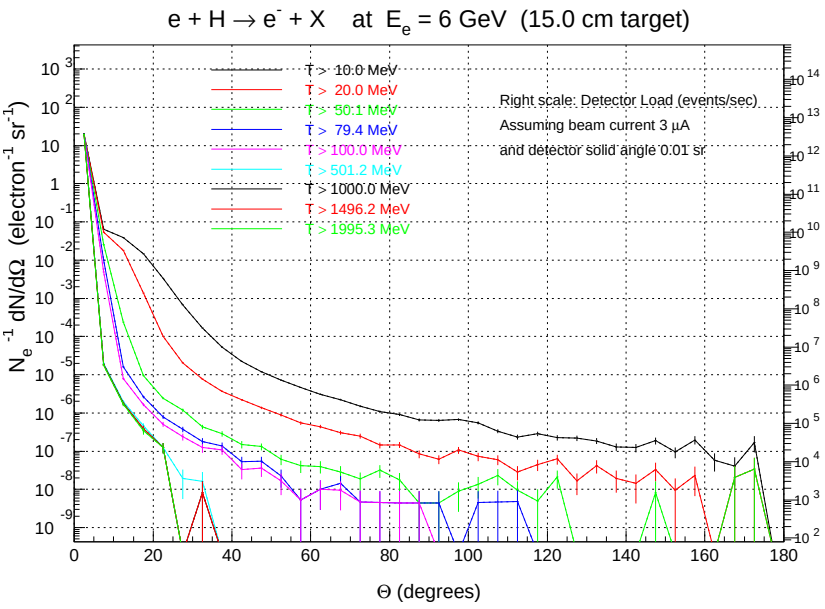

Figure 3.15: Rate dependence versus angle

- Electromagnetic with energy ranging from 0.001 to 0.1 GeV
- Hadronic component ranging from 0.1 to 2.0 GeV
- Deep inelastic component going from 0.1 to 5.75 GeV

kinematic chosen was the one for $Q^2 = 2.32 GeV^2$.

To generate the DC background component, a time window of 10 μs was taken and for each nanosecond of this window an energy deposit was generated from the process previously mentioned. Using a reference shape taken from a previous test run, calibrated so that 500 channels amplitude correspond to 1 GeV (the dynamic range of the ARS being 2000 channels for 4 GeV) the energy was converted to pulses which were piled-up in the window as seen Fig. 3.16.

This allowed to simulate the signal seen by the AC coupled electronics the differentiated signal was computed Fig. 3.17.

Trigger was simulated using the events from the DVCS simulation which would give the energy deposited in the calorimeter blocks for DVCS events to which were added the generated background. All the possible tower were computed allowing to determine expected trigger rates and amount of data to be read.

Background distribution from simulation

Block	Simulation	$\frac{RatioBlockn}{Block0}$	DC read out	$\frac{RatioBlockn}{Block0}$	$\frac{Simulation}{measured}$
0	4	1	0.009	1	reference
90	30	7.5	0.077	8.5	14.1%
114	180	45	0.302	33.5	25.4%
126	220	55	0.409	45	17.3%

3.4 Experimental background distribution

3.4.1 March 2002 test run

The DVCS experiment was conditionally approved in 2000. In order to be fully approved we had to to demonstrate the feasibility to operate the proton array in the background condition. Indeed no scintillator detectors were ever used so close from the target before. We had 3 days dedicated taken right after the end of data taking of the RCS in march 2002 experiment for this test run in order to determine the single counting rates expected in the proton array detector. The scattering chamber was slightly modified with a larger beam pipe in order to reduce background so as to be closer from the DVCS running conditions.

3.4.2 Rate determination

The algorithm to determine the rates was to use the ARS with a random trigger to determine the accidental rates in the proton array. This was done by counting the number of pulses into the window by setting different software energy thresholds and dividing by the time window width. In order to have a good statistic precision the mean value of the number of pulses in the window is computed over the run duration each run was about 500 000 events. Since the windows is 128 ns wide, the rate is simply :

$$Rate = \frac{N_{pulses} \cdot N_{events}}{128 \cdot 10^{-9} \cdot N_{events}}$$

Background and rates

We were able to determine the single counting rates and the effect of different kind of shielding. First conclusion we could draw was the importance of the DC background. When we turned the detectors on no signal could be seen this was our first encounter with the problem mentioned in 3.3.5. So we had to lower the high voltage on the tubes and the beam current in order to be able to take data. The following data were recorded at 0.5 μA with lower high voltage than the ones specified by the manufacturer. The results were scaled to the experiment designed luminosity and are corrected by the PMT gain.

Figure 3.18 show the rates with half inch of aluminum shielding and half inch of Lucite. The block 4 had an additional half inch of aluminum shielding in front of it. The block at 22 degrees is having higher counting rates be cause it was less shielded than block 4 and it seemed that it was more sensitive to the background. We can account this higher rates to the change in gain of the PMT, as measured with the Hamamatsu tube 5.4. The gain tends to increase a little because of the change of balance of voltages in the divider before dropping.

For the next data set we added an additional half inch of Lucite Fig. 3.19.

All the PMTs worked with this shielding and as expected showed lower single rates but with the price to a higher momentum threshold. The plots show than with this kind of shielding only protons with momentum larger than 420 MeV/c would be detected,

Conclusions of this first test run

This test run allowed us to learn the difficulties coming from the background. It was also an opportunity to commission our sampling system providing a new way to determine single counting rates. The conclusions we draw from it were :

- the DC component from the low energy background is a major problem. PMTs need to run at a lower gain

- shielding is compulsory in order to be able to operate the detectors
- enlarging the beam pipe reduced a sizable part of the background
- the counting rates are compatible with the previous simulation which results are in the plots 3.14 and 3.15. So the assumption that the background is electromagnetic and the model of the simulation are validated

3.4.3 Accidental studies in DVCS data

The same study could also be done for the calorimeter. The following plot represents the single counting rates in the calorimeter. It was done using the waveform analysis on the DVCS data of the third kinematic. Since the data were recorded with the ARS and the trigger gate is 85 ns wide, we record for each events 128 ns of signal allowing to look for accidentals outside of the coincidence peak. So following plots were made using the data but looking around the coincidence peak $-11ns < t < -5ns$. This allows to determine how many accidental pulses will pile-up with the real signal.

We can see the energy distribution of the background. It goes from 20 MeV up to a couple of GeV Fig. 3.20.

The background distribution follows the angular distribution with the beam. We can see two different contributions, one with low and middle energy Fig. 3.23 and one with high energy (above 1 GeV) Fig. 3.22

The high energy background comes mostly from elastic electrons reaching the calorimeter.

They account to 1.6 MHz in the block with the highest counting rate. The lower energy background accounts for the remaining counting rates, it comes mostly from decay of π_0 and Moeller electrons.

We can conclude that for the half calorimeter closer for the beam background rates are ranging from 1 to 5 MHz Fig. 3.21. Since pulse width for the calorimeter is 20 ns and with the singles spectrometer rates. We can compare the experimental values obtained with the simulation from the proposal. The rates for the calorimeter given for a 500 MeV threshold are in agreement with the simulation at a 30% level.

Kin #	Calo Sim	Calo Exp
3	$2.2 \cdot 10^7$	$3.4 \cdot 10^7$

We can see that for the rows closest to the the beam accidentals are of the megahertz level for medium to low energy. Given the pulse width of 20 ns, we can consider that pile-up will occur in a 40 ns window so the accidental rate for the calorimeter is for the worst block:

$$N_{acc} = 40 \cdot 10^{-9} * 4.6 \cdot 10^6 = 18.4\%$$

for blocks with rates over the megahertz level 4% to 18% of the events have one pile-up event.

3.4.4 Designs for handling the background

The results of the previous drove the design of different parts of the experimental setup.

Scattering chamber and shielding design

In order to reduce low energy background a couple of options are available :

- reducing secondary source of background
- use of shielding

So the strategy for this experiment was to reduce production of secondary particles. The new scattering chamber was designed keeping this in mind :

- by enlarging the beam pipe exit from standard 2 inch to 6 inches the production of secondary particles downstream the target is reduced. We can see that the angle where matter can interact increases from 5 degrees to 14 degrees. By looking at the figure 3.24 we see that it reduces greatly the number of electrons that can interact with the beam pipe. Indeed electron counting rates in the shaded part are all above the gigahertz level.
- the scattering chamber was designed spherical with a 1 cm aluminum thickness allowing to protons to see the same length of matter while also acting as shielding. And additional two centimeters aluminum plate was added in front of the calorimeter since high energy photons will be detected shielding of the calorimeter is easier than for the proton array.

PMT design and monitoring

Calorimeter In order to reduce the DC current drawn we went from the initial design of 10 stages PMT to 8 stages PMT Hamamatsu R7700 these PMT have a gain of 10^4. In order to reduce the DC component the associated base had a built-in amplifier of a factor 8. This allowed to run at the PMT at a lower gain reducing the DC component.

Proton array The Proton Array is the most challenging detector. Since it is a scintillator it is more sensitive to low energy background of charged particles. The proton which have to be detected have low momentum. The same way as for the calorimeter active bases were used and a diaphragm was placed in front of the PMT to reduce the amount of light collected, its diameter was chosen to correspond to the energy resolution we needed on the proton array.

PMT anode current monitoring Since all the electronics is AC coupled it is not sensitive to the DC current which could mean that the PMT might be drawing a lot of current without being detected and therefore could die prematurely. In order to monitor this the current from the anode was put trough a 10KΩ resistor allowing a read-out of the anode current by recording the voltage on this component. All the DC current coming from the bases were fed into scanning ADCs VMIC3128 giving a real-time read out through EPICS. This was checked and recorded at least once a shift.

3.5 Conclusions

The major difficulty turned out not to be the pile-up which could be handled by the specific electronics but rather the low energy particles generating the DC current. The proton array was the limiting factor for any current increase. We made all our possible to reduce the background sources and to monitor the behavior of the detector. An interesting idea to further reduce the background is the adjunction of a solenoidal magnet similar to the Hall B design which would allow to go to reach luminosity around $10^{38} cm^{-2} s^{-1}$.

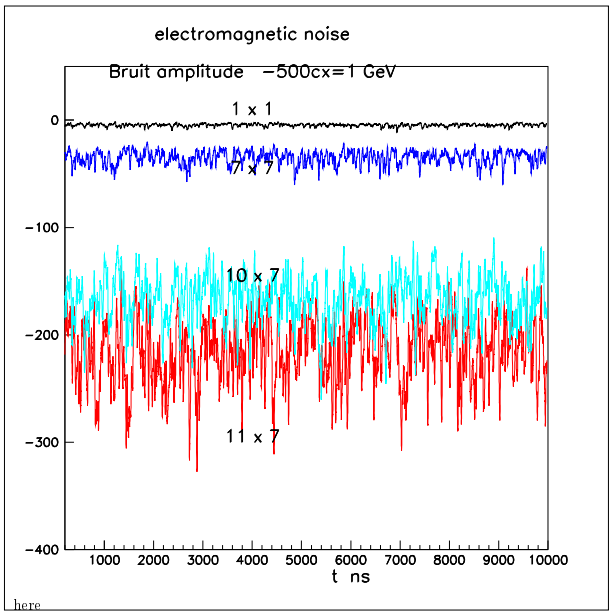

Figure 1: :Electromagnetic noise before continuous level subtraction. Block 1x1 is in the upper left (wieved frok rear . Block 11x7 is the closest to the beam pipe

3

Figure 3.16: Simulated DC current generated by the background

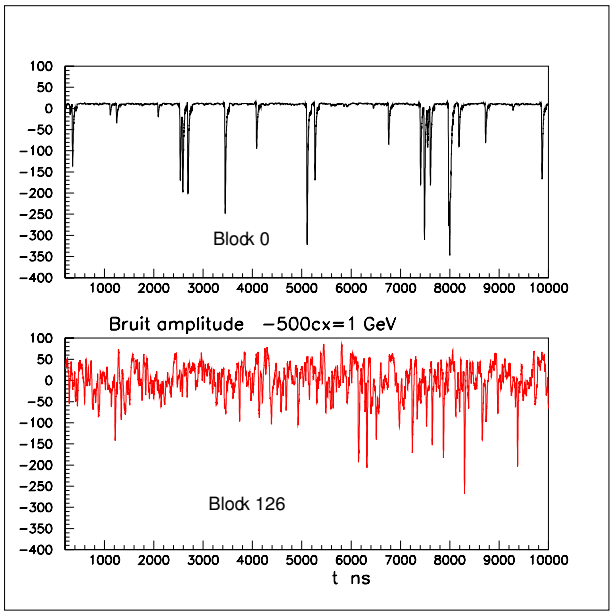

4

Figure 3.17: AC coupled signal as seen by the electronics

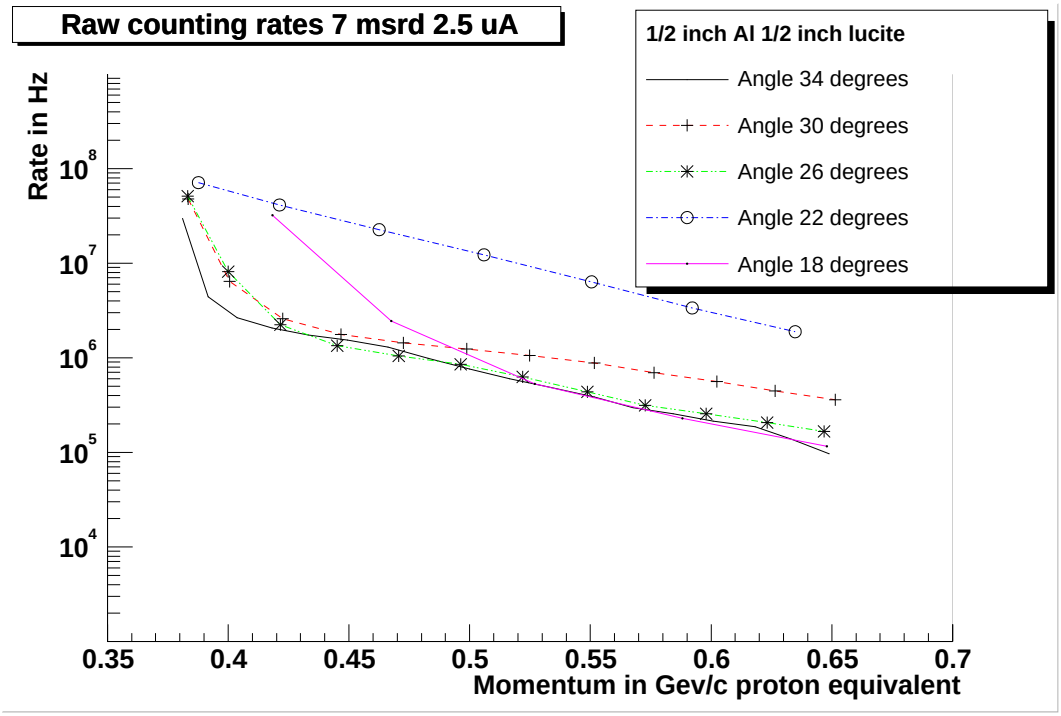

Figure 3.18: Counting rates with 1/2 inch of Aluminum shielding and 1/2 inch of Lucite

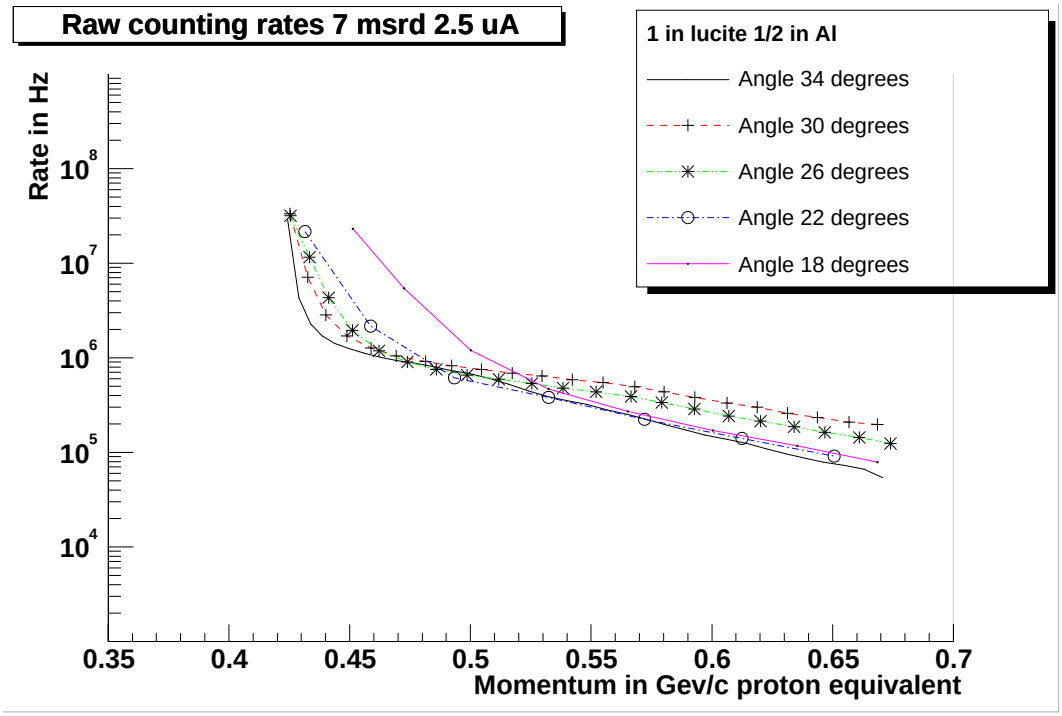

Figure 3.19: Counting rates with 1/2 inch of Aluminum shielding and 1 inch of Lucite

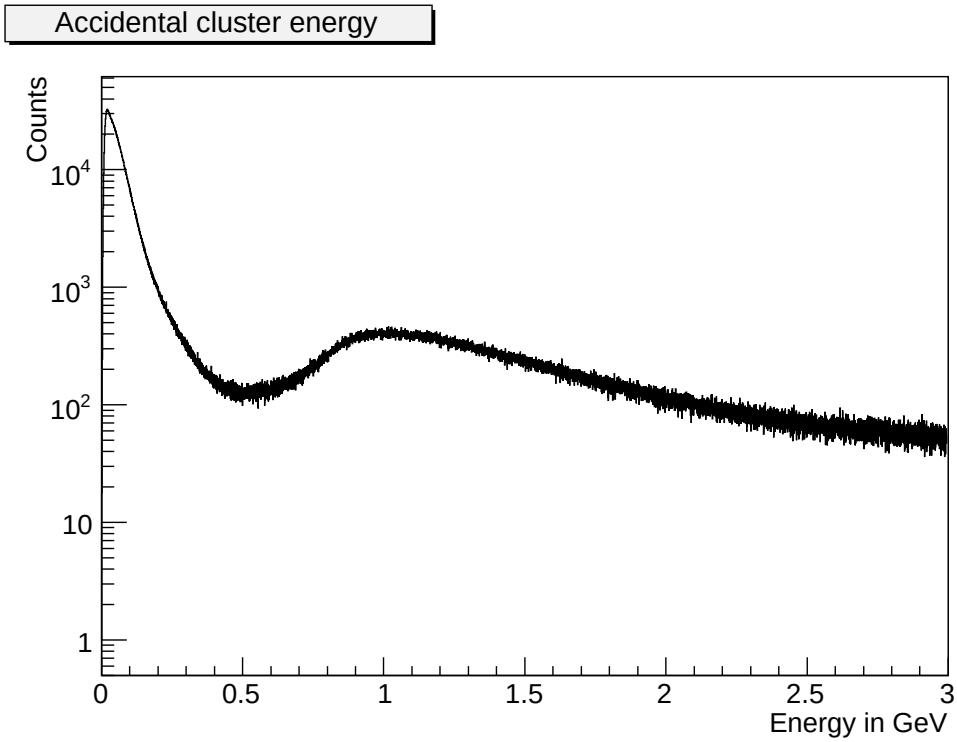

Figure 3.20: Energy distribution of accidentals in the calorimeter

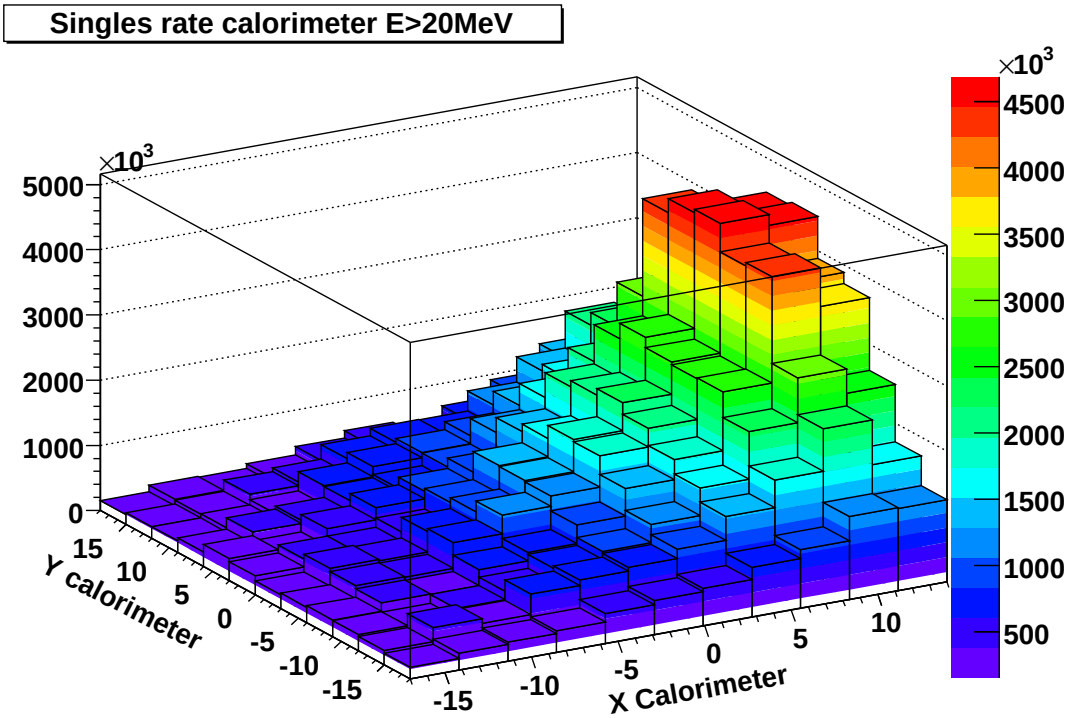

Figure 3.21: Singles accidental rates by block in calorimeter

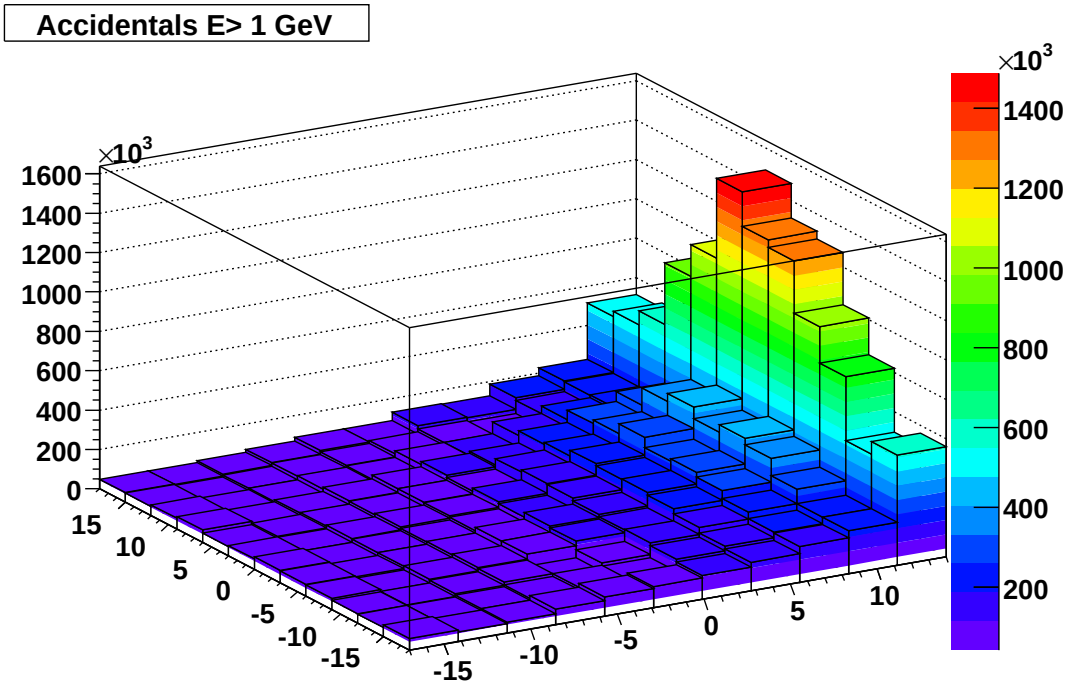

Figure 3.22: Accidentals rates by block of energy higher than 1 GeV

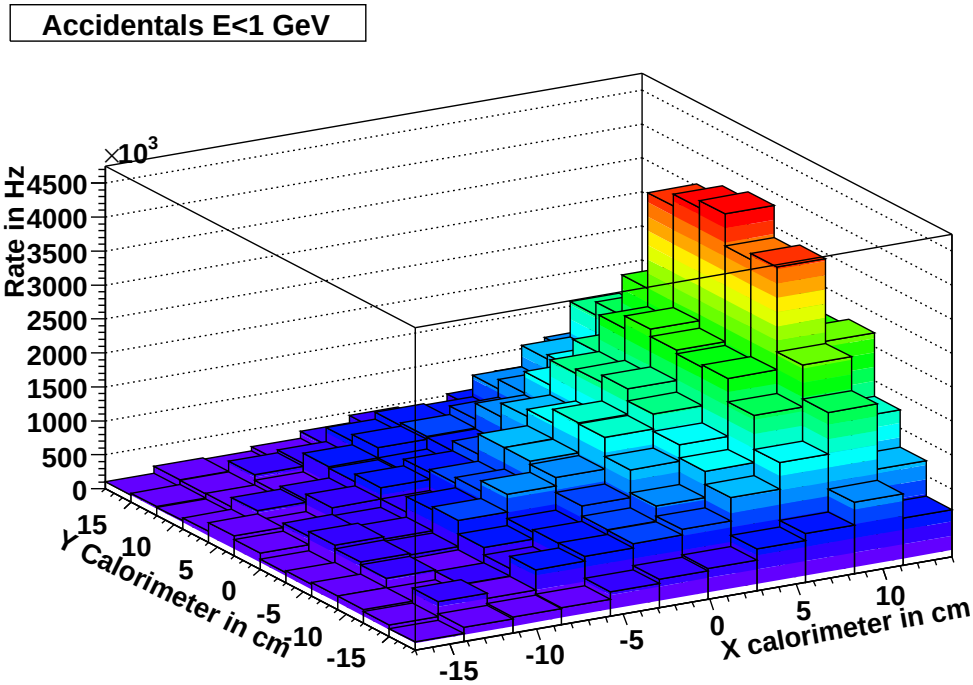

Figure 3.23: Accidental rates by block of energy lower than 1 GeV

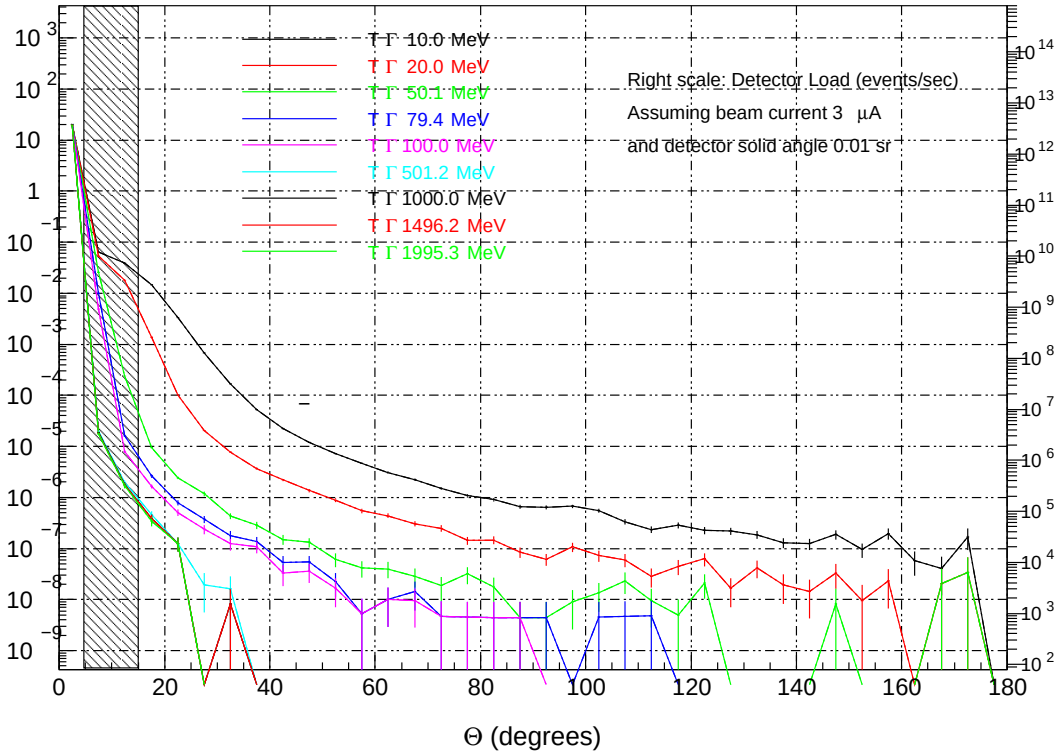

Figure 3.24: Improvement from the beam pipe enlargement

Chapter 4

Electronics and data acquisition

New electronics had to be added since two new detectors were built. I was responsible for all the DVCS related electronics in particularly for the custom electronics built by Clermont-Ferrand. After quick introduction on the principle of data acquisition, I will describe the standard Hall A DAQ. We used a custom electronics in order to address the different needs of the experiment. After using it stand alone during the testing of the detectors in the clean room where the detector was located. We modified the standard Hall A configuration to integrate the DVCS specific electronics. And was used during the experiment during which its performances could be evaluated.

4.1 Data acquisition basics

The Data Acquisition (DAQ) system takes care of recording data coming from the physics detectors. It can be split roughly in two tasks :

- triggering : only events of interest are to be recorded, so a trigger logic has to be designed to select which events will be recorded

- data transfer : information is read out from the modules and recorded. It has to be as fast as possible in order to reduce the dead time (time during which no data can be recorded since the acquisition is busy). Nowadays this task is usually devoted to computers. Modern data acquisition systems may include many electronics boards so it is often split in different crates which are smaller autonomous DAQ system : each crate has a single board computer which reads out the modules and sends the informations to a central computer through the network. This kind of architecture allows parallel processing of the modules and optimization of the data transfer through the use of memory buffers. In our case all these computers are

Power PC computers running the real time operating system VxWorks [81] making the read-out of the modules through the VME bus and sending the data to the network so I will often refer to them as VME CPU.

4.2 Standard Hall A DAQ

The Hall A has been running since May 1997 so all the systems have been commissioned and are commonly used. Since the experiment relies on the Hall A HRS, it is useful to present the layout of the data acquisition system since it will be the starting point for the DVCS experiment : in particularly the DAQ package in use, the trigger setup and the associated electronics.

4.2.1 Jefferson laboratory data acquisition package CODA

DAQ systems vary from one laboratory to the other. At Jefferson Laboratory we used the standard DAQ package called CODA for the physics data analysis Another DAQ package, EPICS, handles the slow controls and will be more detailed in the slow control part 4.4.

CODA software components

CODA stands for Common Jefferson Laboratory Data acquisition. This package of software and hardware components developed by the Jefferson Laboratory DAQ group was designed to accommodate the needs of the three experimental halls. On the software side CODA is in charge of almost all the data transfer part and specifies a data format in which the data are recorded on the disk [44]. CODA software is decomposed in different components which communicate between each other.

- The main CODA process is called RcServer. It holds the different configurations and initializes the components according to the chosen configuration. During data taking it also checks at regular time intervals the status of all the components to ensure that the data are correct.

- The MiniSQL database holds various informations for CODA like the run configurations and the status of all the involved components. Since this is a database server all the components can directly have access to it.

- each VME CPU is running a CODA program called Read Out Controller (ROC) which performs the readout of the VME modules. The only work needed is only to provide CODA ROC with C routines called read-out list

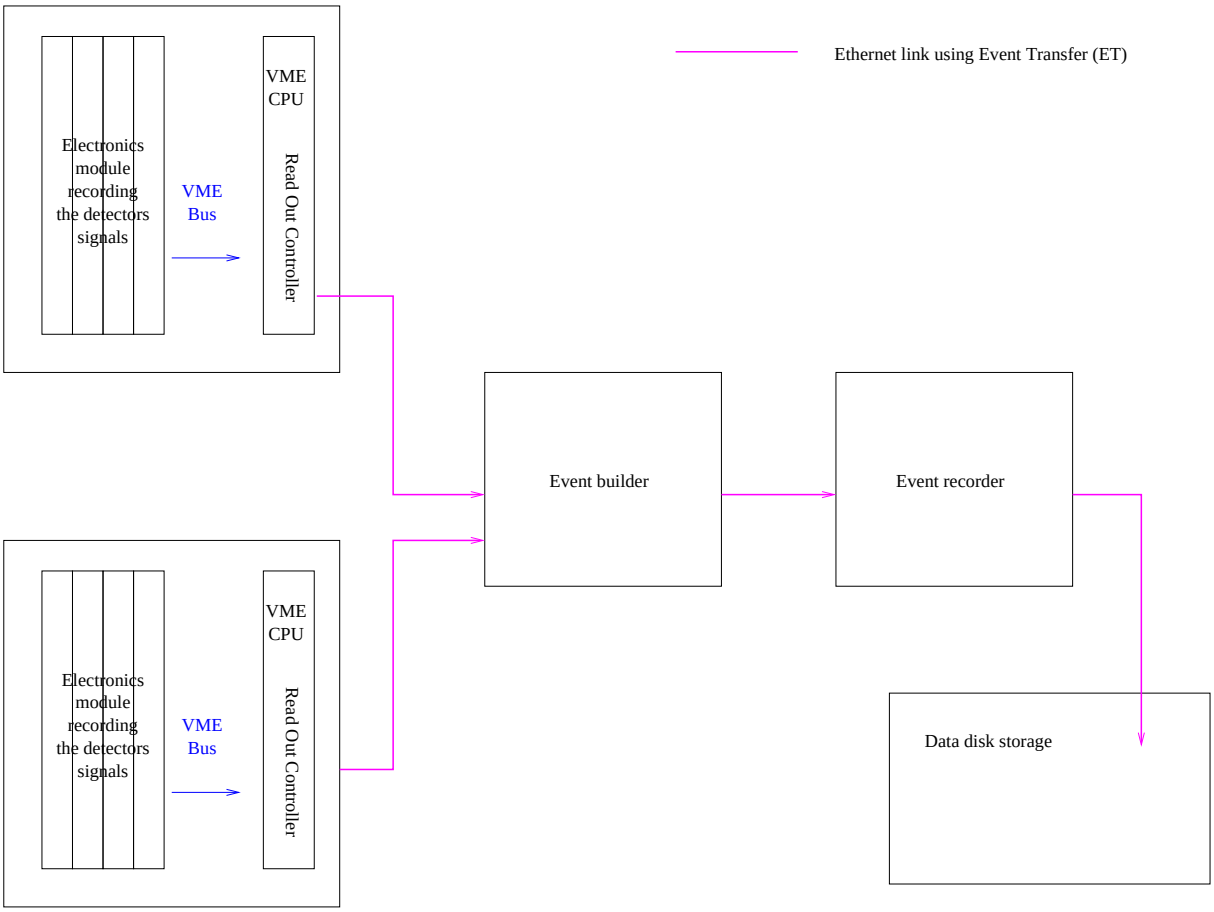

Figure 4.1: Example of CODA configuration

to extract the data from the electronics modules. All ROCs send their data to the Event Builder.

- the Event Builder (EB) collects the data from the different ROCs and sorts them into events putting them into the structured CODA event.
- the Event Recorder (ER) which takes care of the recording of the event constructed by the Event Builder to the attached disk into a CODA file.
- all the components transfer the raw data using the Event Transfer (ET) library

Finally the program CODA RunControl is run on a computer. It is the graphical interface to the rcServer which allows the user to control the DAQ.

CODA hardware components

CODA trigger interface TI

On the hardware side CODA provides electronics helping to manage triggers and event synchronization. Each VME crate running a ROC has a VME CODA Trigger Interface [55] which tells the ROC when to do the readout. Depending on the complexity of the DAQ the ER and EB processes can be run on different computers but in our case all of these programs were running on a Linux computer in the Hall A counting house. The event synchronization between ROCs computer is ensured by the Trigger Supervisor (TS) which is a special type of ROC associated with an hardware board.

Trigger supervisor

The TS [54] hardware is a 9U multifunction VME board. From the several ECL inputs available in the front face, 8 inputs receive the external triggers usually numbered T1 to T8. Signals on these inputs actually start the acquisition of an event. The status of the ROCs are exchanged directly with TS using a dedicated RS432 serial flat cable daisy-chained to all the CODA interface boards which allow to monitor when all ROCs are done processing data. During this time it inhibits all its triggers. This ensures the synchronization between the ROCs.

4.2.2 CODA implementation of the Left spectrometer DAQ

4.2.3 Trigger setup

Spectrometer single arm triggers T1 T3

The spectrometer trigger is generated when a particle go through it. It is generated by a coincidence between two scintillator planes: S1 and S2m. Since S1 is made of 6 scintillator paddles and S2m of 16 paddles the signals go through logic modules [66] : the S1 signal is an OR of the 6 scintillators and the one for S2m is an OR of each its 16 paddles signal. Since there is a PMT (photomultiplier) at each end of a scintillator paddle a coincidence is made between these two PMTs. Nevertheless in order to always have the same time reference the coincidence is set so that the right PMTs from S2 are taken to define the timing. The logic signal issued is called T3 and constitutes the single arm spectrometer trigger for the left arm and T1 the right arm single arm trigger.

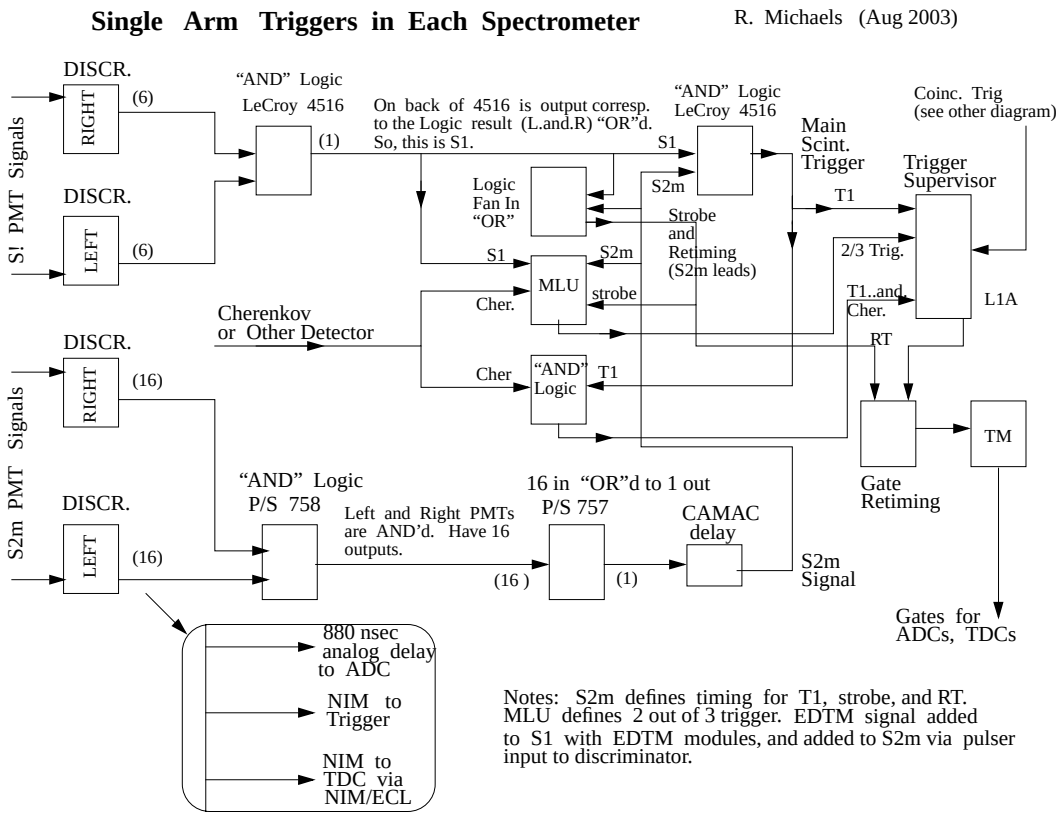

Figure 4.2: Single arm trigger

Spectrometer efficiency triggers T2 T4

Usually an additional trigger is defined for each arm to determine the detector efficiencies. This trigger is called called T2 for the right arm or T4 for the left arm is used for efficiency determination : it is based on taking 2 out of the 3 detectors

S1, S2 and Cerenkov excluding S1S2 coincidence. Since for this experiment the right arm only had the scintillators only not T2 was defined for it.

4.2.4 CODA configuration of the spectrometer read-out

The Hall A using having two spectrometers, both have their own dedicated trigger and electronics allowing them to run either in single or in coincidence trigger. The standard Hall A CODA components are :

- Left spectrometer HRS trigger supervisor TS1
- Left spectrometer HRS ADC TDC Fastbus ROC3 ROC4
- Right spectrometer HRS trigger supervisor TS0
- Right spectrometer HRS ADC TDC Fastbus ROC1 ROC2

Standard electronics is associated with the detectors from the spectrometer detector stack as mentioned in part 3.2.3 :

- ADC fastbus Lecroy 1881
- TDC fastbus Lecroy 1877
- TDC fastbus Lecroy 1875A (at 100 ps resolution for S1 and at 50 ps for S2m)
- VME Scalers SIS 3800

The ADCs record the integrated charge of the pulse coming out from the detectors. Those signals are useful for the Particle IDentification (PID) for detectors such as the Gas Cerenkov detector or the pion rejector. The TDCs give time between the trigger signal and the signal of a detector, those can be used to determine the time of flight of a particle and especially for the VDC to determine the drift time allowing to reconstruct the track with an additional accuracy. For the VDC the TDC are Lecroy 1877 used in common stop which have a typical resolution of 500 ps. High resolution TDC Lecroy 1875A are used for the scintillator paddles, these TDCs only work in common start and were set to 50 ps per channel for S2m signal and 100 ps per channel. Scalers are used to count any value of interests such as numbers of triggers, delivered charge... They are interesting since they continue to count even when the DAQ is busy. So those are useful for efficiencies determinations, charge measurement 6.4.2. The scalers are recorded in two different ways, every 50 events and asynchronously recorded every second.

4.3 Experiment specific electronics and CODA setup

4.3.1 Experiment requirements

The major problem for the DVCS experiment being the background, the electronics developed for the DVCS was specially designed to to deal with it. First by the use of a sampling electronics allowing to resolve pile-up events. In order to reduce the amount of data and improve the signal over background ratio, we also defined a coincidence trigger of the spectrometer with the calorimeter : a special trigger module was designed to generated the photon calorimeter trigger. Different kinds of data were needed to be taken :

- DVCS
- nDVCS
- $eN\pi^+$
- elastic
- LED
- cosmics
- efficiency runs (two single arm)

so different CODA configurations were made including the required detectors. We modified the standard Hall A DAQ to include the new detectors. In particularly we set up the coincidence trigger between the Left Spectrometer and the calorimeter to replace the standard T5 coincidence trigger (usually defined as coincidence between the two spectrometers) and added the sampling system to the CODA read out.

4.3.2 DVCS trigger logic

The DVCS trigger is based on the Left Arm single trigger to which a coincidence with the calorimeter is added.

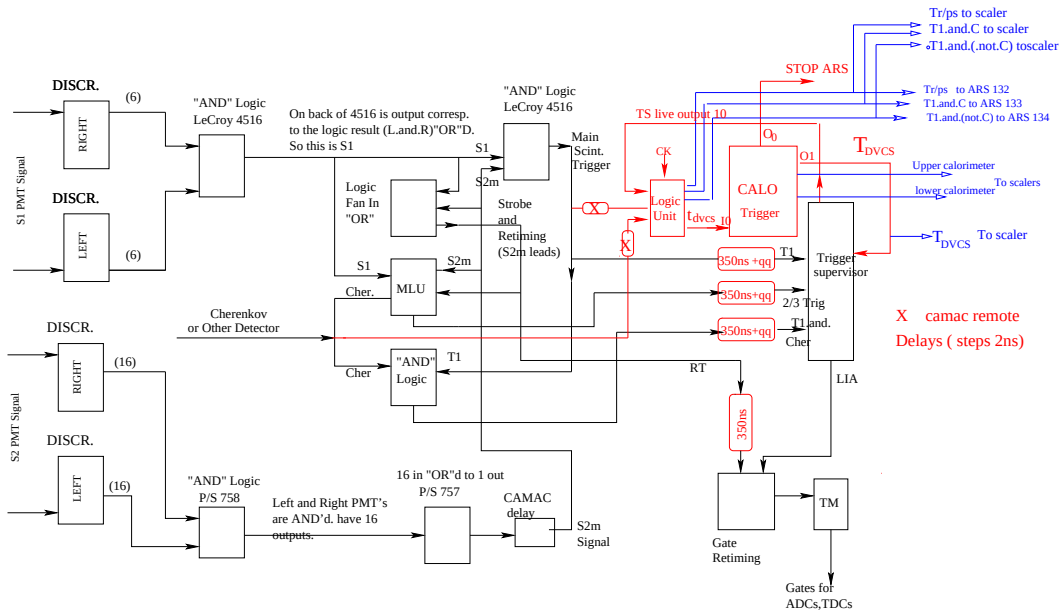

Figure 4.3: DVCS trigger summary

The calorimeter trigger is the second level trigger for the experiment. To determine if a photon has hit the calorimeter when it has received an electron trigger from the spectrometer, a threshold is put on a sum over a given number of adjacent blocks : this allows to take into account most of the blocks participating to the shower giving a good estimate of its energy to be compared with the threshold. This module allowed to greatly reduce the number of analog module usually used to make a calorimeter trigger by summing the channels participating to the shower digitally. So the process to generate a photon trigger is made in two steps :

- first all the channels of the calorimeter are encoded using Flash ADC when an external trigger is issued.
- then when all the data is available digitally, the values are pedestal subtracted and in our case all the sums of 4 adjacent blocks are computed. The photon trigger is generated is one of this sum is over threshold.

Fast ADC The device features a 7 bit Flash ADC for each one of the 168 channels available on the module. To have a good density of channels for the trigger module a custom crate was used. It consists of a motherboard where the FPGA for the sums and the logic were located which received at total 42

4-channels daughter boards which had the fast ADC part. The gate width of the ADC could be set with a register and the values were checked with an oscilloscope and a pulse generator.

Trigger setting	Gate width
0	45
1	65
2	86
3	106
4	126
5	146
6	165
7	186

We choose to run with the setting 3 during the whole experiment corresponding to an 86 ns gate.

A simulation of the impact of the trigger gate jitter was carried out using a simulated DVCS event for different thresholds.

Thresholds	0.5	1	1.5	2	2.25	2.5
window size						
30	100	99.86	99.66	94.83	79.60	33.04
40	100	99.96	99.96	99.96	99.93	98.74
50	100	99.96	99.96	99.96	99.93	98.38
60	100	99.96	99.96	99.96	96.96	99.49

Tower construction and channel numbering Once all the signal are digitized the FPGAs make a pedestal subtraction and compute all the sum of 4 adjacent blocks on 8 bits. The use of FPGAs allowing parallel processing of the data. The trigger making the sums of adjacent channels implies to plug the corresponding block to the right trigger channel : the numbering scheme is often referred as "trigger numbering". An example of how the trigger is numbered and how sums are computed on Fig. 4.4, this represent the numbering looking the calorimeter from the back (channel 0 are farther from the beam and channel 120 closer).

The whole cycle to generate a photon trigger takes 400 ns.

If one of this sum is over a set threshold a validation signal will be issued if none is above threshold the trigger clears itself after 500ns.

Logic module and trigger logic

A logic module was initially designed to be associated with the calorimeter trigger in order to relieve some logic functionalities from the trigger FPGA which were

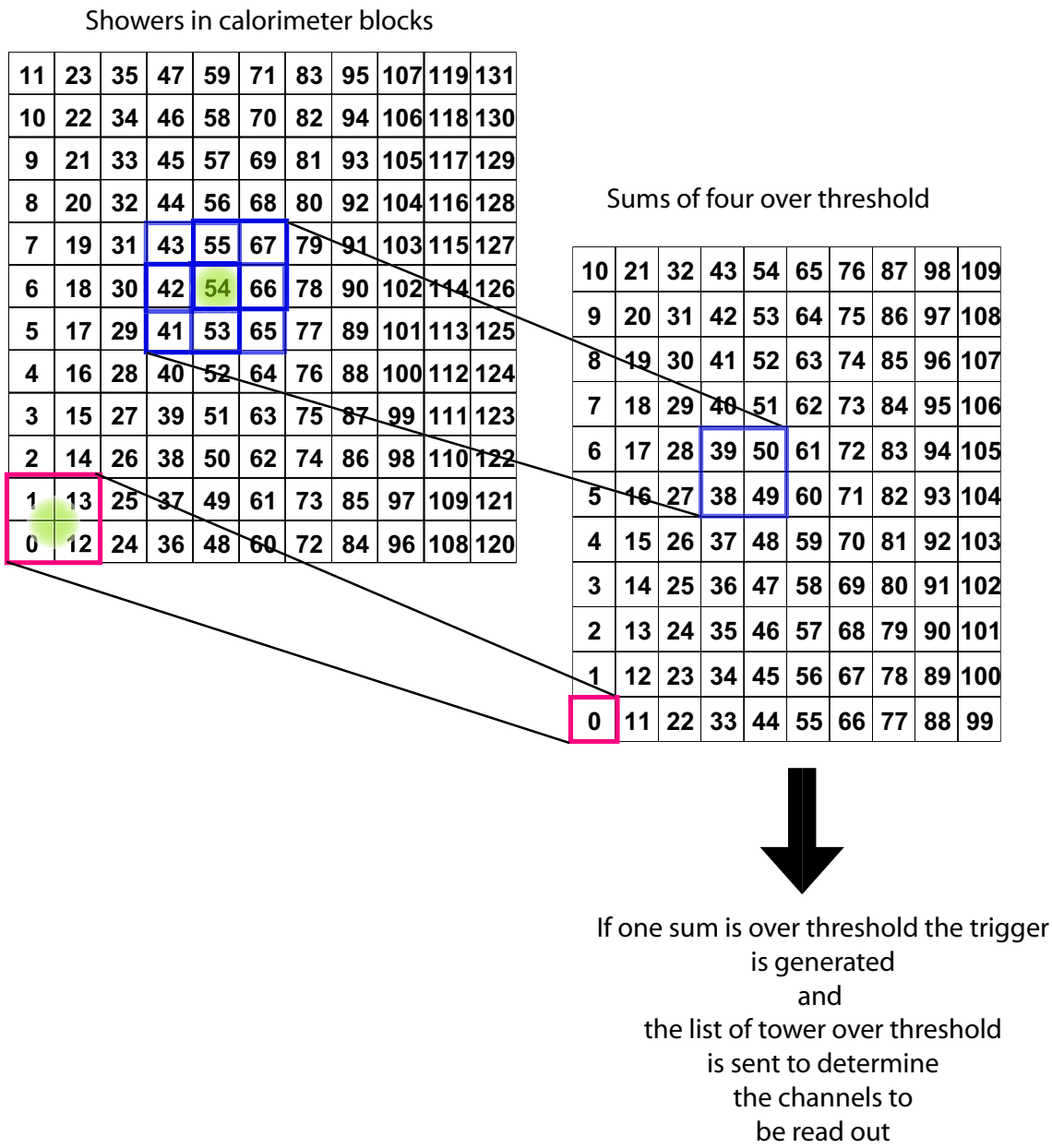

Figure 4.4: DVCS validation

already filled up by the trigger functionalities. Additional features could be added thanks to the FPGA flexibility so it eventually played a major role in the trigger logic since it could integrate a complex logic for the trigger all in a single VME board which was very convenient due to room constraints which was limiting the use of more than one NIM crate for logic. In order to generate the trigger signal which will be used as input to the trigger supervisor, the module takes as inputs logic signals from :

- S2
- Cerenkov
- DAQ enable
- DAQ busy
- calorimeter trigger busy
- T3 trigger

this allowed the logic module to take care of many functions needed for the trigger :

- inhibition
- generate the DVCS trigger from the spectrometer signals and the calorimeter signals
- tagging and selection of the Cerenkov (electrons) and non Cerenkov (pions) events.
- dead-time measurement
- control of the multiplexer

The coincidence trigger T5 starts the encoding of the modules and the data transfer, if this signal is not issued the electronics make a fast clear. This signal is a coincidence between the calorimeter signal which constitutes a S2mγ coincidence and T3 giving a cleaner electron signal. Additionally the gas Cerenkov detector could be added to have control on the pions events by being able to set a prescale on the non Cerenkov event, a prescale factor could be set if some pions events were needed such as the enπ^+ run where all the pions events had to be recorded. This came to modify the Left single arm trigger in the following way 4.5

All the logic signals for the calorimeter trigger and the ARS are going through the logic module. This allows to inhibit the gate of the trigger module and the

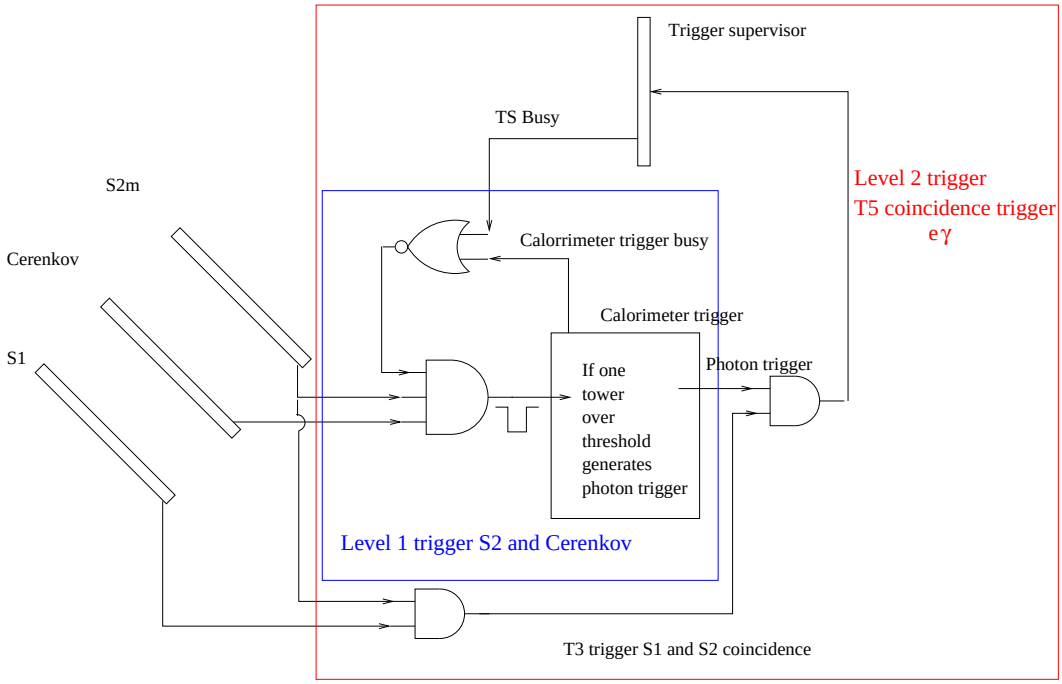

Figure 4.5: elements added for the DVCS coincidence trigger

ARS when an event is being processed. The fastest signal issued by the module is the ARS stop, which is a AND of the S2m signal with the gas Cerenkov for the DVCS data taking. The validation signal which will be used as T5 which starts the DAQ and the encoding of the ARS happens later since it is a AND of the calorimeter photon trigger (which takes 400 ns to be generated) in coincidence with T3 (coincidence of the two scintillator planes).

Timing

Trigger timing setup

Timing has to be made so that the analog signal is in time with the gate generated by the trigger in order to be recorded. Timing was made using different scintillator paddles associated with cable length so that these detectors were in time to 1 to 2 ns at a given high voltage. We used these paddles as cosmics data taking trigger. These paddles were later used as fixed time reference. Delays on calorimeter

PMT transit time		9ns
PMT to patch panel	7m	35 ns
RG213	55m	275 ns
Patch to trigger	4m	20 ns
Total	66 m	339 ns

Spectrometer timing setup

The spectrometer has a 880ns analog delay line on the spectrometer analog signals allowing some freedom on the time taken to generate the trigger. The coincidence trigger induced a delay of 438 ns coming from the time taken by the trigger to generate the trigger and the cabling so we reduce the delay on the gate by this value to have the spectrometer ADC gate in time with the coincidence trigger. In order to have the coincidence trigger in priority the regular spectrometer triggers were also delayed so that they have the same delay as the coincidence trigger.

Trigger gate setup

The signal from S2m used to start the calorimeter trigger was arriving 95 ns after the calorimeter analog signal. Since optical length of the spectrometer is 24 m and electrons are highly relativist in the trigger time of flight of the electron is 80 ns, this left 15 ns of gap between the start of the gate and the calorimeter trigger analog signal which fit in the trigger gate. This values includes the jitter induced by the digital timing, since all the delays are an integer number of the clock period (in this case we have a 50 MHz clock) and the start of the gate arrives asynchronously with the clock giving an uncertainty of 1 clock cycle on the gate width. For the experiment we set the threshold to 57 which corresponded to about 900 MeV for a tower. So efficiency due to the trigger threshold is not an issue for the DVCS event where the photon energy is above 2 GeV. The trigger gate was chosen quite large at 86 ns.

The timing spectrum of the calorimeter show that the coincidence signal is in the ARS window at 30 ns. One can distinguish the trigger window by looking at the distribution of the accidentals. To make sure the coincidence peak was centered in the trigger window the run 2809 was taken with S2 signal delayed by 10 ns. The trigger yield was the same even after the delay which confirms that the coincidence peak is not at the edge of the trigger gate Fig. 4.6.

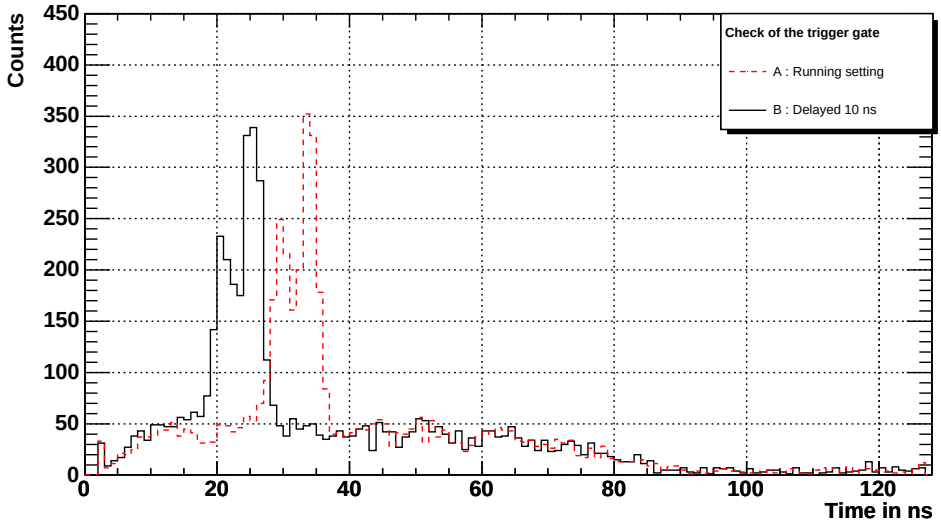

Figure 4.6: Coincidence peak taken from run 2807(B) and 2809 (A) generated with the ARS, trigger signal coming from S2m was delayed by 10 ns, the run was taken in the configuration for pions : $\pi+$ were taken in the left spectrometer and electrons in the calorimeter

4.3.3 DVCS data readout

Two new VME crates were added to the standard Hall A DAQ in order to read the calorimeter and the proton array in parallel.

- DVCS Calorimeter ROC17
- DVCS Proton array and proton tagger ROC18

the electronics for these two crates are similar both had a trigger module and set of ARS board and a logic module. Their use was not symmetrical though since only the calorimeter crate was in the trigger while the proton array crate was only read out. These ROCs gathered the data from the specific modules.

Logic module data

Scalers for dead time measurement Scalers were added into the logic module. They are designed to record the counts from a 16 ns clock in order to determine the dead time. The scalers were coded on 48 bits. The clock counts were enabled by different input signals and were recorded by a scaler. The main scaler labeled 0 is recording all the clock counts. The scaler labeled 1 is the clock gated by the trigger busy. The scaler labeled 2 is the clock gated by the DAQ

busy. The scaler labeled 3 is the clock gated by the DAQ busy or the calorimeter busy

The data of this scaler is sufficient to determine the time the busy time for the calorimeter trigger and the acquisition. These information allow to determine the charge effectively recorded this will be further explained in the section 6.4.1.

Hit pattern The logic module has several accessible VME registers. Besides the control register, a data register containing a bit pattern allows to determine the type of trigger

Signal	bit	Value
Valid	1	1
Random	2	3
Cerenkov	3	5
Non Cerenkov	4	9

Following is a figure for a deuterium run, showing the repartition between Cerenkov and non-Cerenkov events.

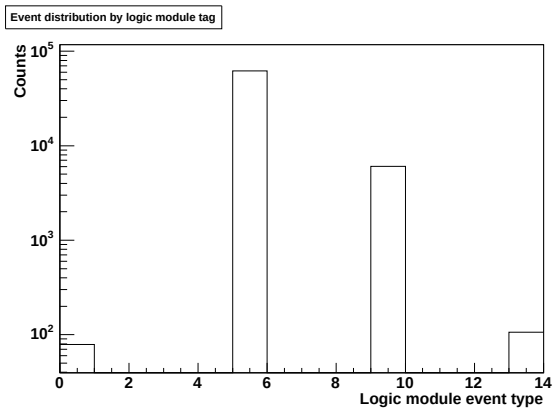

Figure 4.7: Event distribution by logic module type

Event type 0 comes from a clock trigger, so DVCS acquisition has not triggered giving an event type 0. Event type 5 are Cerenkov events. Event type 9 are non Cerenkov event. Event type 13 are non Cerenkov event which happened to occur at the same time as the random clock which was not used.

Calorimeter trigger data

When a validation signal is issued data from the trigger is transfered to the VME CPU allowing to read only the modules corresponding to the blocks hit and also

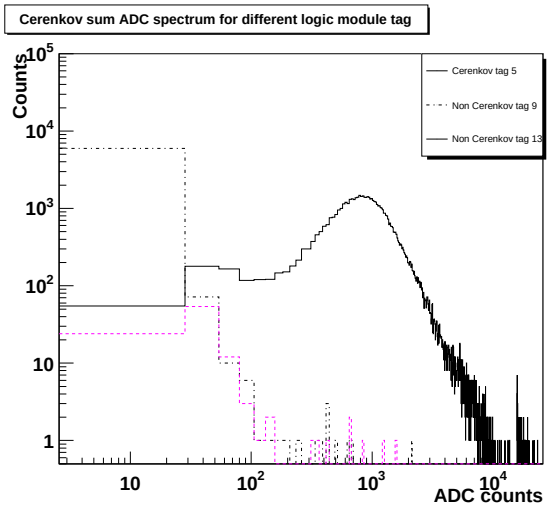

Figure 4.8: ADC spectrum of the Cerenkov sum depending on the type from the logic module

record all the channels with a moderate resolution. At the end of the data transfer the module is cleared and ready to take another event.

Data available on bus The different informations from the trigger are made available on the VME bus :

- tower over first threshold
- tower over second threshold
- sums values
- ADC values of each channel

organized into 92 32 bits words.

Sampling electronics ARS data

ARS principle : analog memory The DVCS electronics recording electronics is a custom 6U 16 VME (A24/D32) module sampling system which is based on the ARS chip developed by Saclay for the ANTARES experiment[61]. This chip allows to sample the input signal of each channel at 1 GHz frequency.

ARS0 chip The ARS chip[31] is a CMOS technology Application Specific Integrated Circuit (ASIC) using the analog memory concept [49] to sample data at a clock rate of 1 GHz. It consists in a circular array of 128 capacitors on which the incoming signal is continuously switched at a clock frequency of 1GHz. After 128 ns the first sample thus gets overwritten allowing the sampling process to be continuous. When a trigger is issued the switching is stopped and the previous 128 nanoseconds are stored on the capacitors. This analog information can be held for up to 500 ns before the discharge of the capacitor alters the data. During this time frame a valid signal can be issued in order to start encoding of the charges or if no valid signal is issued during this time the sampling is restarted. By design each ARS chip hold four channels : when encoding process is started each sample of each channel is multiplexed to an ADC and the encoding of the data is made at a rate of 1MHz. Since the ARS chip only works on positive signal the input of the board are capacitive and a constant DC level is injected on the ARS input.

Operation of the board As soon as it is initialized, in normal operation the ARS continuously samples the signal on the 16 channels. The STOP of the module is issue by a NIM pulse on the input named trigger. This signal stops the ARS and inhibits the trigger input in order that no other trigger can be taken until the event is processed. The timing of the ARS can be set in order to move the time window recorded compared to the STOP signal by varying the ND parameter which ranges from 0 to 107 ns, at 0 the window starts 30 ns before the gate so we can record a 128 ns time window starting from 30 ns after the stop up to 137 ns. When a NIM signal is issued within 500 ns the encoding process is started otherwise the module clears itself. Since the sampling system records 128 times more data than a usual ADC, this stop validation process reduces significantly the dead time of the device by sparing the encoding to only interesting events.

Data structure After the encoding the data is read out from all ARS by the board FPGA (Floating programmable Gate Array equivalent to a processor) formatted in 32 bit words. Each sample is encoded on a 16 bit word :

- 4 bits have the ARS channel number
- the sample amplitude encoded on 12 bit

In order to take advantage of the bus 32 bit width two samples are packed together into a 32 bit word. So the data of one 128 samples of a channel is a stream of 64 32 bits words. The data transfer is made using the VME BUS. It can be done by regular D32 VME cycle or using DMA BLock Transfer 32 (BLT32) to achieve a peak transfer speed of 8 megabytes per second.

ARS specific triggers By design operation of the ARS requires two trigger signals : the stop signal which stops the ARS holding the 128 nanosecond amplitude information on the capacitors and the valid signal which starts the encoding of the samples and the readout. The stop signal defines the timing. It has to be fast enough so that signal coming from the detector can fit in the delay cable.

ARS Stop S2m is an upgraded version of S2 (which was similar to S1) and was designed to have an improved timing resolution and the signal of the right PMTs of S2m is used as time reference for all the electronics. For the DVCS experiment we took the S2m signal right after the logic modules in order to be faster than T3 and used to stop the ARS and start the calorimeter trigger

Validation signal This signal starts the acquisition and the encoding of the data held into the ARS. It is given by the logic module and will be defined later in the logic module paragraph and corresponds to a coincidence spectrometer calorimeter.

ARS and trigger timing Timing is fixed by the cable length but there is a degree of freedom for the ARS since a digital delay can be obtained by varying the ND parameter of the ARS. Another constraint comes from a previous feature for the ARS allowing it to check if the valid signal arrives within a time window after the stop to start the encoding : this window had a maximum value of 384 ns starting at 64 ns after the stop giving a maximum range for the valid of 448 ns. This feature was designed before the calorimeter trigger was built : the calorimeter trigger adds 395 ns so to give room for additional jitters and cable the stop of the ARS were delayed by 45 ns and the settings for the ARS were ND=9 (72 ns). Timing was check with a pulser with a variable delay allowing to scan the trigger gate. It was also checked with a run during the data taking.

ARS Data format mode The ARS were designed following the proposal specifications where this readout was dedicated to the proton array read out. A threshold was supposed to be put on each detector channels. When the decision of the construction of a new calorimeter was made, it was also decided to use the ARS to make its readout. Since a shower is spread among different blocks, one block can have a very small energy deposit making it impossible to use a threshold, so it was decided to base the read-out on the calorimeter trigger information. This would allow to select all and only the blocks participating in the shower as described previously 4.3.2. So a random access channel read-out mode was added to the ARS : the data of each channel could be accessed at addresses which are base address plus a multiple of 0x100 corresponding to the channel. This allows

to read only the channel belonging to the clusters. This mode was also used for the proton array and proton veto detector since the threshold values were hard to determine and efficiency determination could have been a problem.

Calorimeter readout

The calorimeter data is read-out first. It is read-out by the VME CPU which sends it to the network to be recorded and keeps a copy of it in memory. This allows to keep the list of tower hits in order to determine the ARS channels to be read. An array corresponding to the ARS channels is filled up based on the bit pattern of the tower from the trigger. Once the channels to be read are determined a look-up table giving the correspondence between trigger channel and VME address of the ARS channel to be read is used to transfer the data.

Proton array, tagger channel readout :

For the proton array we read out all the blocks during the kinematic 3 since electrons triggers were at a low rate. For the kinematics at higher rate, we decided to reduce the number of block to be read based on the calorimeter information. Since the virtual photon is well defined by the spectrometer, the position of the proton can be deduced from the position of the photon. Using the data from the simulation which introduce resolution effects of the detector we built a look-up table which gives the proton array blocks to be read for a given calorimeter tower [25]. In this case the read-out is made in different steps since the calorimeter information has to be passed to the proton array too. The calorimeter data is first read out by the calorimeter VME CPU. We are using a multiplexer which allows the calorimeter trigger to send its data to the proton array. So then the calorimeter crate is done it makes the calorimeter trigger available to the proton array while it continues transferring ARS data. The VME CPU from the proton array transfers data from the proton array trigger to record all the channels of the proton array and the veto using the ADC information of this trigger. Then it waits for the calorimeter trigger to be available and reads out the calorimeter trigger information. Based on this data the proton array and veto channels to be read are determined using the same scheme as for the calorimeter. This method allowed to reduce the data read from the proton array crate by at least a factor 2 without having to set any threshold on the channels. The average number of blocks read as determined by the simulation was about 20 during the experiment with the background. Experimentally it was about 30 giving a reduction by a factor 3 of the data to be transfered for the proton array.

4.3.4 Dead time and electronics performances

DVCS crates data transfer and dead time

Some measurements of the data transfer speed were made. The CODA trigger interface has logic outputs which can be user defined. In the read-out list program I put a state change in the different parts of the program which was doing the read-out For one trigger channel hit, the total read-out time was 470 μS which could be broken up into :

number of channels readout :	9	132	interpolation 1 channel
trigger data transfer :	105 uS	105uS	105uS
channel to be read determination :	5 uS	5uS	5uS
ARS transfer :	360 uS	4800 uS	40 uS
Total time :	470 uS	4910 uS	150 uS

One can see that dead time comes the ARS data transfer. These measurements allow to have an idea of the dead time for a certain number of channels read.

$$Deadtime(\%) = Rate * (Channels * 40 + 110) * 10^{-6} * 100$$

Since the VME crate are read out in parallel, read out dead time is driven by the proton array crate which had the biggest number of channel to be read. To give an idea in the worst case 50 blocks have to be read and a typical value of the dead-time is 25 % which gives a rate of 118Hz.

This value is slightly higher than the actual rate since the events come randomly, while this computation supposes that they come at a fixed rate.

ARS characteristics

Input characteristics The input for the signal are 50 ohms Lemo connectors. The ARS chip only work on positive signal, a DC current is thus injected and the input are capacitive so the boards only work on pulses. A RC filter integrates the signal in order to improve the timing resolution by fitting on the edge of the pulse.

Resolution, linearity range The range of the constant level affects both the dynamic range and the linearity of the device. The calibration is 1 channel for 0.6 mV and the linearity is good for values of the constant level of 2200 channel giving a range up to 1.3V. A single channel fluctuation is 3 to 4 channels. Channel by channel differences varies with a total dispersion of 30 channels from an ARS to the other as well as sample to sample because of the capacitor discharge : like regular ADC this will be taken care of by subtracting pedestals.

Crosstalk Since each ARS has 4 channels, a 1% crosstalk is present between two channels on the same chip. We designed a cabling scheme for the calorimeter in order to avoid crosstalk of channels into a tower. The algorithm is simple it spreads out the calorimeter channel as much as possible between the 9 ARS board of the calorimeter.

ARS calibration Each ARS sample is encoded on 12 bits, the ARS were used only with half of the full scale in order to stay where the signal stays linear giving a dynamic range of 1.25 Volts on 50 Ohms inputs the calibration constant being 1.6 channels for 1 mV.

Timing resolution The timing resolution on the events depends on the trigger which generates the stop and on the intrinsic electronics resolution. LED runs allowed to determine the timing resolution of the whole chain from the PMT to the ARS for run 3207. Timing resolution is dependent on the analysis, the following plots were made using a constant fraction method. Typical RMS is less than than 1.1 ns Fig.4.9.

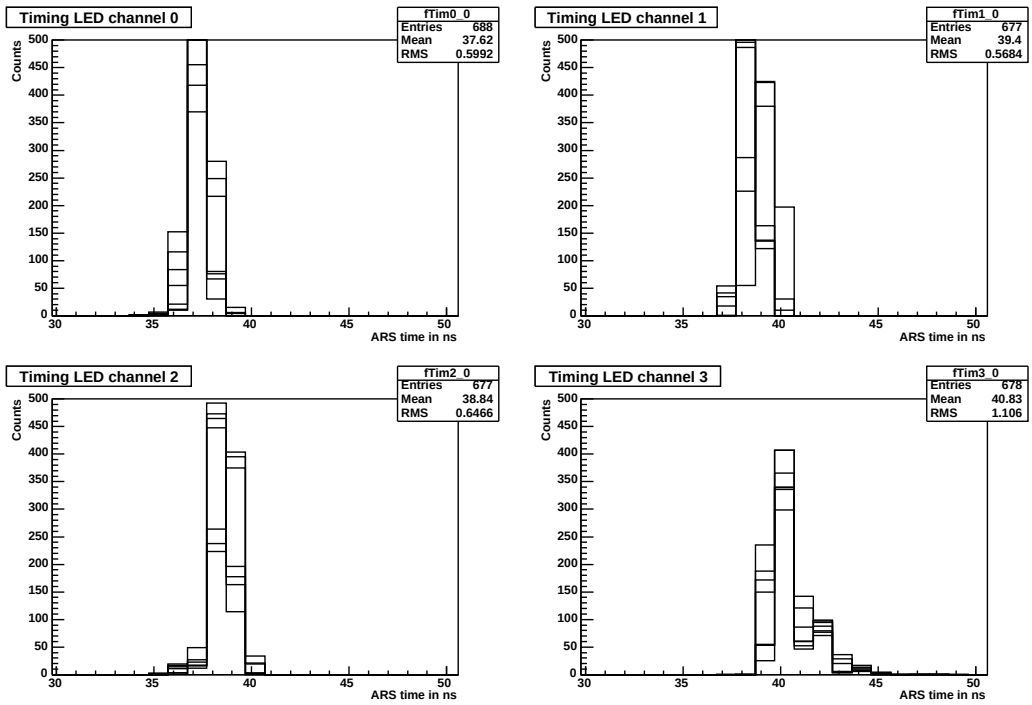

Figure 4.9: Timing of the ARS for LED all 7 LED combinations of 3 LEDs

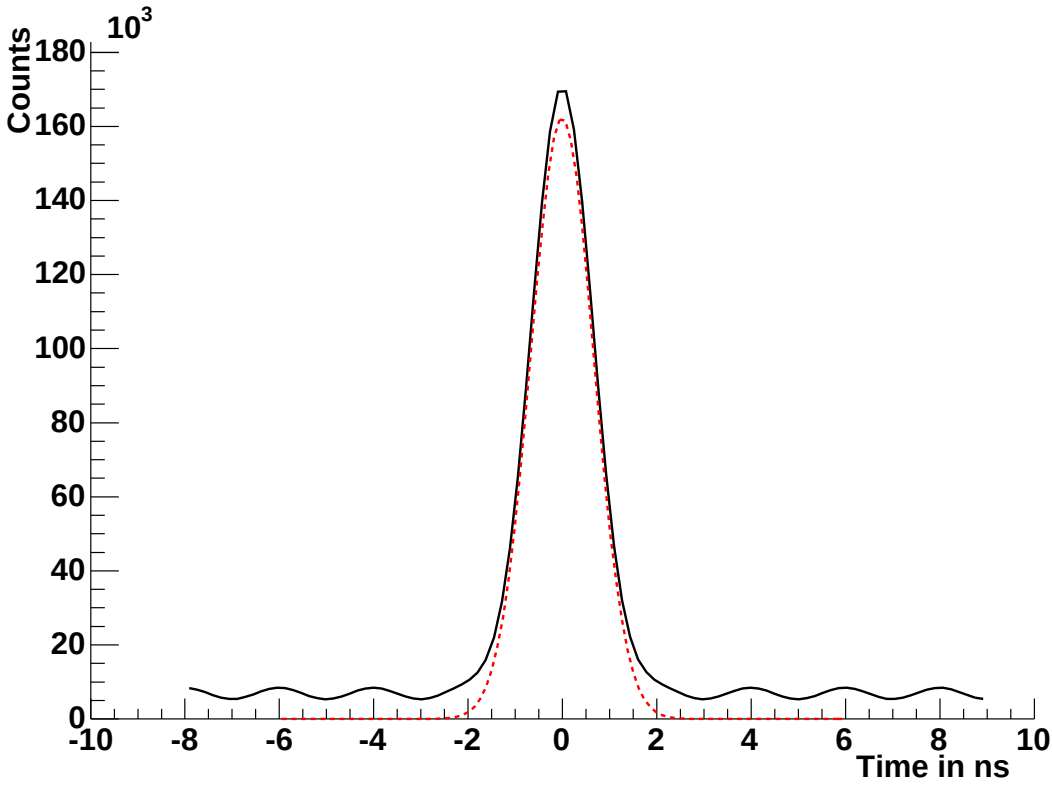

Figure 4.10: Calorimeter left spectrometer corrected time coincidence spectrum for kinematic Q^2=2.32 GeV^2

This can be compared with the waveform analysis from the data Fig. 4.10. Using the corrected coincidence time, we get the resolution for the whole experiment, it is a convolution of the detectors timing resolution with the electronics resolution. The sigma of the distribution is 0.7 ns. So the experimental timing resolution of the ARS with the waveform analysis is better than the sample width of 1 ns one needs to keep in mind that this value is convoluted with the Left Spectrometer detectors timing resolution.

Dead time

Network dead-time The VME CPU used for the DVCS crates were MVME 5100 [70], these boards have 100 MBit network adapter. The network output of

the DVCS crates were plugged into a Gigabit Ethernet switch sending both data from proton array and calorimeter crate to the main Hall A Gigabit Ethernet switch which goes up to counting house. As soon as the crates were on line, raw data transfer rate was tested using a program running on the VME CPU sending as much data as possible to the DAQ computer which receives it.

Crate	Detector	Transfer rate in Mo/s
17	Calorimeter	11.7
18	Proton Array	11.7
TS	Spectrometer	9.6

The dead time associated to the data transfer thus was :

$$DT_{network} = \frac{EventSize}{Transferrate} * rate$$

VME dead-time Event sizes vary for the different kinematics and depending on the use of the multiplexer

Kinematic	Nb Calo	Nb PA	Mux	Coincidence	ARS DT	Net DT	Dead time
I	8	100	0	60	26.5	15	42
II	8	100	0	38	16.8	9.5	27.7
II	8	31	1	50	6.75	4.5	9.4
III	9	100	0	21	9.4	5.32	15.8

This shows the Ethernet interface of the VME CPU contributed to a sizable part of the dead time.

Dedicated scalers for dead time measurement Dead time measurement is usually computed using scalers which count the raw trigger rates coming out from the logic modules. The dead time is thus given by the ratio of recorded events divided by the total trigger number. However by design of the coincidence trigger, no other coincidence trigger can be generated right after a trigger has been accepted preventing the use of this method. Since the logic module was receiving all the busy signals from the calorimeter and the Trigger Supervisor, we had the idea to add scalers channels into this module in order to determine the dead time which was straightforward since this module is FPGA based. Scaler channel 0 counted a 16MHz clock. Channel 1 scaler had the clock signal gated by the busy signal of the calorimeter. Channel 2 had the clock signal gated by the busy signal coming from the Trigger Supervisor. Channel 3 had the clock signal gated by an OR of the busy signal coming from the Trigger Supervisor and the calorimeter giving the total dead time. These scalers allowed to measure the time when the DAQ was busy. Calorimeter dead time when events are not validated can be determined by subtracting value from Channel 3 the value from Channel 2 this dead time was as expected low with a value of about 0.5 %.

This scalers were also read-out on-line to estimate the dead time during the data taking.

Helicity signal and synchronization checks

Since we are looking at helicity dependent cross sections, we recorded the helicity state of the beam. The helicity of the beam is indeed flipped at 30 Hz, the corresponding helicity signal is provided by the accelerator. This signal is fed into the Trigger Supervisor which has user signal inputs allowing to record any logical signal and was put into the data stream event by event. In the same way as helicity information to check event synchronization were recorded, in each crates scalers value from a 105 KHz clock was recorded in each crate as well as different event counters.

4.4 Experiment slow control

Slow control is all the acquisition system that is recorded on time basis rather on an event basis like CODA. It is mostly used to control and monitor electronics elements like High Voltage, power supply... The other data acquisition package used is EPICS (Experimental Physics and Industrial Control System) which is a standard package used for slow control in many different laboratory. EPICS has is based on IOC (Input and output controller) which is equivalent to the CODA ROC : a VME CPU running the EPICS program constitutes an IOC which gather

the data from the electronics in the crate. A IOC communicates with the EPICS server sending and receiving commands and informations to it and relaying them to the associated electronics module.

4.4.1 Standard Hall A slow control

The standard Hall A configuration has many different IOCs in charge of the different components of the Hall. The following systems

- beam-line : Beam position monitors, beam current monitors...
- spectrometer : magnet fields, spectrometer motion...
- cryotarget : temperature, pressure, target motion...

are all controlled using EPICS.

4.4.2 DVCS IOC

- High voltage
- XY table motion
- DC monitoring

More informations can be found at the EPICS website at the Argonne Laboratory It is based on on a EPICS server which holds all the EPICS variables from the different IOCs.

For the detector monitoring the EPICS values are also displayed on control screens in the counting house.

4.4.3 High Voltage

The high voltage crate used the standard for Hall A Lecroy 1458 crate. An ARC Net adapter was included in the DVCS IOC, this allowed to directly control the High Voltage from any program we used by linking it to the EPICS libraries. This was particularly useful for the gain balancing of the calorimeter.

4.4.4 DC monitoring

Dedicated scanning ADC VMIC-3128 were installed. These boards recorded the anode current of the PMTs allowing to monitor the low energy background.

4.4.5 Gain monitoring system

The LED system will be detailed in section 5.1.2. Since the controller for the motion used serial connection, a SBS Industry Pack controller was added and a driver developed to drive the motion from EPICS. This allowed to have control of the motion of the LED in front of the calorimeter from the script which was driving the LED.

4.4.6 EPICS event in data stream

This client server configuration is very flexible since any program can access to the EPICS values by sending queries to the server. This allows to record interesting EPICS values recorded in the data stream. The downside of this method is since EPICS is slower than CODA the values are not very well synchronized with the events and are mostly used for monitoring of the detectors during the offline analysis.

4.5 DAQ commissioning

We used two new pieces of electronics :

- ARS sampling
- calorimeter trigger

the calorimeter trigger and the ARS behaved as expected. The major problems we encountered with the new setup were :

- Problem with IRQ servicing
  This problem occurred when the ARS were reading a large amount of data at high rates, the symptom was that the DAQ was getting frozen. The usual triggering of the readout by CODA is usually based on interrupt request by the TIR board. When an interrupt occurs a service procedure is executed to handle it. This procedure makes the readout of the modules and transfer the data to the network. Since the VME CPU is running a real time operating system [82], tasks have to be executed within a given time. The large amount of data that could be transfered from the ARS module could be a problem since it could take too much time if two many modules were read. The solution was to switch to the polling mode of triggering : instead of waiting for an interrupt to occur on the bus to start the readout, the VME CPU is looking at regular intervals the status of the TIR to determine if a trigger has occurred. Technically this could introduce

an additional latency but this was negligible compared to the time taken to do the data transfer. This way the readout of the module does not have to comply with the stringent timing requirement of an interrupt service request since the readout is started in a regular task.

- Problem with the CODA MSQL server
  The beginning of the experiment saw frequent problem with the CODA components who could not communicated the MSQL database which monitors their state. We eventually traced the problem to the server running on the VME CPU to read the scaler on-line. One port was open for each client displaying the rates and was not released quickly enough. The result was a saturation of the TCP ports eventually preventing any network connections. This problem was fixed by using a new VxWorks version.

4.6 DAQ possible improvement

VME upgrade

The major bottleneck was coming from the VME bus since all the modules are read one after each other. The ARS board used BLT32 allowing a theoretical throughput of 40 Mb/s. But reading many different modules and using the individual channel readout is not optimized for block transfer so peak data rate was around 7 Mb/s Going to BLT64 should allow to double the data throughput without additional modifications [79]. Other VME upgrade like 2eVMe, 2eSST and the latest VXS are becoming available, using all the latest technologies could allow to reach data transfer rate at VME bus level up to respectively 80,160,320 and 1600 Megabytes per second.

Network upgrade

The most limiting factor was the transfer rate from the proton array crate since the signals turned out to be too small to use zero suppression so we relied only on the calorimeter information. This was especially the case for the neutron run where a deuterium target was used which was the least favorable : single electron rates were the highest in the spectrometer and additional channels of the proton veto (57 additional channels) detector were added to the proton array crate. The VME CPU used were MVME5100 [70] which has a 100MBit Ethernet board though PMC Gigabit Ethernet network adapter could be fitted We preferred to stay with standard equipment. Newer CPU MVME5500 or MVME6100 have standard Gigabit Ethernet. So we can conclude the even though we added a

Gigabit Ethernet line for all the crates, it would have been taken advantage of if the proton array crate had had a Gigabit Ethernet adapter.

On fly compression

The data structure of the ARS for one channel is as following. One sample is composed is coded on 16 bit.

- 4 bit for the channel to be read
- 12 bit for the amplitude

in order to take advantage of the 32 bit bus, two samples are packed in a 32 bit word. For the experiment we took alway took data with the full range of 128 samples. So many data words on different channels could be the same and use of compression algorithm before data transfer could be efficient.

Time window reduction

Another way to reduce the data is to reduce the width of the recorded window. The impact on the waveform analysis efficiency has to be determined though.

Multi-crate use

Read-put speed can be reduced by the use of additional crates since modules are read-out in parallel. Splitting modules in different crates allows to easily scale the bandwidth for the read-out of the modules.

Increased range

A modified version of the ARS board was developed allowing to use the full range of the ARS with a limited loss of linearity this could not be implemented for the experiment but only require to change a couple of resistor on the ARS daughter board. The range was limited to 2200 channels giving a input range of about 1.4 V if we used full 12 bit resolution input range would have gone up to 2.5 V allowing more flexibility and higher gain on the base amplifier.

Pipelined fast ADC

The major source of dead-time was the transfer from the ARS to the VME CPU. Pipelined ADC are now available, allowing to continuously take data which is recorded into memory buffers. This allows to transfer the data while is being done allowing a zero dead time readout. This technology is used for example on

the ATLAS detector and is also being developed for the Hall D GlueX detector. The major drawback of this electronics compared to the ARS is the price. The latest fast ADC can go up to 2.2 GHz but for 2 channels pricing is around 16 000$ while ARS board were about 4000$ for 16 channels. Since in most kinematics the coincidence trigger is of the order of tens of hertz the analog memory system is a cheap and efficient method perfectly suited for this kind of measurement.

4.7 Conclusion

We successfully commissioned the new electronics namely the ARS readout system and the calorimeter trigger module. The major drawback of our system was dead time we could have reduced the accidental trigger rates and the dead time by optimizing :

- as far as the trigger gate is concerned since studied showed that we could have gone to the minimum gate width with a small loss of efficiency.
- the ARS time window was recorded over the whole 128 ns.

but we used conservative DAQ parameters in order to be able to study accidental rates. Many improvement can still be made and parameters optimized for an more efficient data taking. If we look at the table 4.3.4 we can see that the simple network upgrade would have made negligible the network dead time allowing to win from 15 % to 5 % more data. The upgrade to BLT64 would yield from 13% to 5% more data. And going to faster technologies such as VXS could further reduce it but the need for a redesign of the board interface depends on the future measurements planned. High rate measurement would highly beneficiate of it but further measurement will most likely be high Q^2. For example for this experiment since rates are moderate for the third kinematic, it represented most of the beam time running so the gain for the total experiment with BLT64 and Gigabit Ethernet would have been closer to 10%.

Chapter 5

Detectors tests and comissioning

The calorimeter was first stacked in the clean room of the EEL (Electronic and Experimental Laboratory) which is a building located between the Jefferson lab offices and the accelerator. The detectors in an almost final setup were mounted there including electronics and support stand. In order to test all the chain from the detector to the electronics. The detector test were carried out either with cosmics or with the LED gain monitoring. A stand alone DAQ system was set up in the clean room, it used the components that would go into the spectrometer hut, the only missing components being the scattering chamber, the left spectrometer and the beam.

5.1 Calorimeter

5.1.1 Cosmics data taking : calorimeter balancing

When the detector was in the EEL we started to test of the calorimeter with cosmics to start balancing of the high voltage.

Cosmics setup

We used the calorimeter trigger associated with scintillator paddles to generate a cosmics trigger. A cosmics mode was added to the calorimeter trigger : the stop was generated by two scintillators paddles placed on top of the calorimeter black box and validation was made by the calorimeter trigger. In order to select cosmics going through the whole calorimeter a coincidence between the top row and the bottom row was also required by the calorimeter trigger 5.1.

Gain adjustement Making a cut on amplitude on blocks on the top and bottom of a column allows to select the vertical. Such high energy cosmics rays leave

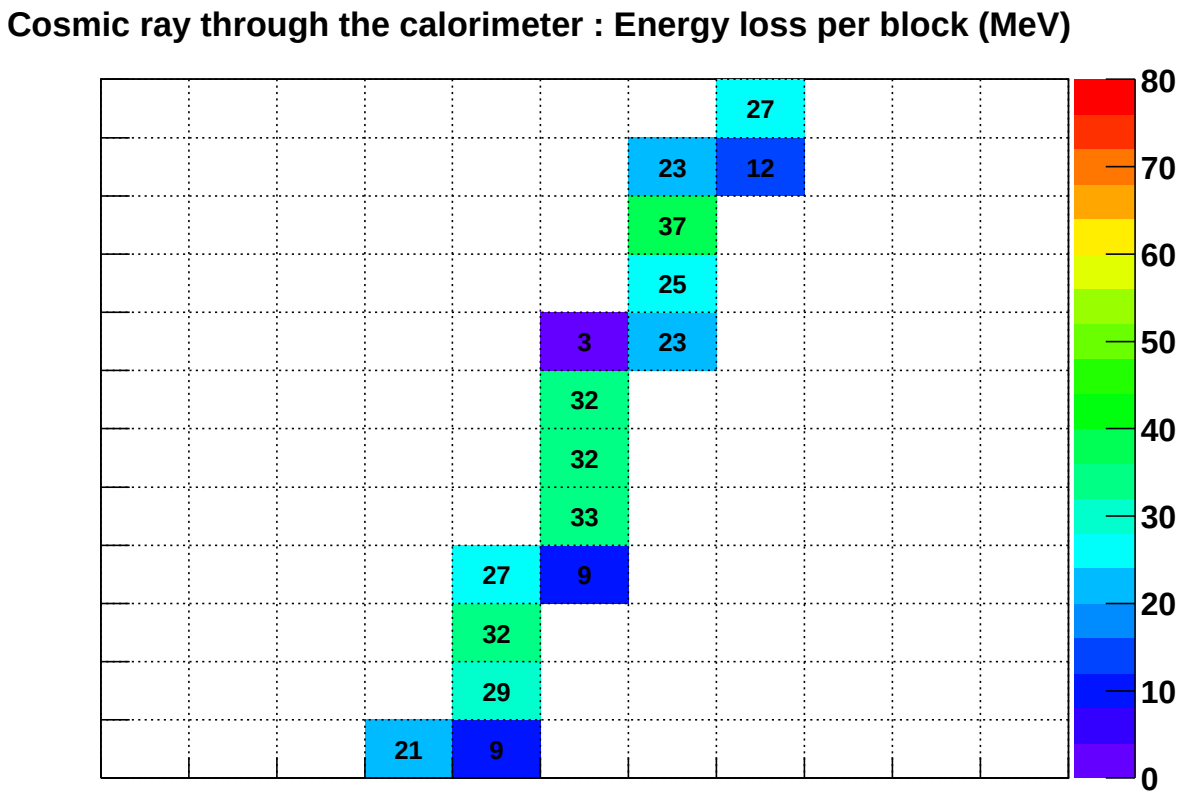

Figure 5.1: Cosmics which generated a trigger for the calorimeter

energy at the minimum ionizing value giving a well defined energy loss peak in each block allowing to balance the gain as seen on figure 5.2.

Gain balancing We used an iterative method to balance the calorimeter gain. The gain parameters of the PMT were measured in Clermont Ferrand and entered in a Mysql database. After analysis of a cosmic run the new high voltage coud be computed and sent to the HV crate. After a couple of iteration we arrived to a spread of about 6 % block to block dispersion. This was the best reachable given the fluctuations on the high voltage.

5.1.2 LED system

In order to monitor the gain variation of the calorimeter a LED [37] system was integrated to the calorimeter mechanical structure. This system was composed

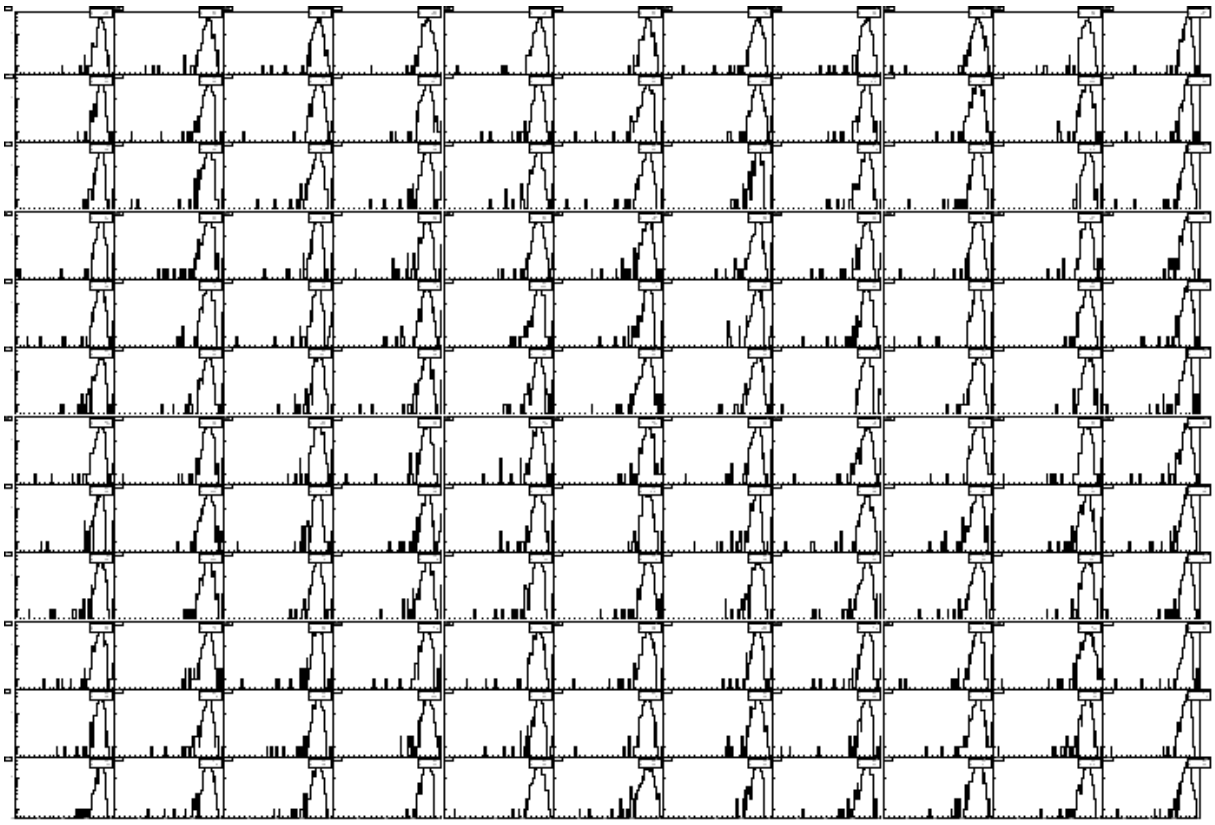

Figure 5.2: Plot of the pulse integral distibution for all calorimeter blocks with selection on vertical events

of two main components :

- A motorized axis for the calorimeter and LED motion
- A LED board to act as a reference source for gain monitoring and to check the linearity of the calorimeter blocks.

The Motorized axis

Device description The calorimeter was equipped with Festo components :

- motor MTR-AC-55-3S
- 2 electric axis DGE-18-385-ZR
- electric axis DGE-18-380-ZR

for the motion of the LED at high speed and 1 for the motion of the calorimeter with lower speed but higher torque. Each motor could be controlled using controller Festo SEC-305 through serial port. We used first the software provided to control them for preliminary tests until the EPICS software control was finished. The controls relied on a GreenSpring serial controller which allows to control 8 different serial devices. This controller is a standard VME board running in the EPICS IOC dedicated for the DVCS. The serial driver was developed from scratch by D. Wetherholt in C language to control the motors using standard EPICS controls.

Position reproducibility

The encoder range is coded on 16 bits corresponding to 65536 steps. The reproducibility is less than 500 steps, leading to a position accuracy as shown in the table 5.1.2

Axis	Steps	Position in mm	Positioning accuracy in mm
X and Y axis	65536	52	0.4
Z axis	65536	1.52	0.016

LED board

A special LED system was designed for the gain and linearity monitoring. The system is composed of two parts : the VME based controller and the LED holder. The VME controller is based on the FLEX IO board from the Jefferson Laboratory Electronics group. This is a general VME card controlled through standard VME which acts as generic interface for other devices. The custom part includes

mostly power supplies : 5V for the LED ,12V for a curing lamp and a pulse generator. The user has control on the LED pulser frequency which supplies 3 LED and the light output of the LED by changing bias on the LEDs. On the other end, the LED board holds 4 LEDs and a small neon UV lamp. 3 LEDs were pulsed following a lighting sequence which covers all the combinations of LED on and off. This allows to check any linearity change. The fourth LED is a continuous LED which could simulate the background of the experiment. The UV lamp is used to cure the calorimeter blocks in case they would become less transparent with radiation damage. This board was located in the EPICS VME crate. Since controlling the board was only consisting in writing values into VME registers, a couple of C functions were written allowing to operate the LED controller from the Vxworks shell. A server allowing to send remotely command to the shell allowed to control the LED from any other computer and was used in the final design.

LED data taking configuration

Data taking with LED mostly took place in the clean room of the EEL. A LED trigger was set using the LED signal as stop for the ARS, the timing was ajusted such that the pulse would be in the trigger and ARS window giving a validation signal for each pulse over threshold.

LED tests One major problem of this system was because of lack of space the LED system was very close from the calorimeter inducing a big sensitivity to the Z position of the LED. Because of the stacking and the parallelism of the LED movement plane we had to reduce this sensitivity using collimators. We put our effort on different devices in order to optimization Z dependence and light output. After different designs of collimators we had a dependence of 1% by millimeter which was sufficient for our purpose.

5.1.3 Continuous scans

Before EPICS was operational we used the Windows software provided with the controllers to move the LED so it was running independently from the LED and the DAQ. But making the assumption that motion is at constant speed and recording a clock we were able to check the blocks positioning and check for the block to block variations. And determine where the maximum was located.

The plot in figure5.3 shows the amplitude distribution of one calorimeter column with HV set from the coefficients so that gain is the same for all blocks . The X-axis is the scaler count of a clock. Since the motion is taken at constant speed it is equivalent to the position of the LED. Two blocks were mislabeled and

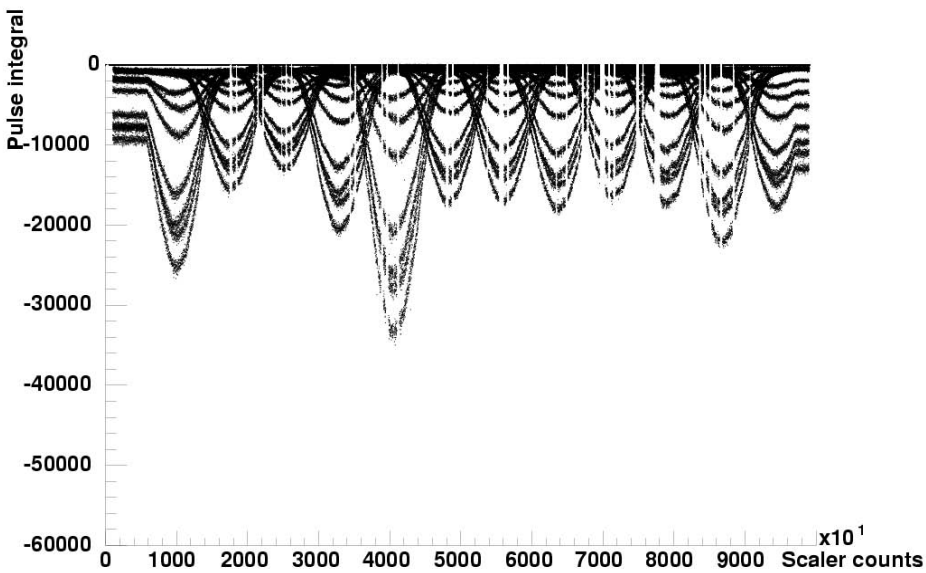

Figure 5.3: Vertical scan of one calorimeter column

thus had wrong coefficients to compute the HV which explained the amplitude spread of some channels. It was taken with the 3 pulsed LED and the LED moving at constant speed from the bottom to the top of the calorimeter. The LEDs being pulsed quickly the motion between two pulses is not visible giving 8 continuous amplitude spectra (though one is difficult to resolve by eye because the sum of two pulses was close from the amplitude of the third one). This allows to check for the parallelism of the LED, the collimation of the LED and check the distance between blocks.

5.1.4 Calorimeter LED configuration

Once the final slow control was operational, we switched to a configuration which makes a scan of all the blocks : the LED would be moved in front of each block for about 30 seconds. Dedicated runs were also taken during the proton experiment giving an estimation of the radiation damages on the blocks. One problem which occurred was that the LED was much more sensitive to surface damage of the blocks while the shower takes place a little after the surface of the blocks. So one cannot apply the attenuation factor directly but this gives an upper limit of the calibration variation of the blocks. Different studies were done with this setting.

Led light output determination

To determine the light output from the LED so that it corresponds roughly to the expected amount of light produced by DVCS photons. For this purpose we look at the distribution of amplitude of the charge recorded coming from the light by the LED. If we suppose that the fluctuations of the signal only come from the statistical variation of the LED and we take enough events we expect to have a gaussian shape with a sigma of $\sigma = \sqrt{N_{phe}}$. Since the signal is amplified by the gain G of the PMT the measured signal will have $\sigma = G\sqrt{N_{phe}}$ and the measured charge is directly proportionnal to the number of photoelectrons with the same gain factor so its mean value will be $\mu = GN_{phe}$. By dividing the mean value by the sigma one can access to the number of photoelectrons produced by the LED without determining the absolute gain of the chain. By looking at the correlation between number of photoelectrons and measured amplitude we see that the linearity is not well sastified hinting for other sources of fluctuations. Nevertheless since those fluctuations can only broaden the sigma the values we obtain are lower limits of the light yield. The data following were taken from LED run 3451 allowing to calibrate the ARS integral to a number of photoelectrons. For the determination of the sigma we subtracted quadratically the contribution from the electronic noise by using the sigma of the distribution of the pedestal. Correcting by the high voltage to have the same gain as for the elastic calibration we obtain the following calibration ARS integral to photoelectrons.

0.167	0.105	0.087	0.128	0.119	0.12	0.12	0.157	0.12	0.158	0.125
0.105	0.129	0.138	0.141	0.123	0.155	0.101	0.14	0.165	0.153	0.146
0.127	0.0754	0.132	0.164	0.091	0.095	0.123	0.115	0.112	0.118	0.074
0.136	0.107	0.141	0.159	0.144	0.124	0.099	0.184	0.126	0.122	0.207
0.159	0.141	0.124	0.097	0.127	0.151	0.114	0.113	0.149	0.115	0.161
0.131	0.134	0.082	0.139	0.125	0.085	0.127	0.137	0.089	0.131	0.118
0.090	0.138	0.13	0.11	0.119	0.156	0.148	0.159	0.118	0.106	0.129
0.133	0.125	0.145	0.13	0.111	0.13	0.165	0.127	0.161	0.12	0.090
0.046	0.128	0.13	0.085	0.102	0.096	0.091	0.12	0.164	0.123	0.106
0.089	0.133	0.147	0.127	0.122	0.142	0.162	0.134	0.136	0.112	0.143
0.153	0.142	0.134	0.133	0.142	0.11	0.13	0.123	0.113	0.188	0.06
0.114	0.058	0.117	0.142	0.086	0.137	0.112	0.087	0.129	0.132	0.083

Table 5.1: Number of photoelectrons by ARS channel for the calibration setting

This calibration will be useful for the analysis of the elastic calibration data and allows to determine the number of photoelectrons produced by the calorime-

ter.

PMT behavior with DC component

The gain variation with the DC current was checked using a simple LED setup. It used 3 LEDs, 2 pulsed and one continuous LED.

We measured the amplitude for a given high voltage value of 700 V.

The results are summarized in the following table :

DC	$\Delta G/G$	Stat. Error	Amplitude	Events	RMS
0	0.0000	0.0172	1673	3396	61
0.5	0.0030	0.0172	1678	3393	62
1	-0.0024	0.0172	1669	3397	65
2	0.0048	0.0172	1681	3398	67
5	0.0071	0.0172	1685	3381	65
9.4	0.0000	0.0172	1673	3387	66
15.1	0.0083	0.0172	1687	3393	59
25	0.0141	0.0171	1697	3403	62.66
40	0.0130	0.0171	1695	3405	64
91	0.0182	0.0172	1704	3397	86.39
352	0.0510	0.0171	1763	3400	74.93

The figure 5.4 shows that for a value of DC current lower than 100 μA the gain variation was less than an 2 %. We can notice that depending on the kind of High Voltage divider the gain slightly increases before dropping which can be seen for the point at high DC current.

We also checked the behavior of all the calorimeter PMT with the continuous LED allowing to simulate the light coming from the background during the experiment. For different values of the anode current we looked at the amplitude variation of the pulsed LED signals with different DC level induced by the continuous LED. 5 runs were taken with 5 different values of DC current as quoted in the following table.

Bias LED	Run number	DC current in μA
Bias 4095	run 4119	0
Bias 1858	run 4115	5
Bias 1823	run 4116	10
Bias 1799	run 4117	15
Bias 1777	run 4118	20

The results are summarized on figure 5.5

This test confirmed the previous test made with one PMT if the the current is limited under 20 μA gain variation is stable under 1% for most of the PMT. So

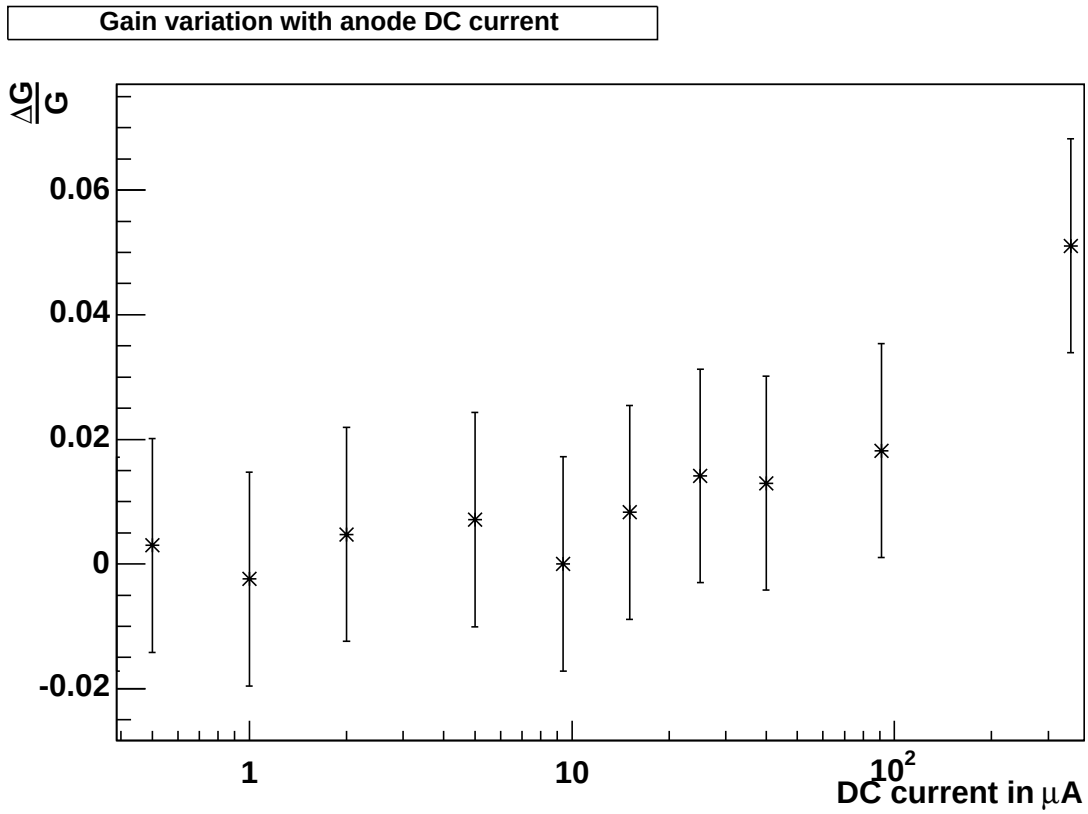

Figure 5.4: Relative gain variation with DC current at HV=700V for Hamamatsu PMT R7700

the DC current will not be a problem for the experiment as far as gain variation is concerned as long as the current value is kept under control.

5.1.5 Calorimeter LED monitoring

During the experiment LED scans of the calorimeter were made on a daily basis, allowing to monitor the radiation damage.

5.1.6 Radiation damage

On figure 5.6 we can see the attenuation coming from the transparency loss of the lead fluoride blocks and aging of the PMT. These runs were taken at the same high voltage at different time of the experiment. The figure is using the calorimeter numbering, block 0 is at the bottom left of the plot and block 131 is on the top right viewed from the back. Left means the angle θ between the calorimeter and the beam is bigger. As expected the blocks closest from the beam were more damaged.

Looking at the block at the smallest angle block 5.7, we se that variation of the gain for the proton experiment did not exceed to 10 %. Unfortunately the LED is very sensitive to the surface damage of the blocks while the shower develops a couple of millimeter farther from it. So the attenuation given by the LED cannot be applied directly to the calorimeter calibration but sets an upper limit on the gain change. The actual calibration changes of the calorimeter were determined from elastic scattering runs.

5.1.7 Conclusion

The setup in the clean room allowed to test all the experimental setup. For the calorimeter :

- calorimeter trigger and selective ARS readout was tested
- LED system and calorimeter motion were setup
- cabling of the calorimeter and mislabeling were troubleshooted
- calibration of the calorimeter using cosmics rays allowing to reach a spread of less than 6 %

the proton detector and the proton veto detector were tested the same way with cosmics rays using another DAQ setup this will be detailed in the neutron experiment related Phd thesis by Malek Mazzouz.

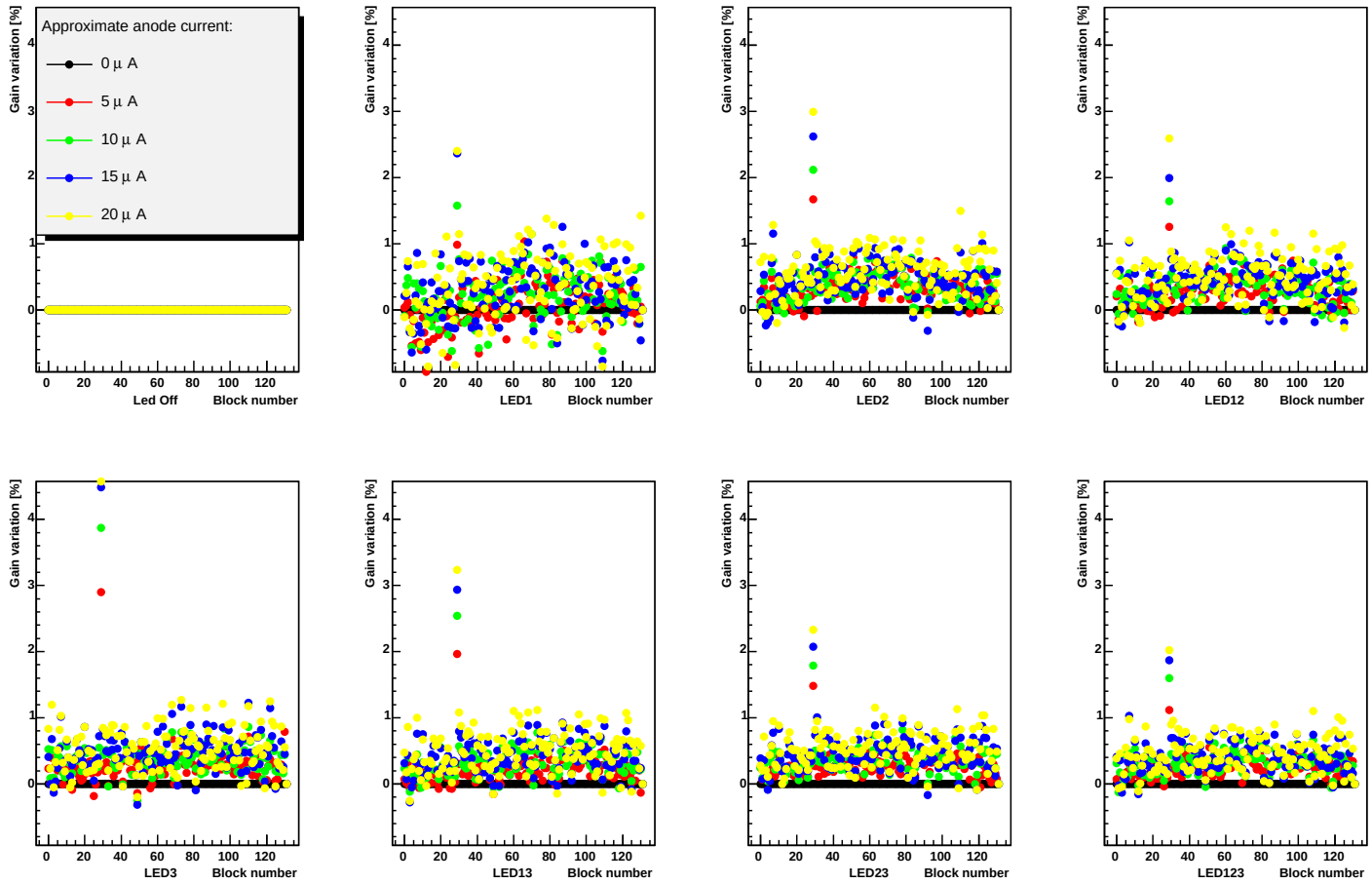

Figure 5.5: Gain variation with DC current

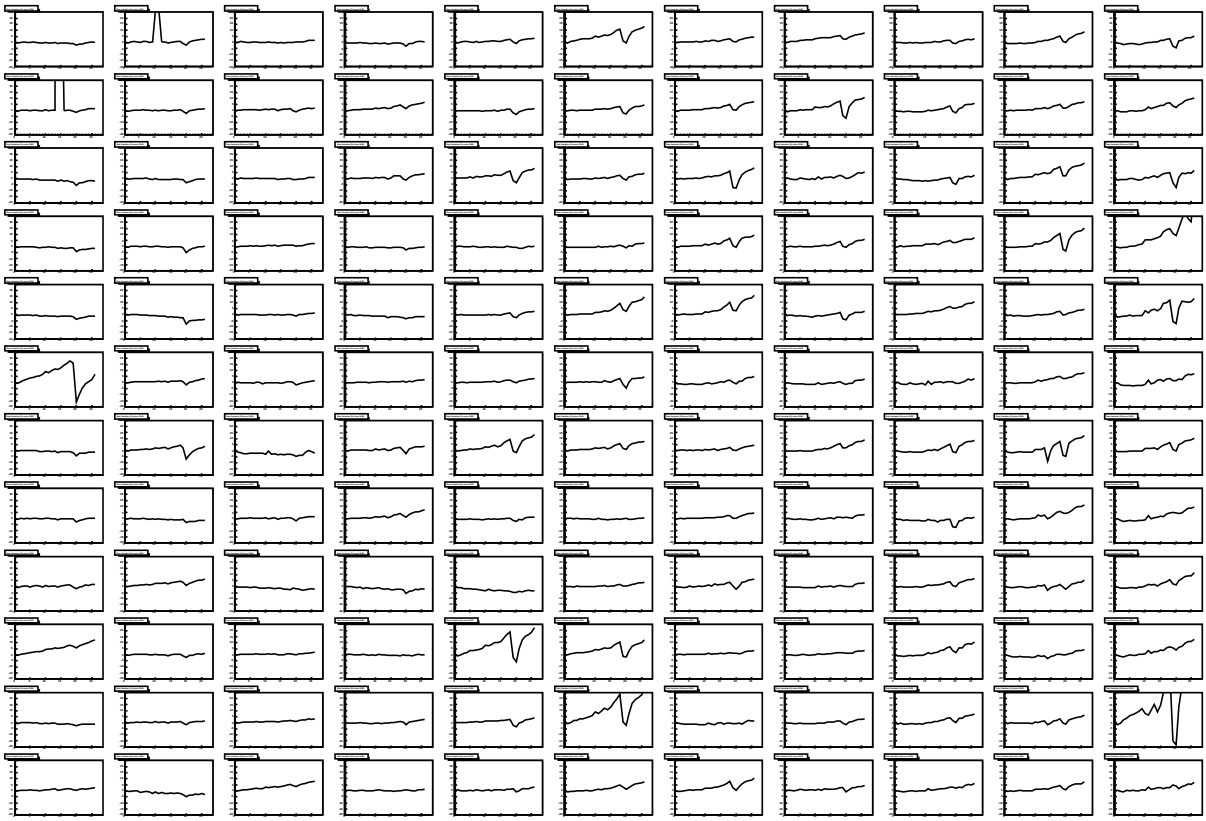

Figure 5.6: Gain variation day by day with LED on the whole calorimeter

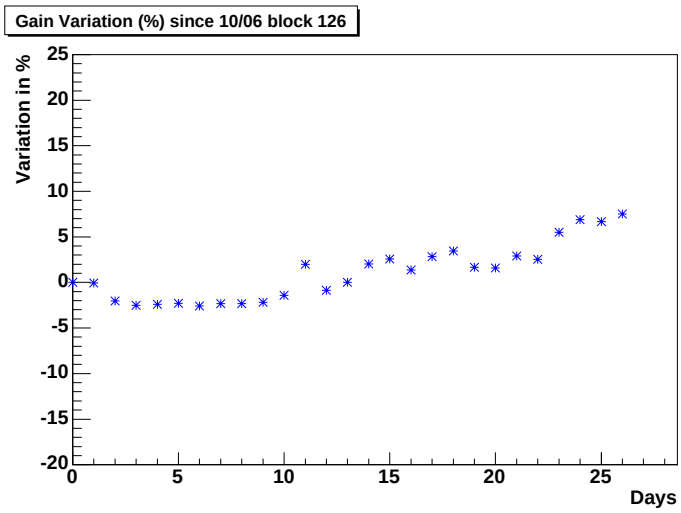

Figure 5.7: Gain variation day by day for block 126

Chapter 6

Analysis

6.1 Analysis strategy and software organization

The analysis is split in different parts depending on the detectors. The different detector specific tasks are summarized in the following list :

- Decoding and spectrometer calibration
- Waveform analysis
- Spectrometer analysis
- Calorimeter analysis
- Proton array analysis
- DVCS and pions event selection
- accidental determination
- Charge and efficiencies determination

The proton array analysis is not relevant for the work of this thesis since the analysis was done without it for more details about the proton array one can refer to the thesis on the DVCS [71] or neutron DVCS [72].

Software architecture

The DVCS part of the software relies on the object oriented ROOT framework. This is mostly a set of classes adapted to the ARS data and to the variable size event structure from the detector. For all three DVCS detectors the same

data structure was used with some small detector specific modifications : each detector has a list of read ARS channel. The base class for the DVCS analysis is the TARSWave. Each object TARSWave represents an ARS channel. This class features the different functions required to process the ARS data :

- decoding
- pedestal subtraction
- waveform analysis

Each DVCS detector has its own event structure which is a list of ARS channels to which detector specific functions or data were added. The calorimeter event has additionnal information. The TCaloEvent class contains the class holding the calorimeter and logic module data, the list of TARSWave associated and also a list of blocks which will contain amplitudes and time of the pulses in order to make the clustering. A MySQL database was setup in order to hold calibrations data for the DVCS detectors like pedestal, position, HV ...

Decoding and spectrometer

The result of the data taking is a CODA file containing raw data from the module. The first step consists to create a Data Summary Tape (DST). The raw data is cast into a structured format allowing data analysis. Different type of events are also recorded in the CODA file, so they are sorted out by event type allowing to differentiate the CODA data, the EPICS data and the scaler data. Access to the CODA event buffer are made using the CODA library which is integrated the Hall A analysis package. The Hall A Analyzer decodes and analyze the spectrometer data. By design this software allow to add detectors which have access to the CODA buffer and can extract data from it. After having defined the detector classes we added our detector to the decoding analysis loop. At the end of the process we obtain a file containing the standard Hall A data structure and the event structures for all three DVCS detectors containing.

6.2 Waveform analysis

6.2.1 Waveform analysis algorithm

The waveform analysis motivated the use of a sampling electronics. It allows to extract the amplitude of a pulse even in case of pile up. It uses the fact the signal of a PMT is linear, each pulse can be related to another pulse from the PMT by a simple scaling factor. Making this asumption all pulses can be expressed by a translation of this reference shape in time and a scaling factor to get the amplitude. We will see how this principle is implemented in the analysis software.

6.2.2 Reference shape

The reference shape is obtained using an average of pulses over runs. We took data fron the elastic setting and selected the elastic pulses for each blocks. Several iterations can be made to select a good sample of events. A first pulse is used as reference shape allowing to select one pulse events and to correct for timing change. By accumulating many pulses we are able to generate a reference shape.

6.2.3 Loop on the number of pulses

The waveform analysis is made by testing with an increasing number of pulses. Since the case with more than two pulses is CPU time consuming we limit ourselves to two pulses. Looking for many pulses can indeed be time consuming since the number of computations increases to the power of the number of pulses since the physics gain is small to resolve this kind of events the computation was limited to a search of maximum 2 pulses. The algorithm is as following :

- the test on the number of pulses, we are looking successively which number of pulses between 0 to 2 fits the data the best.

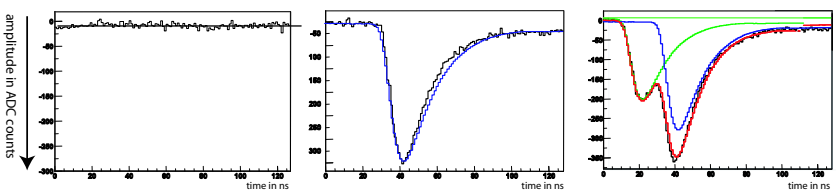

Figure 6.1: Results of the 0,1 or 2 pulses fit

- when pulses are fitted, one or more pulses are translated in time and a minimization on the amplitude of the pulses is computed for each translation.

To differentiate between those cases, three thresholds are used as input parameters : they are limit on the chi square setting a threshold between the different cases.

6.2.4 Pulse fitting function

The event data are copied into an array whose width is twice as big as the ARS time window, in order to be able to look for a pulse which happens before the point where data is recorded. To determine the pulse location, a loop over a specified time window is done. Each pulse is translated in time by one sample giving the signal to be fitted.

6.2.5 Minimzation in the case only one pulse is fitted

In order to illustrate the methode let us look at the following illustration where a one pulse fit is tried over the complete time windows. The window where the reference pulse is translated begins before the real signal so as to be able to fit the tail of a pulse before the actual recorded window.

6.2.6 Minimization on the amplitude : case of 2 pulses and constant background

This is the most general case in the analysis. Let us call A(i) the amplitude of the sample number i. We want to parametrize the data signal by a reference shape S(i) which translated in time so as to minimize the chi square.
Let n be the number of samples. For example in the case looking for 2 pulses with background

$$\chi^2(k_1, k_2, a_1, a_2) = \sum_{i=0}^{n} \left(A(i) - a_1 S(i-k_1) - a_2 S(i-k_2) - b\right)^2$$

By computing the minimization, we get the following linear system to solve :

$$\begin{matrix} \frac{d\chi^2}{da_1} \\ \frac{d\chi^2}{da_2} \\ \frac{d\chi^2}{db} \end{matrix} = \sum_{i=0}^{n} \left[\begin{pmatrix} 2S_{i-k_1}^2 & -2S_{i-k_2}S_{i-k_1} & -2S_{i-k_1} \\ -2S_{i-k_2}S_{i-k_1} & 2S_{i-k_2}^2 & -2S_{i-k_2} \\ -2S_{i-k_1} & -2S_{i-k_2} & 2 \end{pmatrix} \begin{pmatrix} a_1 \\ a_2 \\ b \end{pmatrix} - 2A_i \begin{pmatrix} S_{i-k_1} \\ S_{i-k_2} \\ 1 \end{pmatrix} \right]$$

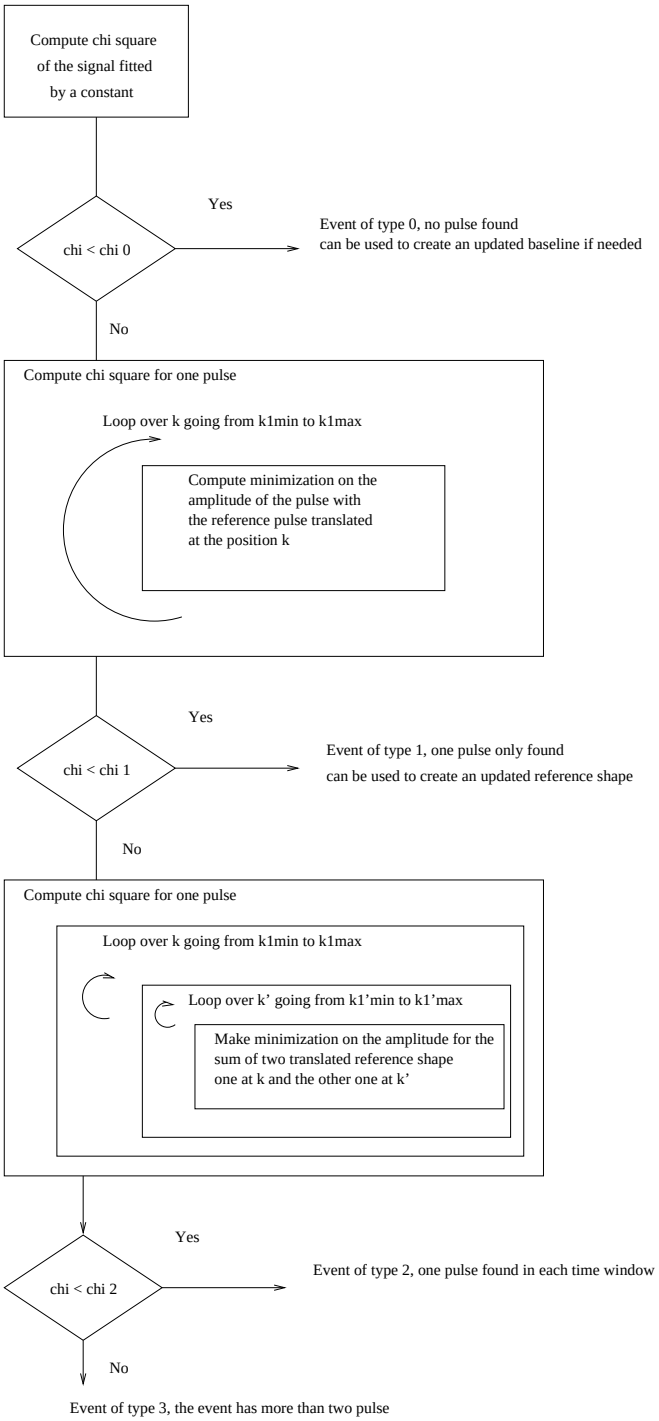
Compute chi square
of the signal fitted
by a constant
chi < chi 0
Yes
Event of type 0, no pulse found
can be used to create an updated baseline if needed
No
Compute chi square for one pulse
Loop over k going from k1min to k1max
Compute minimization on the
amplitude of the pulse with
the reference pulse translated
at the position k
chi < chi 1
Yes
Event of type 1, one pulse only found
can be used to create an updated reference shape
No
Compute chi square for one pulse
Loop over k going from k1min to k1max
Loop over k' going from k1'min to k1'max
Make minimization on the amplitude for the
sum of two translated reference shape
one at k and the other one at k'
chi < chi 2
Yes
Event of type 2, one pulse found in each time window
No
Event of type 3, the event has more than two pulse

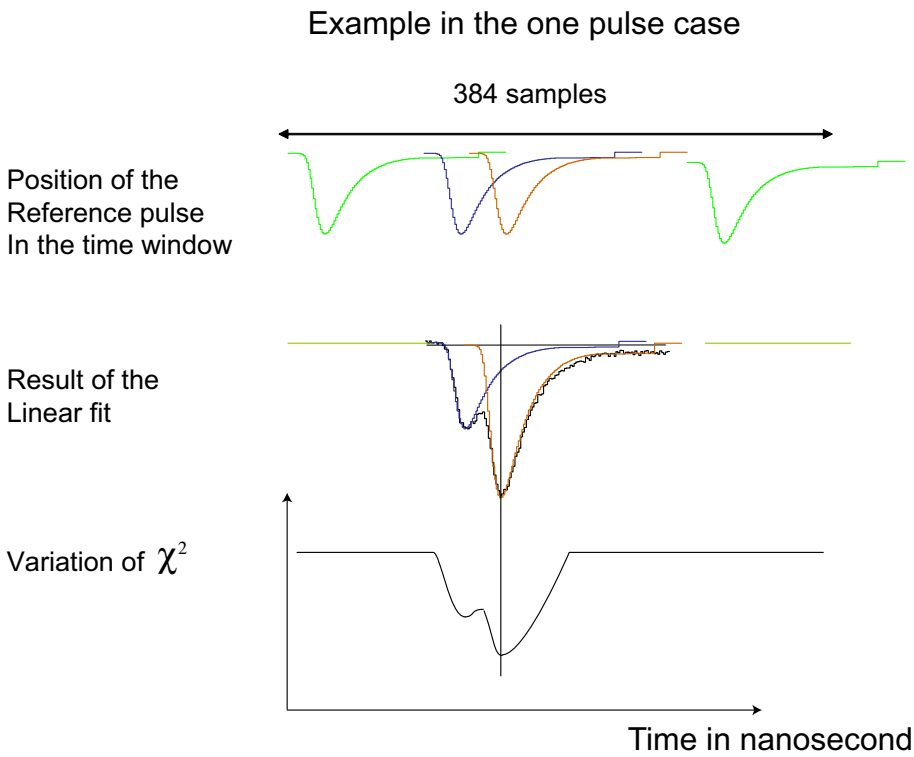

Figure 6.2: The reference pulse is translated in the time window by one nanosecond and a linear fit is performed for each of this steps. The result is the fit which has the minimal χ^2. The χ^2 variation depending on the time position of the reference pulse is schematically represented.

This quantity is minimized if :

$$\sum_{i=0}^{n}\left[\begin{pmatrix} S_{i-k_1}^2 & -S_{i-k_2}S_{i-k_1} & -S_{i-k_1} \\ -S_{i-k}S_{i-k_1} & S_{i-k_2}^2 & -S_{i-k_2} \\ -S_{i-k_1} & -S_{i-k_2} & 1 \end{pmatrix}\begin{pmatrix} a_1 \\ a_2 \\ b \end{pmatrix} - A_i\begin{pmatrix} S_{i-k_1} \\ S_{i-k_2} \\ 1 \end{pmatrix}\right] = \begin{matrix} 0 \\ 0 \\ 0 \end{matrix}$$

$$\begin{pmatrix} \sum_{i=0}^{n} S_{i-k_1}^2 & \sum_{i=0}^{n} -S_{i-k_2}S_{i-k_1} & \sum_{i=0}^{n} -S_{i-k_1} \\ \sum_{i=0}^{n} -S_{i-k_2}S_{i-k_1} & \sum_{i=0}^{n} S_{i-k_2}^2 & \sum_{i=0}^{n} -S_{i-k_2} \\ \sum_{i=0}^{n} -S_{i-k_1} & \sum_{i=0}^{n} -S_{i-k_2} & \sum_{i=0}^{n} 1 \end{pmatrix}\begin{pmatrix} a_1 \\ a_2 \\ b \end{pmatrix} = \begin{pmatrix} \sum_{i=0}^{n} A_i S_{i-k_1} \\ \sum_{i=0}^{n} A_i S_{i-k_2} \\ \sum_{i=0}^{n} A_i \end{pmatrix} \tag{6.1}$$

The cases for one pulse or no pulse are similar to this method,the system to be solved being simpler.

The terms needed to be computed at each event are the three sums of the product of the translated shape multiplied by the experimental signal (right term

).

6.2.7 Parameter settings

Several parameters have to be set in order to reconstruct correctly the pulses and to optimize the performances of the data processing.

First window

The first window is set to the size of the pulse.

Second window

The second window has to be wider since pile-up can occur anywhere in the window,so the windows is chosen to be equal to twice the width of the pulse shape plus 10% on each side.

χ^2 computation window

The parameters to set are the χ^2 threshold between the case 0,1 or 2 pulses. Since we are looking for one pulse at a certain position in time, the criteria chosen to select if the fit is good is the chi square value limited to the interval where we look for the pulse.

χ^2 square limit

The limit χ^2 square has to be computed using the calibration of the blocks in order to have the same limit in energy so for each block. The limit on the chi square for the 0 pulse case is the condition initiating the one pulse research, so this limit is equivalent to an energy threshold on the amplitude of the detected pulse. For the χ^2 limit beween the 1 pulse and the 2 pulses we took the same value as for the 0 and 1 pulse, when one pulse is fitted it is as if it was removed from the χ^2 computation so it is equivalent to the first case.

For all the analysis we set the threshold to 20 MeV.

6.2.8 Software implementation

Data parameters

Different parameters are loaded at the start of the analysis from the database :

- pedestal for the ARS

- reference shapes of the pulse
- first search window
- second search window
- χ^2 window

The left hand side of equation 6.2.6 shows that some terms do not depend on the event at all. Those can all be computed at the beginning of the program by looping on the i,j,k subscripts. The results are stored into a two dimensionnal arrays :

$$Shape2(i,j) = \sum_{k=0}^{k=256} S(k-i)S(k-j)$$

We follow the same process for the sum of the translated shape. Once the matrixes are filled the only operations which remain to be done event by event are the sums and products with the event data to extract the linear system solution.

Value choosen for analysis

Analysis window

parameter	values
Analysis window	[5,85]
χ^2 window	[-20,20]
first window	[-20,25]
first window	[-20,25]
second window	[-20,25]
first window limit	[-20,25]
second window limit	[-20,25]

χ^2 values Using the calibration for each block we determined the values

parameter	values
χ^2_0	[5,85]
χ^2_1	[5,85]
χ^2_2	[5,85]

Period	Run begin	Run end
1	2825	3146
2	4050	4382
3	4868	5109

Table 6.1: Run period used for efficiencies determination

6.3 Electron arm analysis

The spectrometer is the first detector on which the experiment relies on. It defines the virtual photon kinematics and provides particle identification information. In order to extract a cross section measurement all the detectors efficiencies and acceptances have to be determined. This is especially true for the spectrometer since it is part of the trigger. The spectrometer efficiencies were determined by M. Mazouz and more details are available in [72, 62].In order to be exhaustive on the cross section determination I will summarize the different parts of the spectrometer analysis : electron trigger efficiency determination.

6.3.1 Available spectrometer information

The spectrometer allows to select charged particle with a given kinematic by accurately setting the scattering angle and the momentum of the particle.

Triggering

Electron triggers The coincidences between S1 and S2m constitutes the T3 trigger as defined in 4.2 in order to determine the scintillator efficiency we used the T4 trigger. This trigger uses a Memory Lookup Unit (MLU) to select all the combination of 2 detectors out of the three detectors S1, S2m or Cerenkov excluding S1S2m. Runs were dedicated for efficiency measurements. These were single arm mode : both arms triggering separately on their own scintillator planes and were taken twice a day.

Trigger efficiency The first level trigger used for the DVCS is a coincidence between S1 S2 and the Cerenkov detector. And the actual trigger is a coincidence of the level 1 trigger with the calorimeter.

In order to determine the scintillator efficiencies we used the T4 triggers to select particles which went through two detectors out of three. This allows to

compute the number of missed events. If we look at the signals from the spectrometer on the trigger diagram **??** , we see that the signal of the TDC is generated by the discriminated signals from the scintillator paddles. The same logic signal is used for the trigger. So the TDC signal takes into account the threshold put on the discriminator allowing to have the actual efficiency of the trigger. If no signal from the scintillator is seen since the scintillator TDC are in common stop for S1 the time will have a very large value. We put the following cut on the particle trajectory in order to make sure the particles trajectories went through all the detectors but were not detected in one of them since this is a T4 trigger.

Following is the TDC spectrum for one paddle, the TDC are used in common start, so when no signal is seen by the paddle of S1m, the TDC value goes to the overflow value of 4095.

By using the tracking information to constrain the trajectory of the particle to go through a S1 paddle and looking at the gas Cerenkov and pion rejector and checking the number of events which gave no signal we can determine the number N2 of particle lost.

We compute the efficiency by making the ratio of the total number detected particle N1 in S1 divided by the total number of events which will be N1 plus N2 the number of particles going through S1 but not giving a signal which can be determined by looking at the TDC information. This was made using the following cuts :

- cut on the Gas Cerenkov with an amplitude greater than 500, and on the pion rejector with amplitude cut greater than 50 on the first layer and 100 on the second layer to make sure the particles selected are electrons.

- choose only one track events in the VDC

- cut on the central area of the wire chamber by choosing the x position ($-0.5 < L.tr.x < 0.5$) and the y position ($-0.2 < L.tr.y < 0.2$) to constrain the electron trajectory through all 3 detectors.

N1 and N2 have to be corrected by the prescale factors, which allowed to record preferentially a trigger by putting a prescale factor on the other ones. Typically for a TWOARM run for efficiency, the trigger rates were :

Trigger	Rate	Prescale factor
T1	2977.8	7
T3	370.3	5
T4	62.7	1

The prescale values were chosen in order to take about the same amount of T3 and T4. We can define the efficiency of the trigger by

$$eff = \frac{ps3N3}{ps3N3 + ps4N4}$$

To determine N2 for S1, one or more S2 paddles hit were required which excludes event which fires S1 since this is a T4 trigger. The resulting S_1 efficiency is shown in table 6.3.1.

Range	1	2	3
Efficiency	99.98%	99.97%	99.98%

The uncertainty is 0.01%.

The same work was one for S2 by selecting the T4 trigger and one or more paddle S1 hit and the previous cuts. Results are summarized in table

Range	1	2	3
Efficiency	99.97%	99.93%	99.94%

From this study we can conclude that the efficiency of the scintillator trigger is high and steady and we determined the correction to be applied to take into account this efficiency in the cross section.

Timing corrections The spectrometer is generating the first level trigger and the stop of the ARS, so its timing resolution impacts directly on the overall timing resolution of the data recorded. In order to obtain the best timing resolution several corrections have to be made to reduce offsets and jitters as much as possible.

Cabling offset The trigger is generated so that the right PMT of a paddle of S2m sets the timing. Depending on the high voltage and the cable length offsets in time appear paddle by paddle. These offsets are determined using the coincidence data selecting only one paddle.

Flight path correction Depending on the path followed by the particle it will take more or less time to arrive to the scintillator paddle, this mostly depend on the aberration of the spectrometer but for our acceptance a linear fit is sufficient allowing to determine the time correction depending on the dp/p.

Light propagation in scintillator correction The time for the signal to arrive to the electronics depends on the position where it hit the paddle giving to the light more or less path in the scintillator before reaching the PMT. Using the information from the VDC one can determine the position where the particle hit the scintillator paddle and thus compute the additional length to correct for.

Time-walk correction The discriminator used for triggering are not constant fraction, so the timing of the pulse will slightly depend on the amplitude of the pulse.

6.3.2 Particle identification

Gas Cerenkov

The gas Cerenkov already described in 3.2.3 allow to discriminate between pions and electrons. The signal available for this detector is the ADC value of the analog sum. On the following plot one can see the threshold on the discriminator.

Gas Cerenkov efficiency The Gas Cerenkov light is collected by 10 mirrors focusing it on one PMT. The analog sum of the 10 PMTs is a discriminated and constitutes the Cerenkov signal. We did not balance the PMT of the gas Cerenkov but we made sure the threshold on this detector was low enough to induce no inefficiencies. After the data taking we determined accurately the efficiency of the detector in order to correct for in the cross section measurement The Cerenkov signal was added to the trigger starting run 3514. Kinematic 1 counting rates in the spectrometer were high and dead-time was starting to be a problem. This eliminated the pions contamination which represented about 10% of the total number of triggers.

In order to check the efficiency of the trigger we work on the DVCS data where the Cerenkov was not in the trigger. Since the trigger is a coincidence spectrometer calorimeter, this reduces the pion contamination compared to the TWOARM runs where only a single trigger was used. To further select the DVCS events we added a cut the coincidence timing spectrum. Using this event sample, we determined that the gas Cerenkov efficiency was 99%. Contribution from electrons coming from pions-electron knockout is negligible. If we refer to the gas Cerenkov paper by Iodice et al.[52], p236, table 2] it is of the order of $2.5 \cdot 10^{-3}$. Since the pion contamination is about 10%, the contribution to the electron sample is $2.5 \cdot 10^{-4}$.

6.4 Calibrations and corrections

Since we want to obtain a cross section measurement, after determining the spectrometer efficiency we need to know the exact collected charge corresponding to the data. This done in two parts : first we can know the total beam charge delivered by the accelerator using the scaler informations provided those are well calibrated. And we need to correct this charge by the deadtime since only the charge when the DAQ is not busy has to be accounted for.

6.4.1 Deadtime

The usual deadtime measurement in Hall A is made through scalers. Scalers are counting the number of triggers and the dead-time is computed by doing the ration $\frac{N_{eventrecorded}}{N_{total}}$;

As mentioned in section **??** the deadtime measurement is taken care by scalers which measures the counts of a running clock gated by :

- the running time
- the time when the DAQ is busy
- the time when the DAQ or the calorimeter is busy

using those scaler informations, one can determine the dead time of the acquisition.

$$DT = \frac{T_{busy}}{T_{run}}$$

This value is right in the asumption that the beam is constant : in reality beam is not perfect and can be interrupted during for periods varying from a couple of seconds to several minutes, during this period the clock is still running but no charge is taken so this part of time should not be taken into account to correct for the charge as this can be seen on the plot of the clock recorded versus the spectrometer clock Fig. 6.3.

When a beam trip occur the clock continue to count but is not recorded which explains the blanks in the line. The value of the scaler at the end of the run has to be substracted with the value of time without beam. Then we can deduce the total charge recorded using the total charge from the scalers:

$$Q_{recorded} = Q_{tot} \cdot DT$$

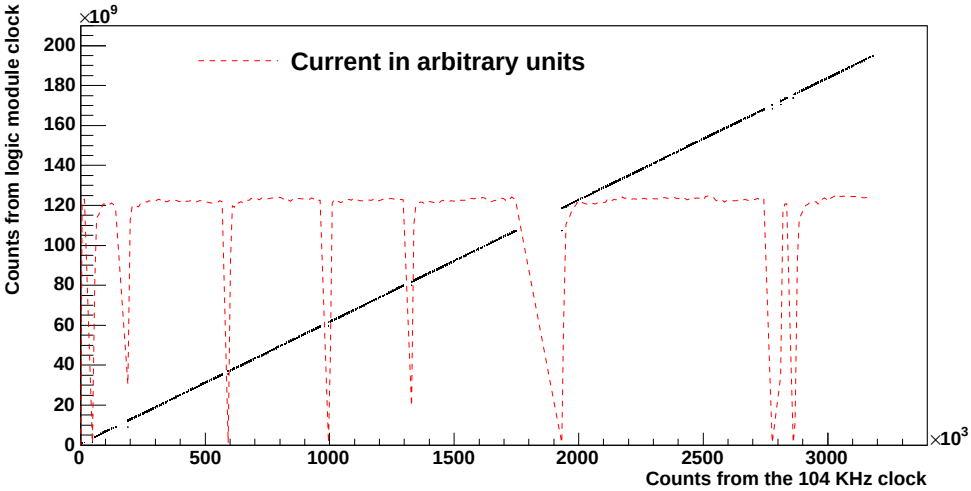

Figure 6.3: Clock used to determine the running time versus the recorded clock and the current

6.4.2 Absolute charge determination, luminosity monitoring

In order to determine the cross section, the charge delivered on the target has to be determined. We rely on the BCM descibed in Part. 3.2.1 and their scaler information. We calibrated the scalers in order to obtain the charge from the scaler values directly. The procedure was made in two parts since the usual BCM calibration procedure in Hall A cannot work a low current: one of the detector used to cross calibrate the UNSER is working poorly at low current.

Injector BCM calibration check The first step was the calibration of the injector BCM 0L02, in order to determine the absolute current a Faraday cup is used at the injector. Beam was delivered to the Faraday cup while recording both BCM and Faraday cup values.

$I_{FaradayCup}$	I_{OL02}	Relative difference
100.49 ± 0.26	100.8 ± 0.20	0.4
50.12 ± 0.33	49.87 ± 0.32	0.5
21.84 ± 0.09	21.75 ± 0.09	0.4
10.16 ± 0.03	10.17 ± 0.03	0.1
5.09 ± 0.02	5.10 ± 0.02	0.2
2.26 ± 0.01	2.23 ± 0.01	1.3
1.206 ± 0.006	1.15 ± 0.006	5.2
0.668 ± 0.003	0.539 ± 0.0004	24

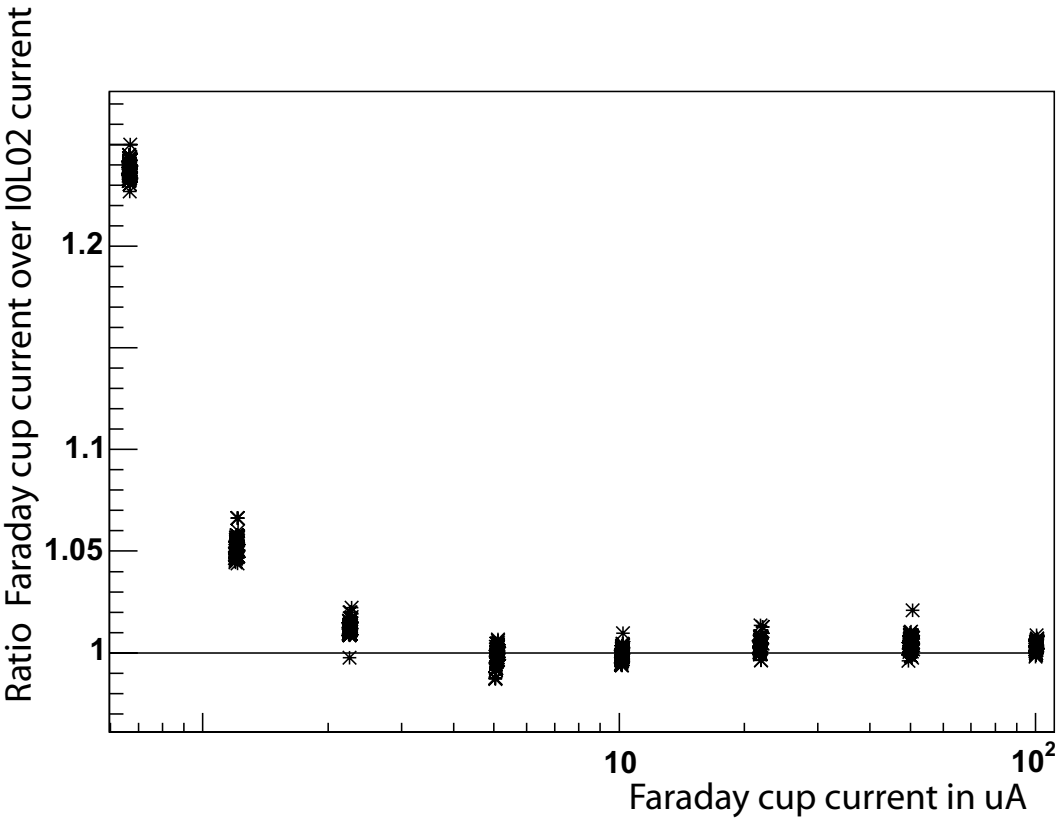

Figure 6.4: Ratio of Faraday cup current over I0L02 BCM current versus delivered

The data shows that 0L02 was already well calibrated with the Faraday cup. For current higher than 3 μA the two devices agree to less than the 1% level.

Hall A BCM scalers calibration Using the used BCM I0L02 as reference, we calibrated the scalers associated with the two Hall A BCM. We also used the right arm as a luminosity monitor, it was set at 0.6 GeV/c at 70 degrees, so we calibrated the rates with the current at the same time.

Run	Current	T_1	T_3	u_{10}	d_{10}
4191	1.106 ± 0.013	1563	189	13635	14445
4192	2.529 ± 0.019	3594	435	30964	32960
4193	5.031 ± 0.027	7144	865	61359	65435
4194	10.689 ± 0.102	15163	1846	120690	139515
4196	15.587 ± 0.635	22008	2675	191234	203898
4198	20.510 ± 0.231	28825	3505	250085	267026

By doing a linear fit on the scalers values over the different runs, the following calibration constants and offset were determined

BCM	Calibration	Offset
u_{10}	12226 ± 29	268
d_{10}	13038 ± 26	206

So we determined the calibration constants for the scaler allowing to determine the integrated charge of each run.

Polarimetry

Moeller measurement A Möller measurement was performed to check the polarization of the beam on December 3rd 2004. This allows to check the beam polarisation. The beam polarization

$$Pz = -76.8\% + / - 0.1(stat) + / - 3(syst)$$

We left the standard DAQ running during the Moeller measurement in order to determine the sign of our asymetry. In order to do so we looked at the beam charge asymetry. For the moller measurement, it had a constant sign negative. For our DAQ we also determined the charge asymetry using the scaler data recorded which turned out to be of opposite sign from the Moeller. So we can conclude that our DAQ and the Moller measurement are of opposite sign allowing to determine the beam polarization unambiguously from the helicity signal.

Compton measurement The beam polarization was also continuously recorded using the Compton Polarimeter.

The average value is 75.32 % which is consistant with the Moeller measurment.

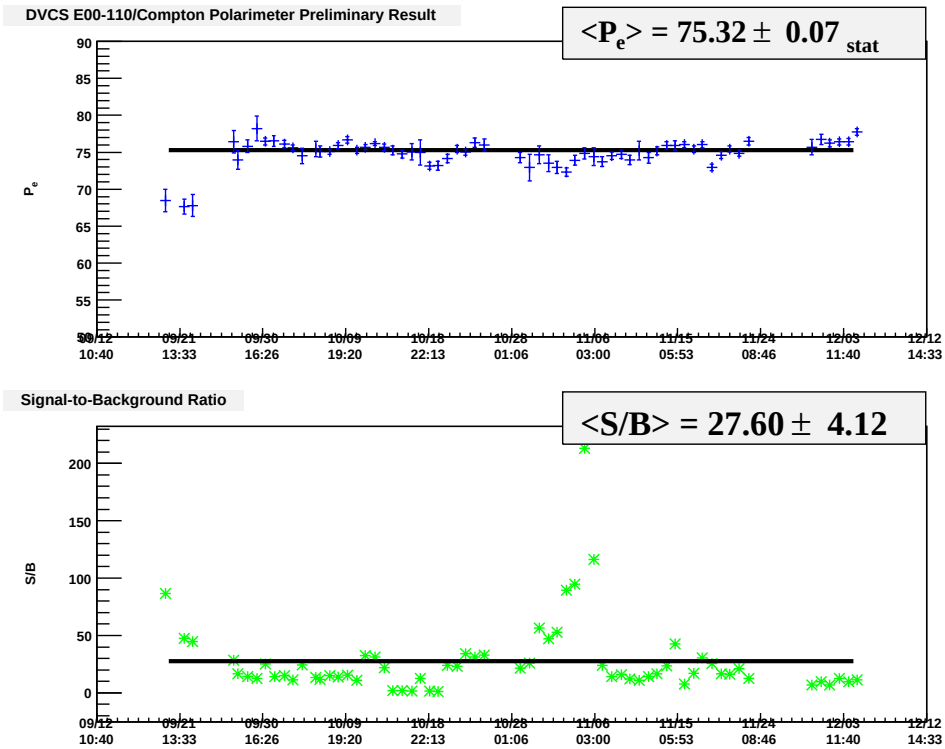

Figure 6.5: Online results of Compton Polarimeter using the electron detector

6.5 Calorimeter analysis

6.5.1 Clustering algorithm

The clustering algorithm determines how many clusters are present in the event and which blocks belong to the cluster. Summing over the blocks of one cluster allows to achieve the best energy and position resolutions. The clustering algorithm relies on the cellular automaton concept which is described in the article by V. Breton [20]. Firstly the local maxima are determined. Then an iterative process is applied where each calorimeter block follows a simple set of rules. This can be illustrated using the virus image. The blocks containing a maximum value are infected by the virus. Each neighboring blocks whose value is above a common set threshold are then contaminated unless they were already contaminated : the value of the maximum is copied into it and the next iteration starts and so on until the neighboring blocks reach the energy threshold.

6.5.2 Position reconstruction

Center of shower determination

Once the energy is determined the position of the cluster is determined using a logarithmic weighting of the block center positions for the x axis, x_i are the centers X coordinates :

$$x = \frac{\sum_i w_i x_i}{\sum_i w_i}$$

with

$$w_i = max\{0, [W_0 + ln(\frac{E_i}{E})]\}$$

Following is the position distribution of the events on the calorimeter for the π_0 for the third kinematic.

Once the position of the hit of the photon is known at the surface of the calorimeter, since we know the vertex position thanks to the spectrometer information, we can determine the photon four-momentum.

6.5.3 Elastic scattering calibration

Several calibration runs were taken in order to calibrate the calorimeter. We used elastic scattering on the LH2 target taking protons in the left spectrometer and electrons in the calorimeter. In order to cover the calorimeter acceptance the calorimeter was put back at 5.5m.

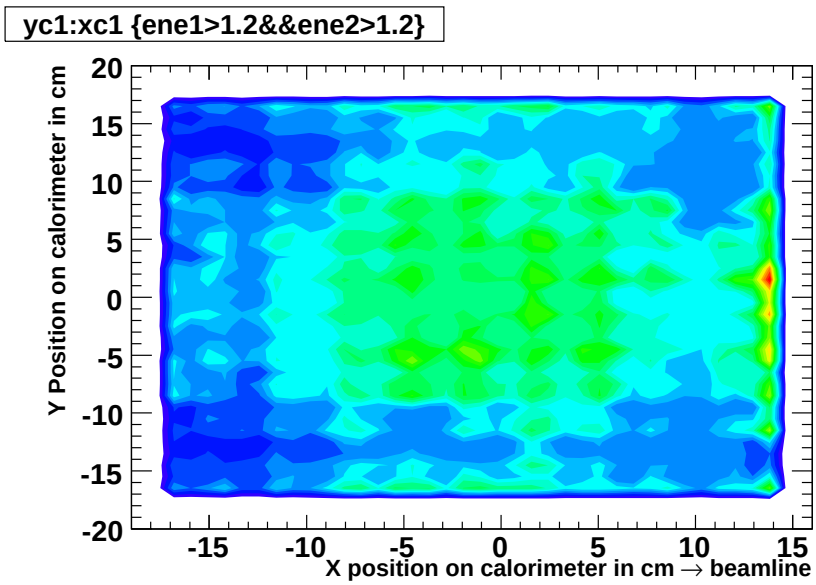

Spectrometer angle in degrees	Spectrometer momentum in GeV/c	Calo angle angle	Electron energy in GeV
36.48	2.489	-20.50	4.03
37.69	2.381	-20.50	4.13
39.41	2.234	-20.50	4.27

These 3 kinematic settings allow to cover the whole calorimeter.

Spectrometer calorimeter elastic proton selection

Protons were selected in the spectrometer by cutting on the elastic line of the spectrometer. Looking at the focal plane 6.6, on a momentum versus the tangent of the angle phi (angle of the outgoing proton in the focal plane) one can select the elastic lines.

Since the scattering is elastic the proton determines the energy of the electron.

Calorimeter calibration coefficient determination method

We used a linear minimization method to determine the calibration coefficients for the calorimeter blocks. Let us call C_k the calibration coefficient of the block number k E_k the measured energy in block k , E_{inc} the incident energy, E_{th} is the expected electron energy deduced from the proton.

By definition :

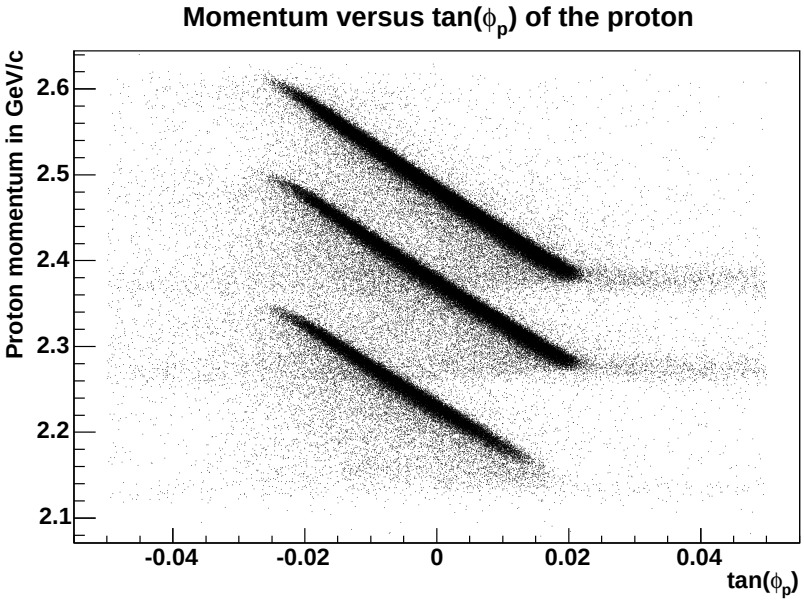

Figure 6.6: Elastic lines for the 3 elastics settings

$$E_{th} = \sum_{i=0}^{131} C_i E_i$$

we have 132 unknown coefficients.

Measuring N events, we determine the coefficient C_i by minimizing the χ^2 as follows.

We denote E_k^j energy in the block k of the j th event

$$\chi^2 = \sum_{i=0}^{N} \left(E_{th} - \sum_{i=0}^{131} C_k E_k \right)^2$$

For i varying between 0 and 132

$$\frac{\partial}{\partial C_i}\chi^2 = \frac{\partial}{\partial C_i}\left(\sum_{j=0}^{N}\left(E_{th}^j - \sum_{k=0}^{131} C_k E_k^j\right)^2\right) \tag{6.2}$$

$$= 2\sum_{j=0}^{N}\left(E_{th}^j - \sum_{k=0}^{131} C_k E_k^j\right) E_i^j \tag{6.3}$$

χ^2 is minimized when the above quantity is set to zero which leads to

$$\sum_{j=0}^{N}\sum_{k=0}^{131} C_k E_k^j E_i^j = \sum_{j=0}^{N} E_{th}^j E_i^j \tag{6.4}$$

$$\sum_{k=0}^{131}\sum_{j=0}^{N} C_k E_k^j E_i^j = \sum_{j=0}^{N} E_{th}^j E_i^j \tag{6.5}$$

$$\sum_{k=0}^{131}\left(C_k\left(\sum_{j=0}^{N} E_k^j E_i^j\right)\right) = \sum_{j=0}^{N} E_{th}^j E_i^j \tag{6.6}$$

The linear system can be summarized in the matrix form

$$MC = E$$

where C is defined as the vectors

$$C = \begin{pmatrix} C_0 \\ \\ C_n \end{pmatrix}$$

c

$$E = \begin{pmatrix} \sum_{j=0}^{N} E_{th}^j E_0^j \\ \\ \sum_{j=0}^{N} E_{th}^j E_n^j \end{pmatrix}$$

And the matrix elements of the matrix :

$$M_{ij} = \sum_{k=0}^{N} E_i^k E_j^k$$

At the end of the process inverting the matrix allows to get the calibration coefficients.

We made two elastic calibration runs where we detect elastic electrons in the calorimeter by switching the polarity of the left arm. We thus look at the elastic electron proton scattering.

$$ep \rightarrow ep$$

We obtained for the first eleastic data set.

3.190	3.266	3.436	3.483	3.542	4.239	3.327	3.951	3.365	3.965	3.673
3.240	3.604	3.523	3.417	3.832	3.704	3.845	4.692	4.599	3.808	4.524
3.186	3.410	3.246	3.601	4.005	3.668	3.957	4.038	3.885	6.026	4.158
3.230	3.190	3.410	3.546	3.649	3.683	3.705	3.894	3.914	4.172	4.409
4.841	3.441	3.644	3.954	3.866	3.884	3.522	3.817	3.539	3.775	4.711
4.151	3.862	3.555	3.522	4.032	3.641	3.758	3.654	3.440	3.661	3.780
3.254	3.853	3.530	3.529	3.679	3.990	3.412	3.476	4.444	4.097	4.329
3.148	3.343	3.611	3.641	3.438	3.451	3.937	3.391	3.846	3.784	3.753
3.532	3.567	3.539	3.372	3.228	3.537	3.689	3.474	3.859	3.499	4.513
3.727	3.500	3.316	3.555	5.001	3.903	3.510	3.411	3.719	3.698	4.060
3.263	3.602	3.568	3.792	3.815	4.201	2.974	3.515	3.673	3.585	3.971
3.702	3.418	4.020	3.632	3.460	3.559	4.136	3.628	3.573	3.939	3.494

For the second data set which was taken towards the end of the experiment we could the the effects of radiation damages.

3.297	4.231	3.892	3.689	3.751	5.720	3.675	4.755	3.665	4.623	3.927
3.423	3.692	3.744	3.720	4.433	4.393	4.456	6.210	5.567	4.464	5.671
3.225	3.426	3.423	4.054	4.921	4.249	5.385	4.359	4.072	7.666	4.867
3.314	3.406	3.591	3.621	3.860	3.979	4.629	4.340	4.342	6.063	8.652
4.953	3.395	3.894	4.362	4.451	4.386	4.084	4.091	4.253	4.198	6.032
6.708	4.320	3.721	3.778	4.477	4.145	4.204	4.190	3.686	4.331	4.421
3.360	4.777	3.710	4.153	5.044	4.945	3.741	4.061	5.251	5.309	5.362
3.580	3.422	3.817	4.061	3.584	3.696	4.734	3.740	4.183	4.556	4.519
5.135	4.582	3.528	3.349	3.137	3.902	4.236	3.785	4.489	3.798	5.711
5.803	3.565	3.507	3.688	8.317	5.059	3.826	3.738	4.480	4.320	5.095
3.334	3.867	3.821	4.224	4.586	6.779	3.190	3.802	4.214	4.034	8.699
3.947	3.549	4.753	3.821	3.704	4.356	5.079	4.264	4.022	4.690	4.152

Following is the table of the relative calibration coefficient changes.

0.032	0.228	0.117	0.056	0.056	0.259	0.095	0.169	0.082	0.143	0.065
0.053	0.024	0.059	0.081	0.136	0.157	0.137	0.244	0.174	0.147	0.202
0.012	0.005	0.052	0.112	0.186	0.137	0.265	0.074	0.046	0.214	0.146
0.025	0.063	0.050	0.021	0.054	0.074	0.200	0.103	0.099	0.312	0.490
0.023	-0.014	0.064	0.094	0.132	0.114	0.138	0.067	0.168	0.101	0.219
0.381	0.106	0.045	0.068	0.099	0.122	0.106	0.128	0.067	0.155	0.145
0.031	0.193	0.049	0.150	0.271	0.193	0.088	0.144	0.154	0.228	0.193
0.121	0.023	0.054	0.103	0.041	0.066	0.168	0.093	0.081	0.169	0.170
0.312	0.221	-0.003	-0.007	-0.029	0.094	0.129	0.082	0.140	0.079	0.210
0.358	0.018	0.054	0.036	0.399	0.229	0.083	0.088	0.170	0.144	0.203
0.021	0.069	0.066	0.102	0.168	0.380	0.068	0.076	0.128	0.111	0.544
0.062	0.037	0.154	0.049	0.066	0.183	0.186	0.149	0.112	0.160	0.158

The last calibration was taken at the end of the experiment and showed that radiation damage followed the dependence with theta but with some spurious variations going up to more than 50% for a couple of blocks. The difference between block could come from different impureties between the different batch of blocks.

Calorimeter resolution

For the elastic data, we can determine the calorimeter resolution by looking at the reconstructed energy and angle versus the predicted energy and angle of the electron of the proton this can be seen on figure 6.7.

At 4.2 GeV this gives

$$\frac{\delta E}{E} = 2.7\%$$

$$\delta\theta = 1.8mrad$$

$$\delta\phi = 1.3mrad$$

Light yield from the calorimeter

Using the ARS calibration determined from the LED, we can give a lower limit to the number of photoelectrons produced by the Lead Fluoride blocks for a 1 GeV by energy.

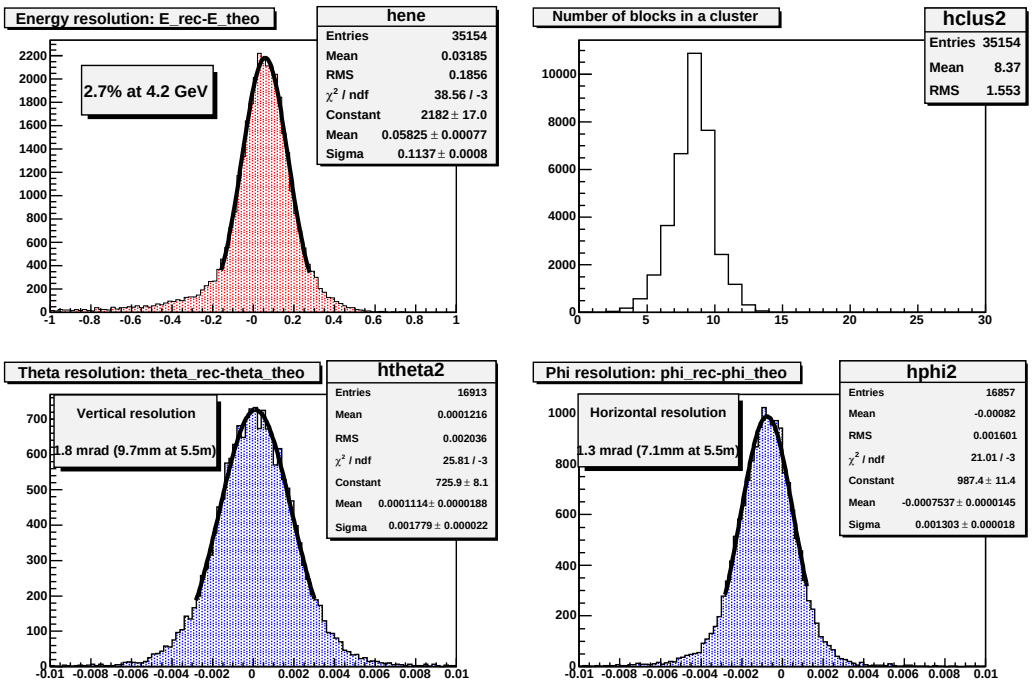

Figure 6.7: Calorimeter resolution determined from the elastic scattering data

598	273	342	478	432	552	451	671	464	648	480
388	473	521	558	500	658	408	652	707	613	627
444	267	507	632	404	391	579	442	520	529	311
488	407	519	566	523	459	435	703	497	622	490
567	489	468	363	526	581	462	410	625	442	715
745	537	294	520	487	341	500	556	344	545	479
330	588	484	451	580	675	560	644	502	485	569
525	463	518	513	409	500	704	487	631	503	380
229	587	468	292	347	376	360	486	685	449	483
479	484	543	464	695	648	604	517	586	447	621
543	547	503	512	579	616	488	453	460	765	471
423	206	484	510	314	605	471	353	503	554	357

6.5.4 Calorimeter trigger

ARS and calorimeter trigger calibration

Using data from run 4255, the linearity of the trigger with the ARS was checked by plotting the ARS waveform amplitude versus the trigger value. The ARS Waveform analysis was calibrated with the elastic data. This run gives the calibration constant conversion between trigger and energy, the correspondence is about 40 MeV for one trigger ADC count.

Trigger pedestal is usually around 25 counts. In order to have a bigger dynamic range an offset is subtracted and an individual offset is added in order to compensate channel to channel differences. General offset applied to each channel was 18 and individual offsets ranged from 0 to 7 counts so that actual pedestal value was around 9 counts.

The threshold was set to 57 counts for most of the experiment. With a pedestal of 9 on each block this gives an energy threshold on the tower of about 850 MeV. Using the actual pedestal values and corresponding calibration constants, the plot 6.8 show the actual thresholds on the tower triggers after the first calibration. Some thresholds values reach 1.1 GeV but this should not affect DVCS events where the photon energy is more than 2 GeV and in the analysis a cut on the energy is made at 1.2 GeV.

6.5.5 Trigger read-out topology

As it was describe in the part 4.3.2, the calorimeter trigger selects given topology. Since only towers above threshold are read-out each tower being a sum over 4 blocks.

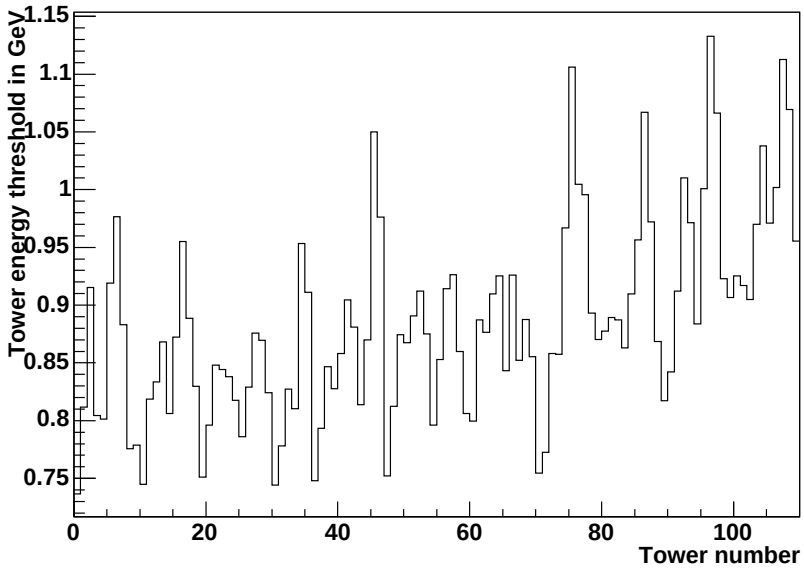

Figure 6.8: Thresholds on calorimeter tower

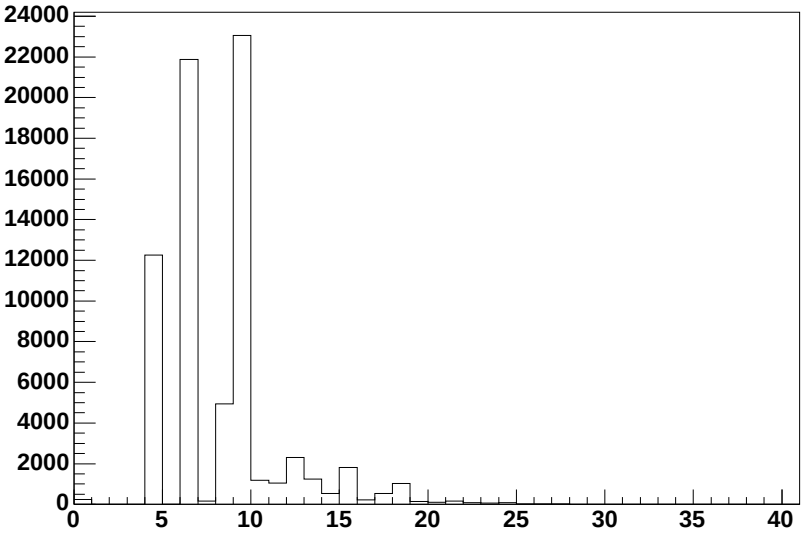

Figure 6.9: Number of blocks read out by event

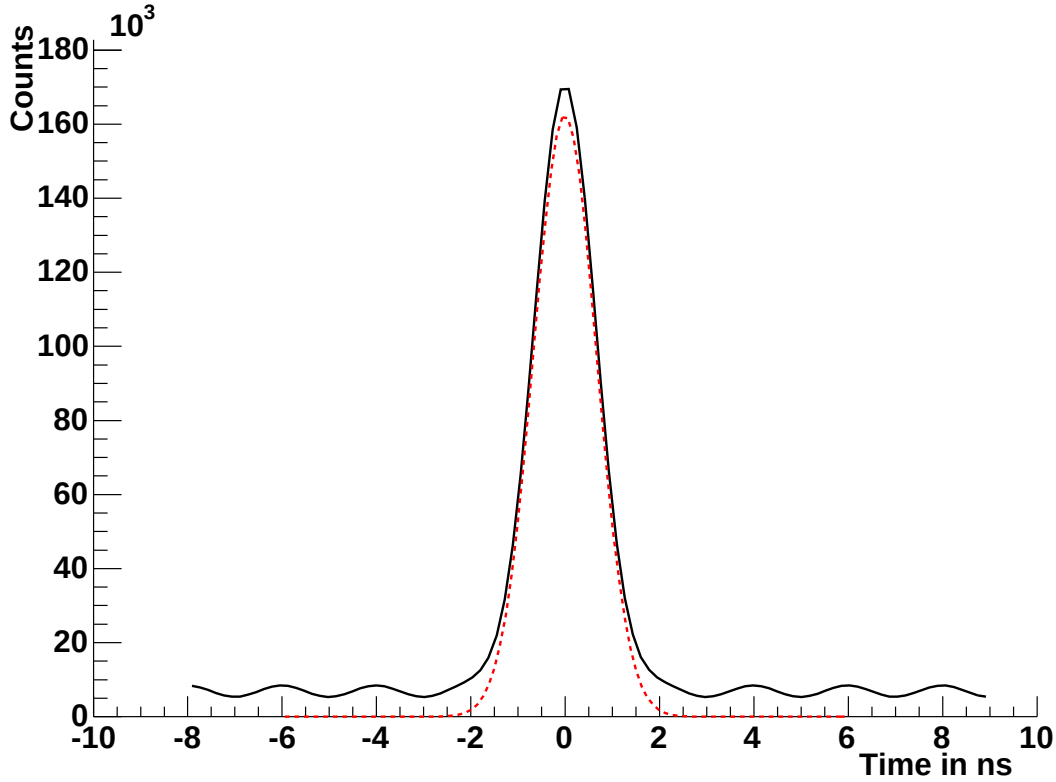

Figure 6.10: Calorimeter left spectrometer corrected time coincidence spectrum for kinematic Q^2=2.32 GeV^2

6.5.6 Calorimeter corrected coincidence time : timing resolution

The stop for the calorimeter ARS is done by the S2m scintillator so the coincidence timing has to be corrected for the spectrometer correction and the offset from the electronics.

Using the spectrometer and calorimeter timing corrections we get a timing resolution of 0.66 ns Fig 6.10. The resolution depends on the energy cut for this timing spectrum a cut at 300 MeV in a block was made.

6.5.7 DVCS data : photon vertex reconstruction

The informations from the clustering gives the position where the photon hit on the calorimeter surface. Using the calorimeter position from the survey : calorimeter angle, distance of the calorimeter, block position we can obtain the coordinate of this point in the Hall. The spectrometer information on the electron allow to determine the position of the vertex which combined with the calorimeter information gives the electron direction. The photon four-momentum is thus completly determined having the direction and energy of the photon.

Pile-up effect on calorimeter trigger

Since all the signals are AC couple the zero lies in fact at the position of the DC component produced by the pile-up of low energy particle. Fluctuations of the DC component can thus produce either positive or negative shift widening the pedestal. For the channel closest to the beam, pedestal width induced a couple false trigger due to positive values which give a high ADC value because the value goes around be above zero but these events represent no more than 0.3 % of the events.

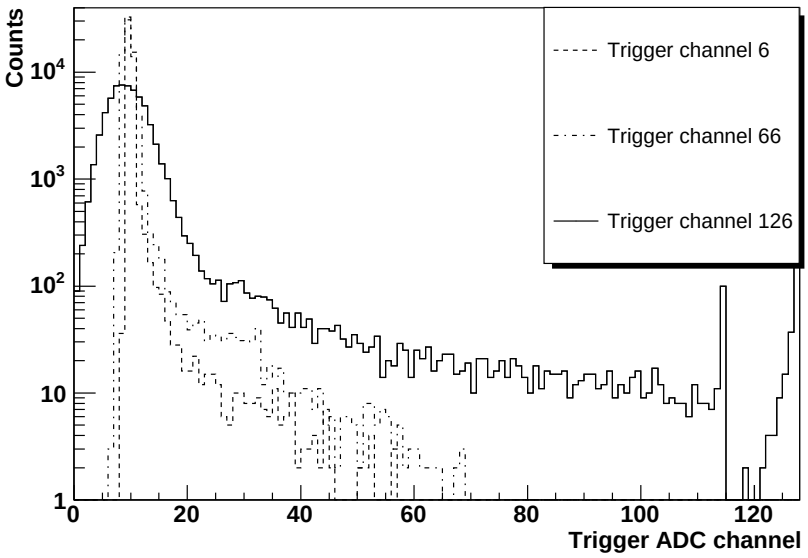

Figure 6.11: Trigger pedestal for block 6 (23 degrees) block 66(15 degrees) and block 126 (7 degrees)

RMS of the calorimeter pedestal :

1.79	1.62	1.98	2	2.27	1.64	3.04	2.1	3.14	3.39	4.66
1.69	1.97	2.1	2.21	2.31	2.27	2.24	1.9	3.06	4	4.46
2.02	2.03	2.35	2.19	1.92	2.64	2.08	3.39	3.2	2.95	4.49
2.2	1.98	2.34	2.38	2.7	3.03	2.73	3.39	4.3	3.59	7.33
1.33	2.48	2.23	2.01	2.31	2.3	3.39	3.73	4.51	6.33	5.67
1.54	1.94	2.46	2.68	2.31	2.8	3.66	4.66	5.91	7.09	12.6
2.12	1.79	2.45	2.42	2.26	2.48	4.11	4.68	3.85	4.41	8.2
2.2	2.26	2.35	2.26	3.18	3.29	2.78	4.45	4.37	6.3	9.68
1.6	1.53	2.41	2.72	3.44	2.92	2.73	4.31	4.1	6.34	6.03
1.16	2.07	2.49	2.55	1.24	1.9	3.33	3.77	3.54	5.17	6.29
1.95	1.77	1.83	1.89	2.22	1.63	3.61	2.95	3.36	3.93	3.18
1.48	2.04	1.49	2.17	2.55	2.29	1.96	2.67	3.64	3.27	5.15

Table 6.2: Pedestal width depending on the block

Accidentals and pile-up determination

The ARS data allowed to select good events from accidental ones by cutting on the coincidence time. One can select the good events by selecting the ones in the coincidence peak and accidentals cutting outside of the peaks. One can see the 497 MHz beam structure in the accidental background each bump corresponding to an electron bunch by parameterizing each bump with a Gaussian distribution we can determine the signal over noise ratio since the electron bunch are equivalent they will have the same sigma. So we parametrize the timing spectrum by the following distribution :

$$F(t) = A_c e^{-\frac{(t-\phi)^2}{2\sigma^2}} + \sum_{i=-k}^{+k} A_a e^{-\frac{(t-\phi)^2}{2\sigma^2}}$$

extracting A_c and A_a one can compute the respective probabilities to have an electron in the coincidence peak or in an accidental bunch.

This can be done for different cut of energy allowing to have the timing resolution depending on the energy and on the angle theta.

24	22	21	20	18	17	16	14	13	12	11
24	22	21	19	18	16	15	14	12	11	10
23	22	20	19	17	16	14	13	11	10	9
23	21	20	18	17	15	14	12	11	9	8
23	21	20	18	17	15	13	12	10	9	7
23	21	19	18	16	15	13	12	10	9	7
23	21	19	18	16	15	13	12	10	9	7
23	21	20	18	17	15	13	12	10	9	7
23	21	20	18	17	15	14	12	11	9	8
23	22	20	19	17	16	14	13	11	10	9
24	22	21	19	18	16	15	14	12	11	10
24	22	21	20	18	17	16	14	13	12	11

Figure 6.12: DC current distribution on the calorimeter

6.6 Radiation damages : accumulated dose

6.6.1 Background from DVCS data on calorimeter

Measurement from the anode DC current of the PMT calorimeter

Since the PMT base and the ARS are DC coupled, the anode current of the PMT was put on a 10 KΩ resistor and sent to a VMIC3128 scanning ADC recording to monitor the total anode current drawn from the PMT. After correcting for the gain of the PMT and the pedestals we get the distribution of the DC current on the calorimeter. It respects the θ dependence of the background.

Assuming that the DC background only depends on the beam intensity and on the position. We can evaluate the dose received by the PMT using the DC current measurement. Using the beam intensity recorded from the accelerator as normalization, we can determine the dose received by the block from the low energy background which is not seen by the ARS. We directly have the measurement from the anode current, so by correcting for the gain of the PMT, we can evaluate the number of photoelectrons produced in the DC background and using the elastic calibration which gave the energy by photo-electron we can determine the energy deposited by this background.

$$Npe_{Background} = \frac{DCCurrent}{Gain} \cdot 1.6^{19}$$

We can deduce the total dose received by the calorimeter using the durations for the 3 kinematics (9 days of Kinematic 1,15 days of kinematic 2,14 days kinematic 3 ,),

We have values of the DC current for the three different kinematic, allowing to determine the instantaneous dose received by each block. By normalizing by

187	390	346	354	458	330	773	584	1373	1595	2596
269	279	213	305	430	396	684	619	1171	1831	2300
251	525	367	329	470	739	604	1746	3123	1603	5186
303	249	309	363	598	841	1096	1317	2349	3806	1533
95	341	381	522	490	373	1214	2021	2050	4138	2259
110	269	601	427	287	1084	1430	2154	4392	3866	7236
347	141	457	400	357	458	1299	1800	1859	3031	3660
229	329	363	399	815	987	883	2178	1870	3367	7029
514	150	415	744	892	895	1375	1797	1841	4114	3720
153	297	353	447	175	334	1038	1610	1608	2903	3036
255	198	243	244	411	278	971	1445	1512	1665	392
260	551	191	354	755	508	606	1404	1376	1306	3996

the accelerator current we can compute the total dose received by each block.

Total absorbed dose

By integrating this absorbed doses over the length of the experiment for the 4 kinematics,

Kin	Duration
1	9 days
2	15 days
3	14 days
nDVCS	26 days

87	390	346	354	458	330	773	584	1373	1595	2596
269	279	213	305	430	396	684	619	1171	1831	2300
251	525	367	329	470	739	604	1746	3123	1603	5186
303	249	309	362	598	841	1096	1317	2349	3806	1533
95	341	381	522	490	373	1214	2021	2050	4138	2259
109	269	601	427	287	1084	1430	2154	4392	3866	7236
347	141	457	400	357	458	1299	1800	1859	3031	3660
229	329	363	399	815	987	883	2178	1870	3367	7029
514	150	415	744	892	895	1375	1797	1841	4114	3720
153	297	353	447	175	334	1038	1610	1608	2903	3036
255	198	243	244	411	278	971	1445	1512	1665	392
260	551	191	354	755	508	606	1404	1376	1306	3996

If we refer to the different articles from P. Achenbach [4] and Kozma, P[58] available on radiation damage for Lead Fluoride, we see that most of the blocks

absorbed dose of the order of a kilo rad. But the results from the LED hint that damage were more to the surface of the block most likely due to low energy electrons which can be constrained to smaller part of the block inducing a higher dose.

6.6.2 Calorimeter recalibration method

Since the gain monitoring did not allow to correct for the gain change due to the blocks transparency changes. An interpolation methode was used to have a time dependence of the the calorimeter calibration. The data from the elastic scattering calibration were used. The method described in **??** takes as assumption that the light attenuation is proportional to the charge deposited in the block.

$$\frac{1}{G^i(t)} = \frac{1}{G^i(t_1)} - \left[\frac{1}{G^i(t_1)} - \frac{1}{G^i(t_2)}\right]\frac{C^i(t)}{C^i(t_2)}$$

with

$$C^i(t) = \int_{t_1}^{t} I(x) = DC^i(t_1)Q_1(t)$$

This method was checked by looking at the missing mass resolution improvement and was applied to the processing of the calorimeter data for all the run taken.

6.7 Pion electroproduction

Though the π^0 electroproduction is a background to the DVCS, this reaction is interesting for different reasons :

- it allowed to check the calorimeter calibration using the invariant mass of the pion as a reference
- no measurement have been made so far in this kinematic range

This kind of events are anyway part of the data collected since events with two photons from a π^0 decay with energies above the threshold will be recorded. In this part we analyzed the data from the third kinematic in order to extract the π^0 electroproduction cross section.

6.7.1 Kinematic

The kinematic is similar to the DVCS with a π^0 in the final state instead of a real photon which decays in two photons.

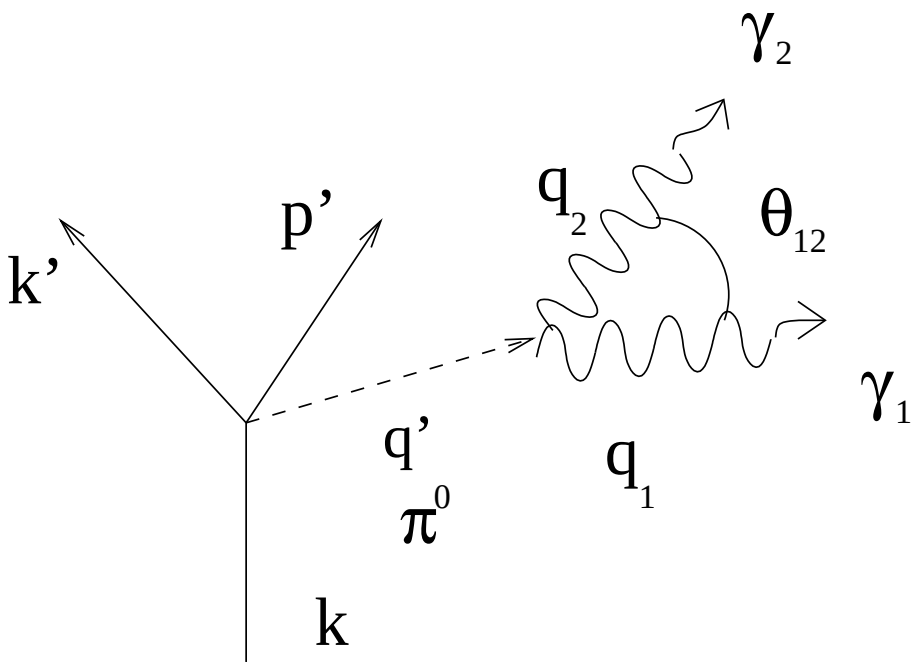

Figure 6.13: Kinematical variables

$$\begin{aligned} \gamma_1 + \gamma_2 &\rightarrow \pi_0 \\ q_1 + q_2 &= q' \end{aligned} \tag{6.7}$$

$$k1.k2 = E_1 E_2 \sin^2 \frac{\theta^2}{2}$$

$$\begin{aligned} |q_1 + q_2| &= q_1^2 + q_2^2 + 2q_1 q_2 \\ |q_1 + q_2| &= q_1^2 + q_2^2 + 2E_1 E_2 (1 - \cos\theta) \\ |q_1 + q_2| &= 4E_1 E_2 \sin^2\theta \\ M^2 &= 4E_1 E_2 \sin^2\theta \end{aligned} \tag{6.8}$$

For small angles, $M^2 = E_1 E_2 \theta$

Minimum angle between two photons If we call q_1 and q_2 the four-momenta of each detected photons, we have

$$q_1 \cdot q_2 = E_1 E_2 (1 - \cos\theta_{12})$$

since this quantity is a Lorentz invariant we also have from the center of mass :

$$q_1 \cdot q_2 = E_1 E_2 (1 - \cos\theta_\pi) = E^2/2$$

hence we can can deduce the angle between the two photons in the laboratory frame as a function of the energy of one of the detected photon.

$$\cos(\theta) = 1 - \frac{m^2}{2E_1(E - E_1)}$$

Deriving this expression, allows to determine that the extremum of the function is for $E_1 = E/2$ since the spectrometer is set at 2.35 GeV/c maximum $\pi_0$energy is around 3 GeV giving the smallest angle between two photons of 5 degrees which corresponds to 10 cm so 3 calorimeter blocks : so if the two photons coming from the π_0 decay are in the calorimeter they will always produce two clusters. In order to selection pions, events were select on the number of clusters and the timing cut. Events with two clusters in time in the calorimeter are likely to be π_0 events. A simple plot of the invariant mass the calorimeter edge with a cut on indeed shows a peak at the π_0 mass contaminated by background.

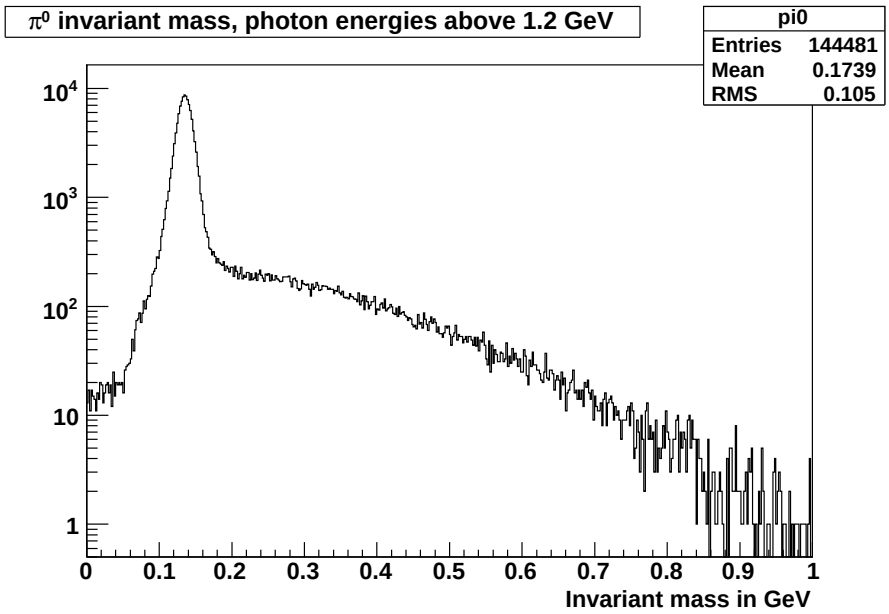

Figure 6.14: Raw invariant mass reconstructed from two photons in the calorimeter with a cut on the energy at 1.2 GeV

6.8 Data analysis

The data analyzed is for the Q^2=2.32. with calorimeter at 14.8 degrees and electron spectrometer at an angle of 23.91 degrees. The cross section is expressed in the decomposition from the paper by Drechsel [30].

$$\frac{d\sigma_\nu}{d\Omega_f dE_f d\Omega} = \frac{d\sigma_T}{d\Omega} + \epsilon\frac{d\sigma_L}{d\Omega} + \cos\phi\sqrt{2\epsilon(1+\epsilon)}\frac{d\sigma_{LT}}{d\Omega} + \cos 2\phi\epsilon\frac{d\sigma_{TT}}{d\Omega} + \sin\phi h\sqrt{2\epsilon(1-\epsilon)}\frac{d\sigma_{LT'}}{d\Omega}$$

The transverse and longitudinal parts are the most straightforward parts to extract by integrating over phi and the helicity, this work will be limited to the TL part for time constraint reason but the complete extraction of the other terms will be done for the final results of the analysis.

6.8.1 Run selection

The third kinematic was taken from october 21st 2004 to November 7th 2004 and accounted for 255 runs. Out of this 255 runs a couple of them had problems with the calorimeter :

The run selection was based on beam quality, spectrometer and calorimeter parameters. A good parameter to check the quality of the data is the number of event normalized by the beam charge. Since all data taking condition are not supposed to change, this ratio should be constant. The normalization allows to eliminate beam current fluctuations. Also since the current was low at 2.5 μA there was no need to cut for the beam trips : we checked that target boiling are negligible at this current.

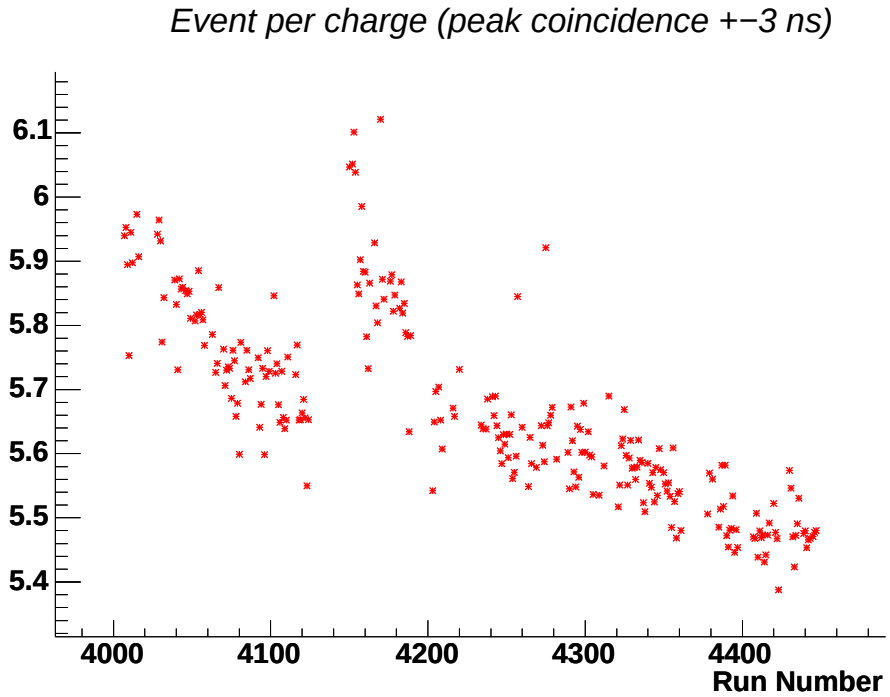

Figure 6.15: Number of events normalized by the beam current

As we can see in figure 6.15 the number of events by charge in the coincidence peak has a decreasing trend which is caused by the radiation damage of the calorimeter and has a mean value around 5.7. Since we preferred not to change any thresholds or High Voltage, the threshold was artificially increased as the blocks lost transparency. The jump around round 4150 was an attempt to cure the blocks using UV light but we see that the gain of transparency is only temporary and reached the same value after a couple of runs.

6.8.2 π_0 events selection

Spectrometer cuts

Acceptance The R-function are functions allow to easily parameterize complex shapes as sum of simpler shapes. This method was developed by M. Rvachev [75]. We used the implementation of the R-function by J. Lerose. It is presented in the form of a function taking as the parameters in the TRANSPORT convention [23]:

- θ is the vertical angle taking a positive value when pointing toward the floor
- ϕ is the horizontal angle in the spectrometer frame

$$r - functions(y, dp, \theta, \phi)$$

with

$$y = -vertex * \sin(ATan(kpx/kpz) \quad (6.9)$$

$$\theta = ATan(kp_y/\sqrt{kp_x^2 + kp_z^2}) \quad (6.10)$$

$$\phi = ATan(kp_x/kp_z) - \phi_{HRS} \quad (6.11)$$

$$dp = \frac{\sqrt{kp_x^2 + kp_y^2 + kp_z^2}}{p_{central}} \quad (6.12)$$

The spectrometer cut using the R-function was used on the real and simulated events.

Number of tracks in the VDC Events having multiple tracks in the VDC are removed since they can be ambiguous and lead to a bad electron reconstruction.

Number of tracks	Number of events	%
0	$1.53 \cdot 10^4$	1.54
1	$9.45 \cdot 10^5$	93.2
more than 1	$5.27 \cdot 10^4$	5.2

One track events represent 93

Calorimeter cuts After this data processing, the events were filtered through a set of cuts on the calorimeter to select the π^0.

A cut on the photon energies was set to 1.2 GeV to insure no threshold effects from the trigger affects the efficiency of photons detection.

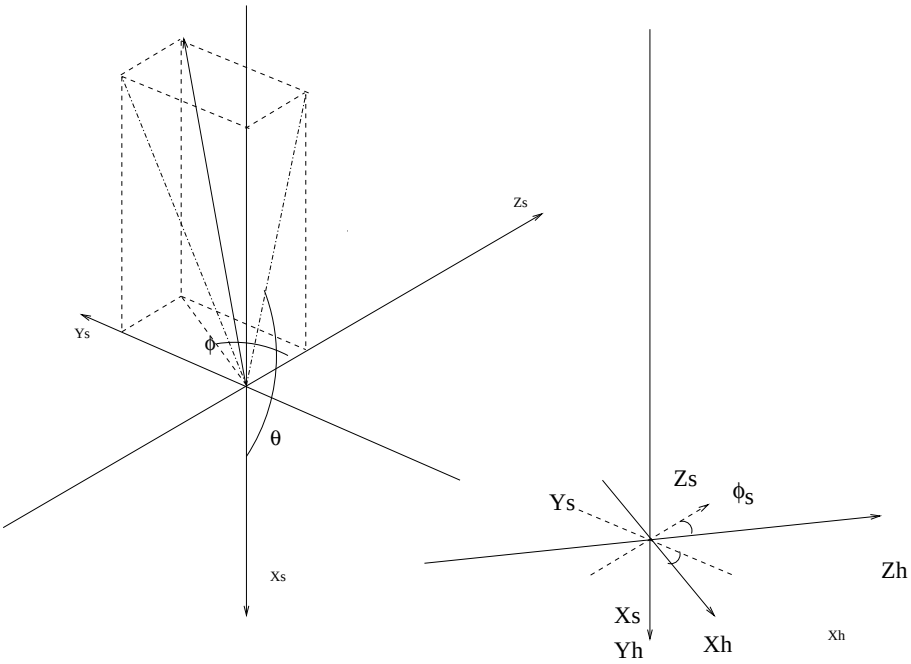

Figure 6.16: Spectrometer angle conventions

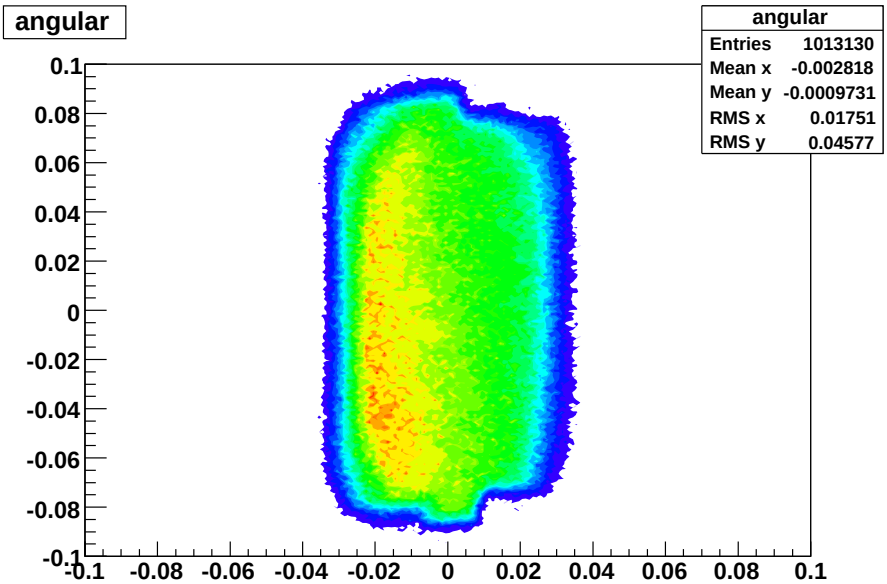

Figure 6.17: Electron angular distribution

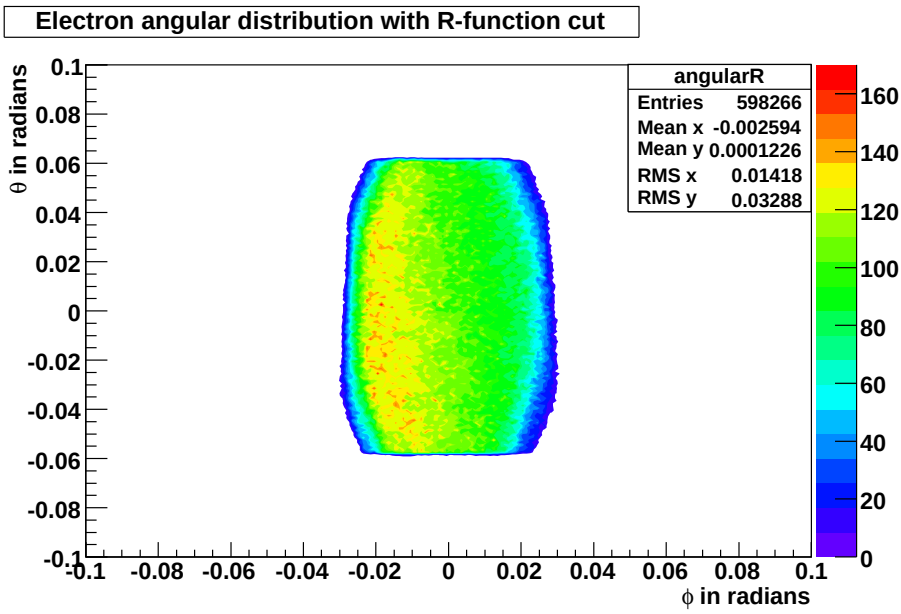

Figure 6.18: Electron angular distribution after R-function cut

We first made a cut on the calorimeter geometry allowing us to define accurately its acceptance and to eliminate events with energy leakage which could worsen the energy resolution.

We made a cut on $|(x_{calorimeter} + 1.5)| < 13.5cm$ and $|(y_{calorimeter})| < 15cm$ which corresponds to reduce the calorimeter by one block and a half (each block measuring 3cm x 3cm). Note that the calorimeter has a offset of half a block in the x-axis..

These cut reduced the statistics from $17 \cdot 10^6$ events to $2.6 \cdot 10^6$ In order to select the π_0 events we selected only 2 clusters events with a cut on the cluster amplitude. From the sample of the third kinematic with the cut events with 3 or more clusters represents 6.2 % compared to the number of events at 2 clusters giving the correction to be applied for the 2 clusters events lost.

Nb Clusters	kevents	%
1	2439	91
2	229.3	8.5
3	13.2	0.5
4 or more	1	0.04

Finally we used a symmetrization in order to preserve the right left symmetry around the virtual photon when studying the transverse and longitudinal part of

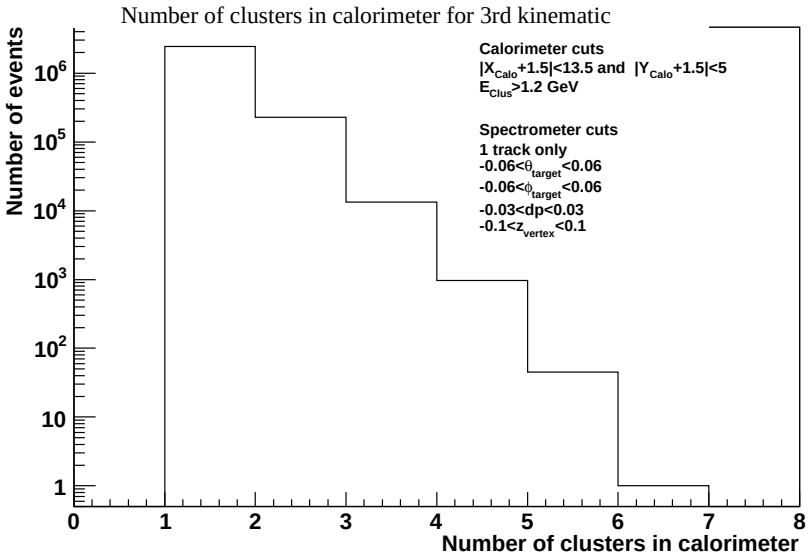

Figure 6.19: Number of clusters by event distribution

the cross section: it consists in reconstructing the virtual photon and to define a smaller calorimeter surface so that the calorimeter surface is symmetrical around the virtual photon making sure that the terms in cos ϕ cancels when integrating over phi.

6.8.3 Accidentals

Pion accidental analysis We want to study the pions from electroproduction.

$$e + p \rightarrow e' + p + \pi^0 \rightarrow e' + p + \gamma_0 + \gamma_1$$

The two photons are detected in the calorimeter. If we look at the invariant mass reconstructed from the two photons we clearly see the peak corresponding to the π^0 mass. The raw spectrum shows this peak above a background constituted of accidentals events and production of two pions.

This yields to different accidentals cases that have to be subtracted. The different case are illustrated by the plot of the time of one cluster versus the time of the other cluster on a [-10,10] time window 6.20. The different possible cases are

Number	Cuts	Events after cut	%
	No cuts	1013	100
0	vertex	963	95
1	calo x1	875	86
2	calo y1	789	78
3	calo x2	616	61
4	calo y2	566	56
5	time	515	51
6	dp	494	49
7	x col	438	43
8	y col	403	40
9	E1	182	18
10	E2	104	10.2
11	m	97	9.6
12	Q2	97	9.6
13	s	92	9.1
14	Rfun	45	4.5
15	Symmetrisation	37	3.7

Table 6.3: Number of events going through the set of given cuts

Those are summarized in the following table

electron	Real π_0	Acc π_0	γ real	γ acc		m_x^2	$m_{\pi_0}^2$	case
yes	yes					yes	yes	real
		yes					yes	π^0 acc
yes			yes	yes				acc coinc
yes			yes					acc acc
yes	yes			yes				Lost pions
yes	yes		yes					Lost pions

We made different treatment of the same data sample in order to determine the accidentals so that the normalization is the same for all the samples.

For the real π_0, events will be chosen if they have two cluster with the photons within at [-3,3][-3,3] ns window for all the photons.

For the π_0 accidentals, this is exactly the same analysis as for the real $\pi_0 events$ but shifted out of the coincidence peak. Events will be taken within in [3,9] ns window choosing the pions out of the coincidence window.

For the π_0 accidentals created by two uncorrelated photons in the calorimeter, we chose timing windows one in the coincidence peak [-3,3] and one out from the coincidence peak [5,11], the clustering was made on these two windows, giving a sample of two clusters events. To generate the background a cut on timing to

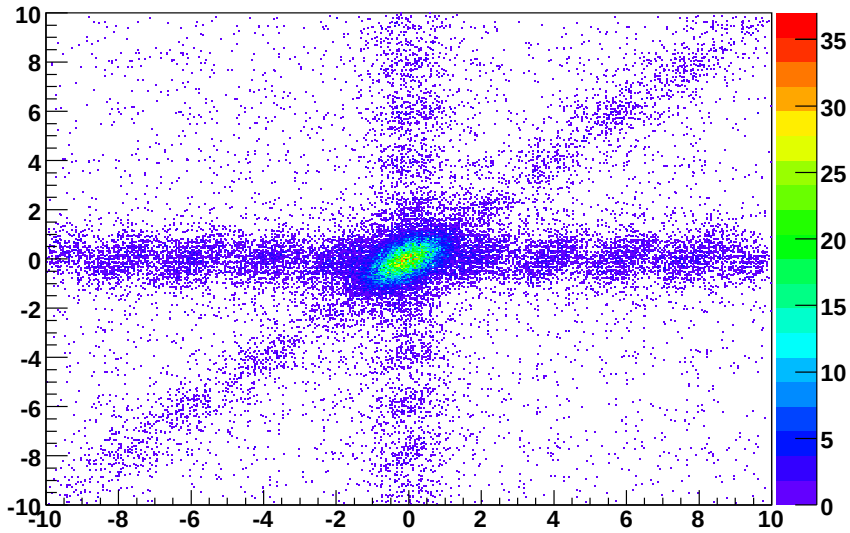

Figure 6.20: Arrival time of first cluster versus arrival time of the second cluster axis are in ns. We can see

choose one cluster in each time window was made.

Lastly we have the case where two photons not in coincidence timing window make an accidental We chose different timing windows : one in two different windows [-11,-5] and one out from the coincidence peak [5,11], the clustering was made on these two windows, giving a sample of two clusters events.

These cases are summarized in the plot 6.20 of the coincidence time of the second cluster as a function of the coincidence time of the first cluster.

6.8.4 More than two clusters events

Most of the 3 clusters events are likely to be a pion associated with a photon. So the number of two clusters events will be corrected for the cluster with more than two clusters.

The subtracted spectrum on invariant mass show the accidental subtraction is good but in order to extract the pion electroproduction cross section we need to deal with a physical background which is the ρ^+ production which disintegrates into :

$$\rho^+ \rightarrow \pi^+ + \pi^0$$

If we look at the missing mass spectrum we see that the one pion peak is polluted

by two pions events.

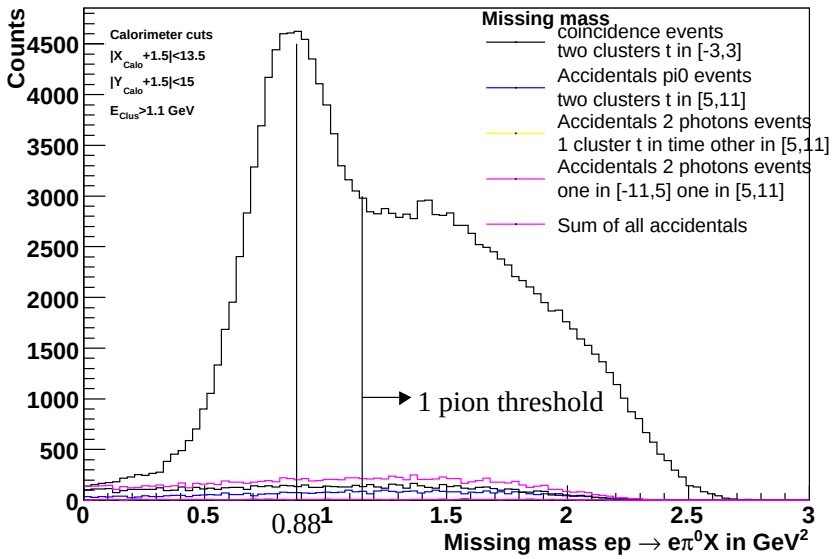

Figure 6.21: Missing mass of the reaction $ep \rightarrow e\pi^0 X$ with no background subtraction, one can see the different background contributions

After background subtraction,

6.9 Background identification and estimation

The reactions which can produce π^0 additional are ω production, rho production and Δ.

$$ep \rightarrow ep\omega \rightarrow ep$$

$$ep \rightarrow en\rho \rightarrow en\pi^0\pi^+$$

$$ep \rightarrow e\pi^0\Delta^+ \rightarrow ep\pi^0\pi^0$$

Requiring a high energy π^0 guarantees that this particle does not come for a resonance decay where the π^0 is a low energy one.

6.10 Extraction

In order to extract the exclusive π^0 we use the additional information given by the missing mass to disentangle the two processes. Experimentally we know :

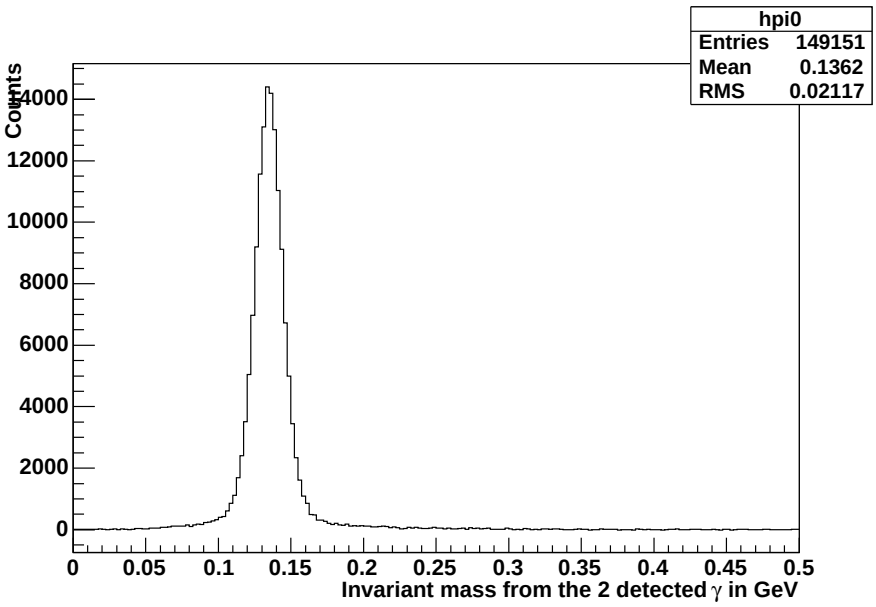

Figure 6.22: Invariant mass spectrum of the two photons in the calorimeter with subtracted accidentals

- the scattered electron $\vec{k'}$ from the spectrometer.
- the pion $\vec{q'} = \vec{q'}_{\gamma 1} + \vec{q'}_{\gamma 2}$ from the calorimeter and the vertex.
- the nominal energy of the accelerator k.

The raw cross sections we obtain this way are a convolution of the detectors resolutions and the radiative correction and mixes one pion and two pions reactions. In order to extract the crosssection at the vertex since all the theoretical predictions give cross section on the vertex variables, we used an extraction method allowing to deconvolute those effects and also to resolve the different channel which can produce π^0 by using the missing mass variable. We tried different assumption for the two pions reactions as mentioned formerly : first one with ρ production, ω production, Δ production and Δ and rho production. The best fit was obtained for the Δ production only so we can conclude that this is the biggest contribution of physical background :

$$\gamma p \rightarrow p + \pi^0$$

$$\gamma p \rightarrow \Delta^+ + \pi^0 \rightarrow p + \pi^0 + \pi^0$$

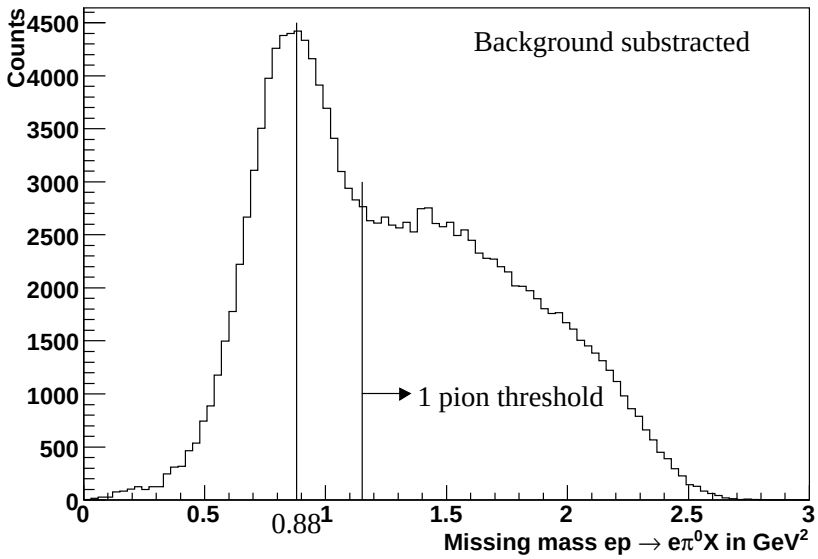

Figure 6.23: Missing mass of the reaction $ep \rightarrow e\pi^0 X$ with background subtraction

One can disentangle these two reactions using the missing mass : $ep \rightarrow e\pi^0 X$, for the exclusive DVCS we will have only a proton so a peak at the proton mass and the threshold for a second pion.

In order to take care of the acceptance, the resolution effects and the radiative correction we used a Monte-Carlo simulation.

6.11 Simulation

The simulation models the behavior of the detectors and of some of the observables associated to them. This allows to determine effects of correlations between variables and bin migration.

6.11.1 Event generation

The full geometry of the experiment detectors as well as the radiative correction were modelized into Geant 3.21. Electrons were drawn in the spectrometer acceptance and thereafter the pion or the Δ are created and decayed. Since the events are drawn in the spectrometer first the associated cross section for the simulated event samples is 1. The phase space factor $\Delta t \cdot \Delta xb \cdot \Delta Q2 \cdot \Delta phi_e$ is

also computed for each event this corresponds to the phase space where the event was drawn.

The simulation included :

- the HRS resolution on angle, momentum and vertex
- the trigger with a uniform threshold at 0.9 GeV

If we look at the vertex variables we see that the two processes are almost completely separated some protons going to higher missing mass because of radiative corrections. So if we can deconvolute the radiative corrections and resolutions effects we should be able to separate the two processes.

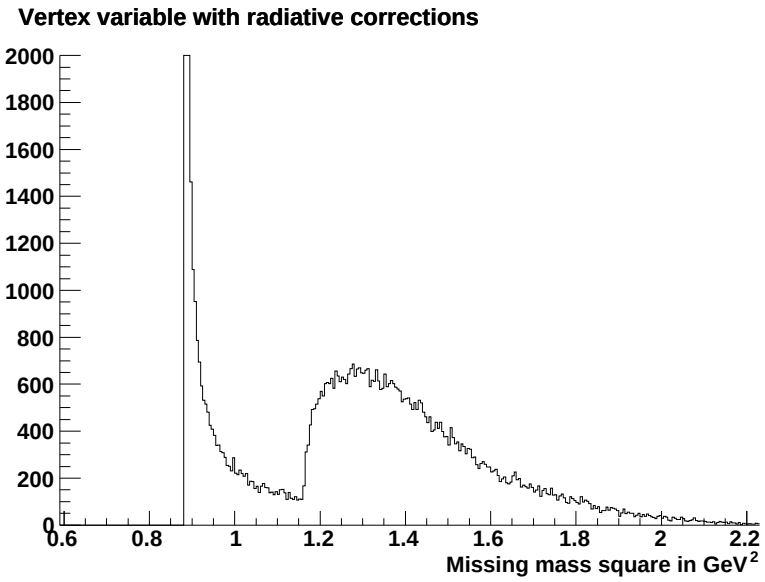

6.11.2 Resolution adjustment of the simulation

When comparing the reconstructed variables with the experimental data we saw some discrepancies. The invariant mass of the π^0 is too narrow 6.24 compared to the real events.

Calorimeter

The simulation did not indeed include some processes which can contribute to the resolution. In particularly

- photostatitics : the energy is randomly picked into a Gaussian centered on the energy and of width α which is the parameter set.

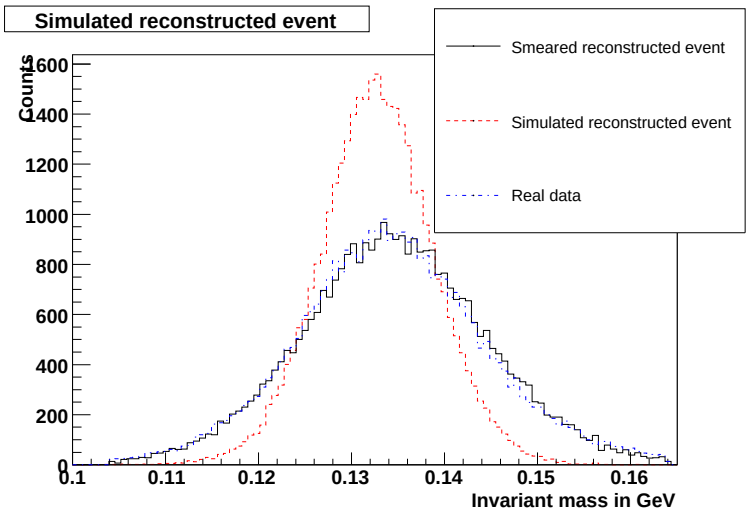

Figure 6.24: Pion invariant mass

- angular resolution
- leak coefficient : this is a multiplicative coefficient applied to all the components of the photons four-momenta

We put parameters corresponding to this smearing in order to fit the real events. One result we could already draw from the simulation was the dependence on the resolution effect of the correlation between the missing mass and the invariant mass.

So we added the correction for this correlation for both the real and smeared simulated events which corresponds to a rotation of the coefficient alpha center on the pion mass and missing mass squared. As we can see on 6.24 the smeared events and the real events fit almost perfectly for the following parameters :

Parameter	Value
E_{res}	$1.8 \cdot 10^{-3}$
Pos_{res}	3.5 mm
E_{leak}	1
$E_{leakSimu}$	1

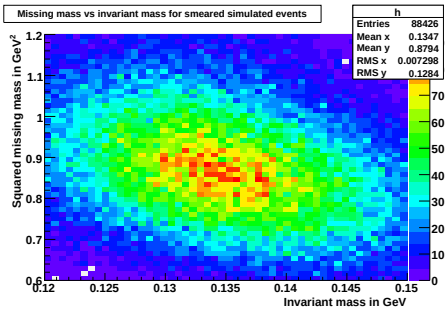

Figure 6.25: Missing mass vs pion invariant mass from simulation

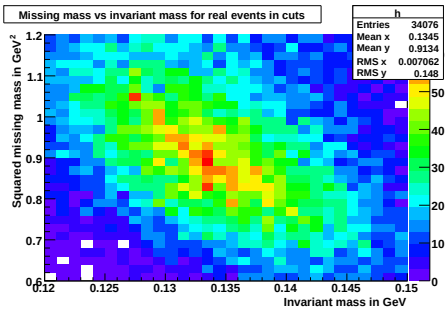

Figure 6.26: Missing mass vs pion invariant mass from data

6.11.3 Extraction method

The real data implies choosing a binning to analyze the data. So the quantity we actually study is the integral over the bin width of the differential cross section convoluted with the response of the detectors and the radiative corrections. To compare the experiment results with the theoretical models we need to extract the cross section in vertex variables. So we need to deconvolute the experimental measurement from resolution effects and radiative corrections. This comes to solve the following integral equation where $Y(i_e)$ is the number of counts for an experimental bin each experimental binbeing index by a single super-index i_e, x_v is the vector of vertex variables, x_{rad} is the vector of corresponding to radiative corrections variables independent from x_v and likewise x_res is the vector of resolution variables independent of x_v with the unknown $d\sigma(x_v)$

$$Y(i_e) = \mathcal{L}u \times \sum_{i_v=1,N_v} \int_{\Delta(i_e),\Delta(i_v)} d\sigma(x_v) \otimes Res(x_v, x_{res}) \otimes Rad(x_v, x_{rad}) dx_{res} \cdot dx_{rad} \cdot dx_v \tag{6.13}$$

here is the $\mathcal{L}u$ is the integrated luminosity.

In the same way that for the experimental data we define a binning for the vertex variable X:

$$X(i_v) = d\sigma(\bar{x_v}) \sim < d\sigma(x_v)) >_{i_v} = \frac{\int_{\Delta(i_v)} d\sigma(x_v) dx_v}{\int_{\Delta(i_v)} dx_v} \tag{6.14}$$

In this approximation we assume that the cross-section in a bin $\Delta(i_v)$ is replaced by the value $\bar{x_v}$ at the center of the bin. This is justified if the cross section a small second order derivative.

$$d\sigma(x_v) = d\sigma(\bar{x_v} + \epsilon) = d\sigma(\bar{x_v}) + \epsilon \frac{\partial d\sigma(\bar{x_v})}{\partial x_v} + \mathcal{O}(\epsilon^2) \tag{6.15}$$

In order to be able to take into account all the bins correlations, we put the all the bins into a vector using an arbitrary numbering defining N_e the total number of experimental bins and defining N_v the total number of vertex bins. This allows us to define a passage matrix we will call K from the two sets of bins.

$$Y_{exp} = KX_{vertex}$$

$$K(i_e, j_v) = \mathcal{F} \sum_{\mu=1,N_G} \int_{\Delta(i_e),\Delta(i_v)} Res(x_v, x_{res})) \otimes Rad(x_v, x_{rad}) dx_{res} \cdot dx_{rad} \cdot dx_v \tag{6.16}$$

K contains the different probabilities that a reconstructed variable bin has to be filled for a given vertex bin. This method allows to take into account all the correlations between all the variables.

The N_e equation system can be use to construct a χ^2

$$\chi^2 = \sum_{i_e=1,N_e} \frac{(Y(i_e) - \sum_{i_v=1,N_v} K(i_e, i_v) \times X(i_v))^2}{\sigma(i_e)^2} \tag{6.17}$$

By requiring the χ^2 to be minimal for each X_{i_v} value.

$$\begin{aligned} \frac{\partial}{\partial X_{i_v}} \chi^2 &= \frac{\partial}{\partial X_{i_v}} \left[\sum_{i_e=0}^{n_e} \left(Y_{i_e} - \sum_{i_v=0}^{n_v} M_{i_e i_v} X_{i_v} \right)^2 \right] \\ &= \sum_{i_e=0}^{n_e} \left[2 \left(Y_{i_e} - \sum_{j_v=0}^{n_v} M_{i_e j_v} X_{j_v} \right) M_{i_e i_v} \right] = 0 \end{aligned}$$

This yields N_v equations N_v unknowns

We define the matrix associated to the system :

$$U = MX$$

with

$$M_{ij} = \sum_{i_{e=0}}^{n_e} K_{i_e i} K_{i_e j}$$

with M a square matrix of dimension N_e. So we can obtain the vertex variables by simply solving the system by just inverting the matrix M.

The error matrix must satisfy $\partial\chi = 1$ which yield the the invert matrix is also the error matrix.

Passage matrix generation

The matrix is filled by scanning files of generated events one generation π^0 sample and one Δ sample. Each simulated event contains particles four-momenta at vertex and reconstructed. So for each of them the bin number i_v at vertex and in the reconstructed i_e is determined and the corresponding matrix element K(ie,iv) is incremented. In order to take into account the real flux of virtual photons we weighted each event by a normalization factor : event is weighted by the photon flux factor to get the flux of virtual photon from the flux of electrons :

$$\Gamma = \frac{\alpha K}{2\pi^2 |q^2|} \frac{E'}{E} \frac{1}{1-\epsilon}$$

with the convention corresponding to the real photon leading to the same final state where

$$K = s - M^2$$

and

$$\epsilon = 1 - 2\frac{\nu^2 - q^2}{q^2 \tan^2(\theta/2)}$$

multiplied by the space phase factor.

6.11.4 Extraction of TL part of the cross section

I remind the π^0 cross section :

$$\frac{d\sigma_\nu}{d\Omega_f dE_f d\Omega} = \frac{d\sigma_T}{d\Omega} + \epsilon\frac{d\sigma_L}{d\Omega} + \sqrt{2\epsilon(1+\epsilon)}\frac{d\sigma_{LT}\cos\phi}{d\Omega} + \epsilon\frac{d\sigma_{TT}}{d\Omega}\cos 2\phi + h\sqrt{2\epsilon(1-\epsilon)}\frac{d\sigma_{LT'}}{d\Omega}\sin\phi$$

For the angle and helicity independent part, The result allow to separate the contribution of pions produced by the the delta from the exclusive pions 6.27

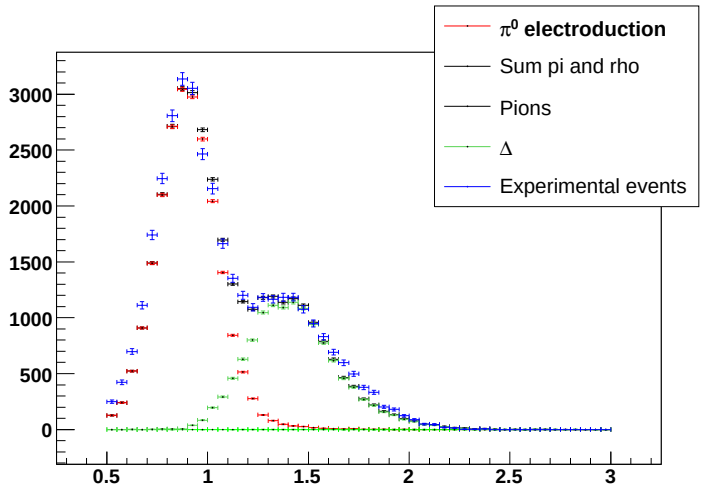

Figure 6.27: Missing mass squared $ep \rightarrow ep\pi^0 X$ in GeV^2

and the result of the t-dependence in counts to be compared with the real data and in cross sections.

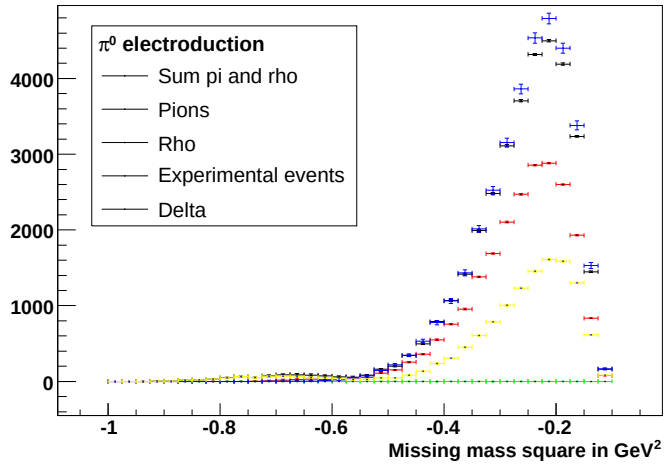

Figure 6.28: t distribution at vertex

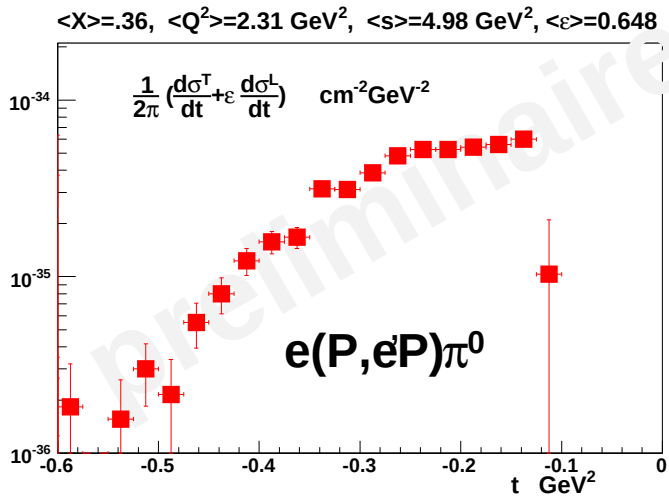

Figure 6.29: Pion electroproduction cross section integrated over ϕ as a function of t

Chapter 7

Conclusions and outlook

7.1 Experiment summary

Overall the experiment was successful. Nevertheless some parts which is common for a commissioning experiement leaving room for improvements for an experiment using the similar setup.

7.1.1 Proton array

The proton array as was the limiting factor for the experiment, it was the most sensitive to the DC current which prevented any current increase. The blocks at the smallest angle Additional shielding with a magnetic field would be a good solution to further reduce the low energy background and allow to go to higher luminosity.

7.1.2 Calorimeter

Even though the calorimeter was the closest from the beam line it performed much better than the proton array thanks to the lead fluoride and the PMT used. Nevertheless radiation damage of the calorimeter turned out to be very inhomogeneous : for a given angle from the beam,transparency variation were ranging from about 10% up to more than 50 % . If a testing method to identify which blocks would be more sensitive to radiation was developed this could improve the global radiation hardness of the calorimeter. The curability of the blocks has also to be studied. Gain monitoring was not very efficient since it was sensitive to the surface damage caused by low energy particle. Moreover the system failed at the beginning of the neutron run because of a position limit problem, so additionnal limit switches should be added to prevent such problems to occur again. With the different behavior of the blocks to the radiation a

continuous monitoring of the calorimeter gain using fibers or a physical process would be beneficial .

7.2 Mapping GPDs

The quark angular momentum can be computed knowing the E and H GPD. In order to have a complete description of the nucleon structure $\tilde{E}$ and $\tilde{H}$ have to be known and the full dependence on x_B and ξ has to be determined. To deconvolute the GPDs many different experiments are needed to be carried out in order to access the real and imaginary part of the amplitudes which will give access to a particular linear combination of GPDs. The extensive set of reaction allowing to access to the GPDs is given in section 6 of [13]. I will summarize what are giving some of these measurements in term of GPDs and will summarize the data that will be soon available on the different facilities.

7.2.1 DVCS cross section measurement

The cross section measurement of the DVCS gives the integral on the ξ variable of the GPDs. The higher the beam energy is the lower the BH cross section get making it possible to access directly the DVCS cross section. The Compass experiment will run a muon beam from 100 GeV or 190 GeV. It will have the advantage to cover a wide kinematical range and an energy where the BH is negligible compared to the DVCS cross section. This would allow the direct measurement of the DVCS cross section and Deep Virtual Meson Production at Q^2 where these reactions should be interpretable in terms of GPDs. An upgrade of the COMPASS detector [28] was proposed and this experiment would start after the completion of the COMPASS experiment around 2010 [3]. For lower beam energies the study of cross section could still be possible but would require a high luminosity. This kind of measurement could be carried on in Hall A the same setup with an additional magnet which could allow higher luminosities for measurement with photons going at larger angles where BH does not dominate too much over DVCS. The DVCS cross section could be obtained by subtraction of the BH. The same setup used for this experiment can be reused to make measurement at different Q^2. A letter of intent for a dedicated high luminosity was also submitted to PAC 27 [32] for a dedicated solenoid detector for the 12 GeV upgrade : it would add to the magnet and tracking an almost 4π calorimetry making it especially suitable for low cross section measurements.

7.2.2 Interference term measurement

The study of the interference is experimentally easier at lower energies. Asymmetries measurement can give informations and study of the interference term cross section can be eased by the BH process since the cross section of the interference term increase as the BH increases.

Cross section difference measurement

No other measurement are planned yet in Hall A though the same setup could be reused. Especially for the study of the neutron DVCS which is interesting since it is more sensitive access to the E GPD. The neutron experiment E03-106 [36] was accepted to run right after the proton DVCS experiment. Only one point out of the two were accepted, after completion of the analysis of the first data on the neutron, other kinematical points could be done. This kind of measurement would also greatly benefit of an increase in luminosity since neutron cross section is smaller than for the proton and the additionnal difficulty to detect the neutron.

Beam charge asymmetry

The beam charge asymmetry is the most direct way to access to extract the GPDs since the difference directly gives the interference term cross section. HERMES is still the unique facility to have the availability of a positron beam though. With its new recoil detector[59], HERMES will run until 2007. This will complete the former measurement of beam charge asymmetry

Beam single spin asymmetry

The beam single spin asymmetry is the most studied quantity since all the facilities have access to a polarized lepton source. The two strategies are the asymmetries measurement and the measurement of the interference term cross section. When the difference between two beam polarization is taken, only the DVCS and the interference term remains since BH does not depend on polarization in the case of the unpolarized target. Since the most of the measurements are taken where the BH dominates, the $|DVCS|^2$ can be neglected allowing to extract informations the imaginary part of the DVCS amplitude.

Hall B Hall B finished its data taking in 2005 and will have a additionnal run to complete the statistics. Since the usual trigger is on the electron and with the CLAS 4π capabilities. This data set can be used to study many different reactions in addition to DVCS such as meson production and Double DVCS though the statistical accuracy will be limited by the moderate luminosity. Hall B can work at

6 GeV on different type of experiments. The 4π detector capabilities is perfectly suited to study complex final states. Different experiments already measured ω [67] and on the ρ [47].

Hall B : CLAS++ The Hall B CLAS detector should be upgraded for the 12 GeV upgrade. Main improvements are in terms of luminosity up to $10^{35} cm^{-2} s^{-1}$. The upgrade plans also for a vertex detector and an inner calorimeter. The upgrade of Jefferson Laboratory at 12 GeV will have its kinematical coverage largely enhanced both in Q^2 and x_B. With its central detector combining vertex detection and calorimetry, it is very well suited to DDVCS studies and other complex final states, the only drawback is the luminosity which stays at $10^{-35} cm^{-2} s^{-1}$, which is the main justification for a dedicated high luminosity detector.

7.2.3 Double polarized experiments

Double polarized experiments are more powerful to extract the GPDs. According [13] part 6.1.8. experiment having both polarized beam and a longitudinal and transverse polarized target should be able to determine all 4 GPDs H,E,$\tilde{H}$,$\tilde{E}$. On the experimental side, polarized target have a couple of drawbacks :

- polarization can be high as but is most of the time moderate
- polarized target are often synonym of low luminosity
- transverse polarized target have a field perpendicular to the beam and thus can deflect the beam.

Polarized target

HERMES HERMES is also on pioneer on polarized target it features a gas target which can be polarized either longitudinally or transversely.

Hall B A proposal for the DVCS reusing the E01-113 setup was accepted. The experiment E05-114 [60] to study the DVCS using the Hall B amonia polarized target. The CLAS++ upgrade the option of a transverse target is mentioned too.

Recoil polarimetry

Another way to have a double polarized experiment is to study the recoil polarization of the proton. But so far recoil polarization is limited to small acceptances like the Hall A spectrometer FPP or HARP[1] detectors and efficiency of the polarimeters is usually lower than 10% [40], so an increase in luminosity and

construction of nearly 4π polarimeter would be needed. So DVCS with recoil polarimetry is not likely to be done in the near future but it is mentioned as an option in the dedicated detector Hall A forementioned where the high luminosity could compensate the low efficiency of the polarimeters.

Electron ion collider

A project of Electron Ion Collider is still planned in the DOE program but is not a priority right. The two project in are ELIC [63] which would be based in Jefferson or eRHIC at Brookhaven National Laboratory. The major advantage of this new machine would be a center but most important would be the luminosity which would be at least $10^{33} cm^{-2} s^{-1}$ and up to $10^{35} cm^{-2} s^{-1}$ with both beam polarized above 80%. This would be a major improvement in terms of luminosity compared to HERA. Compared to regular polarized target this has the advantage of a pure proton target and a very high proton polarization. Low energy background would not be a problem since not electronic atoms are present but like HERA the kinematical domain would be nevertheless limited to small x.

7.2.4 Deeply Virtual Meson production

One major task left with the GPDs measurement is the flavor decomposition Deeply Virtual Meson production results are very promising but measurement seems harder to be interpreted in terms of GPDs at current Jefferson Laboratory kinematics. Scaling seems to occur to higher Q^2 values than for DVCS : greater than $5GeV^2$ for the ω [67] and ρ [47]. Selecting a particular mesons also allow to select a particular flavor of GPDs [13] Part 6.3.5.

7.2.5 Double DVCS

Having a virtual photon in the final state gives an additional degree of freedom. Varying the virtuality of the outgoing photon allows to make measurement away from the line x=ξ. This require to detect a lepton pair in the final state so a reduction of the cross section by a fact $\frac{1}{137}$. Since Hall B took DVCS data on DVCS, it will be able to study the DDVCS at the same time using. But Double DVCS will be easier to study after the 12 GeV upgrade, with the new energy and the improved CLAS++ this would result in 5 folds increase in term of luminosity and a larger kinematical range. For the study of Double DVCS a high luminosity experiment could also compensate for the $1/\alpha$ reduction of the cross section.

7.2.6 Neutrino DVCS

With the multiplication of neutrinos experiments studying neutrinos oscillations such as KEK to Kamiokande in Japan, CERN to Gran Sasso and the NuteV[21] and MiniBoone[73] experiment at Fermilab. Neutrino flux are becoming higher and higher. And Deeply neutrino scattering as described in [7] might become feasible. The νDVCS is mentioned in the Minerνa program [8] and would accumulate about 10 000 of this kind of events in 4 year of data taking. This would allow to make the flavor decomposition of the strange quarks.

7.2.7 DVCS on nuclei

Studies of the DVCS on nuclei [14] could help to understand the transition between quarks and hadronic. Some results from HERMES using the PID capabilities could be interesting to study coherent DVCS or Deep Meson production on nuclei with a deuteron in the final state on a deuterium target.

7.2.8 Inverse DVCS : photo-production of lepton pairs

This process is :

$$\gamma p \rightarrow l^+ l^- p$$

according to [15] cross section should be of the order of a picobarn. This reaction could allow to access to the real part of the Compton amplitude at facilities having a photon beam. This kind of experiment could be run in Hall B and Hall D where tagged high energy real photons with high luminosity are available associated with detectors suitable to reconstruct the full final state.

7.3 Conclusions

The GPDs can be accessed in many different experiments this is extensively covered in chapter 6 of [13] and chapter 9 [29]. From this different method we can see that the access to the GPD E is a key issue in order to determine the and will require either double polarized experiments or experiments on the neutron which have the common problems of lower efficiencies either coming from the target polarization,recoil polarimeter or from the efficiency to detect neutrons and the smaller cross section. And in order to completely map the GPDs the DDVCS is the reaction to be considered. All of these processes thus either a low efficiency or lower cross section which constitutes a great challenge since experiments have to run at high luminosity associated with the need to detect complicated states with a good resolution. So are the difficulties that will have to

be overcome by the future experiments. This work showed that studying DVCS at high luminosity was possible after a lot of work in reducing and handling the background. In order to study the DVCS process, the π^0 background has to be understood and subtracted more over the Deep π^0 production can give access to the $\tilde{H}$ and $\tilde{E}$. The GPDs are a major reason driving the 12 GeV upgrade at Jefferson Laboratory so this experiment paves the way to another way of measuring the GPDs : a very high luminosity associated with a dedicated detector. The field would indeed benefits of a high luminosity dedicated detector indeed going from a 10^{35} to $10^{38} cm^{-2} s^{-1}$ can make the difference between a possible and impossible measurement and would open the ability for very low cross section process such as Double DVCS, DVCS with recoil polarization, neutron experiments.

Bibliography

[1] High acceptance recoil polarimeter. Given at CEBAF 1992 Summer Workshop, Newport News, VA, 15- 19 Jun 1992.

[2] Hydrogen technological survey thermophysical properties. National bureau of standards,US department of Commerce National technical information service.

[3] Outline for generalized parton distribution measurements with compass at cern. CERN-SPSC-2005-007.

[4] P. Achenbach et al. Radiation resistance and optical properties of lead fluoride cherenkov crystals. *Nucl. Instrum. Meth.*, A416:357–363, 1998.

[5] A. Airapetian et al. Measurement of the beam spin azimuthal asymmetry associated with deeply-virtual compton scattering. *Phys. Rev. Lett.*, 87:182001, 2001.

[6] J. Alcorn et al. Basic instrumentation for hall a at jefferson lab. *Nucl. Instrum. Meth.*, A522:294–346, 2004.

[7] Paolo Amore, Claudio Coriano, and Marco Guzzi. Deeply virtual neutrino scattering (dvns). *JHEP*, 02:038, 2005.

[8] Jeffrey A. Appel. Future hadron physics at fermilab. 2005.

[9] J. Ashman et al. An investigation of the spin structure of the proton in deep inelastic scattering of polarized muons on polarized protons. *Nucl. Phys.*, B328:1, 1989.

[10] O. Keith Baker et al. The high momentum spectrometer drift chambers in hall c at cebaf. *Nucl. Instrum. Meth.*, A367:92–95, 1995.

[11] M. Baylac et al. First electron beam polarization measurements with a compton polarimeter at jefferson laboratory. *Phys. Lett.*, B539:8–12, 2002.

[12] Maud Baylac. *Mesure de la polarisation du faisceau d'électrons du Jefferson Laboratory par effet Compton pour l'expérience de violation de parité HAPPEX en diffusion élastique électron-proton.* PhD thesis, Universite Lyon I - Claude Bernard, 2000.

[13] A. V. Belitsky and A. V. Radyushkin. Unraveling hadron structure with generalized parton distributions. 2005.

[14] E. R. Berger, F. Cano, M. Diehl, and B. Pire. Generalized parton distributions in the deuteron. *Phys. Rev. Lett.*, 87:142302, 2001.

[15] E. R. Berger, M. Diehl, and B. Pire. Timelike compton scattering: Exclusive photoproduction of lepton pairs. *Eur. Phys. J.*, C23:675–689, 2002.

[16] J. Berthot and P. Vernin. Beam energy measurement in hall-a of cebaf. *Nucl. Phys. News*, 9N4:12–16, 1999.

[17] Siegfried Bethke. Qcd studies at lep. *Phys. Rept.*, 403-404:203–220, 2004.

[18] J. D. Bjorken and Emmanuel A. Paschos. Inelastic electron proton and gamma proton scattering, and the structure of the nucleon. *Phys. Rev.*, 185:1975–1982, 1969.

[19] Martin Breidenbach et al. Observed behavior of highly inelastic electron - proton scattering. *Phys. Rev. Lett.*, 23:935–939, 1969.

[20] V. Breton et al. Application of neural networks and cellular automata to interpretation of calorimeter data. *Nucl. Instrum. Meth.*, A362:478–486, 1995.

[21] S. J. Brice. Miniboone. *Nucl. Phys. Proc. Suppl.*, 143:115–120, 2005.

[22] W. K. Brooks. Hadronic multi-particle final state measurements with clas at jefferson lab. *Spires e-print*, 2003.

[23] Karl L. Brown. A first and second order matrix theory for the design of beam transport systems and charged particle spectrometers. *Adv. Part. Phys.*, 1:71–134, 1968.

[24] D. S. Carman et al. The region one drift chamber for the clas spectrometer. *Nucl. Instrum. Meth.*, A419:315–319, 1998.

[25] A. Chantelauze. Master degree thesis report. www.jlab.org/ astrid, 2004.

[26] Bogdan Wojtsekhowski Charles Hyde-Wright, Alan Nathan. Exclusive compton scattering on the proton. Proposal PAC 16 http://www.jlab.org/exp_prog/proposals/99/PR99-114.pdf, 2000.

[27] John C. Collins. Proof of factorization for diffractive hard scattering. *Phys. Rev.*, D57:3051–3056, 1998.

[28] N. d'Hose, E. Burtin, P. A. M. Guichon, and J. Marroncle. Feasibility study of deeply virtual compton scattering using compass at cern. *Eur. Phys. J.*, A19:Suppl147–53, 2004.

[29] M. Diehl. Generalized parton distributions. *Phys. Rept.*, 388:41–277, 2003.

[30] D. Drechsel and L. Tiator. Threshold pion photoproduction on nucleons. *J. Phys.*, G18:449–497, 1992.

[31] F. Druillole et al. The analogue ring sampler: An asic for the front-end electronics of the antares neutrino telescope. *IEEE Trans. Nucl. Sci.*, 49:1122–1129, 2002.

[32] Charles E.Hyde-Wright. A solenoidal detector for deeply virtual compton studies at luminosities¿10. http://hallaweb.jlab.org/collab/PAC27/12GeV-solenoid.pdf, December 2004.

[33] James Harold Ely. Measurement of the single spin azimuthal asymmetry in the predominantly exclusive electroproduction of photons from the proton. 1997. UMI-30-57756.

[34] S. Escoffier et al. Accurate measurement of the electron beam polarization in jlab hall a using compton polarimetry. 2005.

[35] C.E Hyde-Wright F. Sabatie, P. Bertin. Proposal for deeply virtual compton scattering at 6 gev. Proposal PAC 18, 2000.

[36] E. Voutier F. Sabatie, P. Bertin. Deeply virtual compton scattering on the neutro. Proposal PAC 24, 2003.

[37] Pierre Bertin Fernando J. Barbosa. Results on the led pulser system for the hall a dvcs experiment. Internal note to be released, February 28th 2003.

[38] Gagik Gavalian. *Deply Virtual Compton Scattering Beam Spin asymmetry measurments with CLAS.* PhD thesis, University of New Hampshire, 2004.

[39] O. Gayou et al. Measurement of g(e(p))/g(m(p)) in e(pol.) p –¿ e p(pol.) to q**2 = 5.6-gev**2. *Phys. Rev. Lett.*, 88:092301, 2002.

[40] Olivier Gayou. *Proton form factors, measurement of the proton form factors ratio $\mu_p GE$*. PhD thesis, Universite Blaise Pascal, 2003.

[41] Murray Gell-Mann. Symmetries of baryons and mesons. *Phys. Rev.*, 125:1067–1084, 1962.

[42] K. Goeke, Maxim V. Polyakov, and M. Vanderhaeghen. Hard exclusive reactions and the structure of hadrons. *Prog. Part. Nucl. Phys.*, 47:401–515, 2001.

[43] Iwona Grabowska-Bold. Measurement of deeply virtual compton scattering using the zeus detector at hera. DESY-THESIS-2004-034.

[44] Jefferson Laboratory DAQ group. Coda user guide. ftp://ftp.jlab.org/pub/coda/docs/manual/coda1.4.ps.

[45] P. A. M. Guichon, L. Mosse, and M. Vanderhaeghen. Pion production in deeply virtual compton scattering. *Phys. Rev.*, D68:034018, 2003.

[46] P. A. M. Guichon and M. Vanderhaeghen. Virtual compton scattering off the nucleon. *Prog. Part. Nucl. Phys.*, 41:125–190, 1998.

[47] C. Hadjidakis et al. Exclusive rho0 meson electroproduction from hydrogen at clas. *Phys. Lett.*, B605:256–264, 2005.

[48] Cynthia Hadjidakis. *Electroproduction exclusive de méson vecteur ρ^0 à vitualité intermédiaire à Jlab avec le détecteur CLAS*. PhD thesis, Université Paris 7 DENIS DIDEROT, Jussieu, 2002.

[49] Gunther M. Haller and Bruce A. Wooley. A 700-mhz switched capacitor analog wave form sampling circuit. SLAC-PUB-6414.

[50] F. Halzen and Alan D. Martin. *QUARKS AND LEPTONS: AN INTRODUCTORY COURSE IN MODERN PARTICLE PHYSICS*. New York, Usa: Wiley (1984) 396p.

[51] R. Hofstadter and R. W. McAllister. Electron scattering from the proton. *Phys. Rev.*, 98:217–218, 1955.

[52] M. Iodice et al. The co-2 gas cherenkov detectors for the jefferson lab hall-a spectrometers. *Nucl. Instrum. Meth.*, A411:223–237, 1998.

[53] H. E. Jackson et al. A short-orbit spectrometer for hall c. Given at CEBAF 1992 Summer Workshop, Newport News, VA, 15- 19 Jun 1992.

[54] Ed Jastrzembski. The trigger supervisor. $ftp://ftp.jlab.org/pub/coda/docs/pdf/manuals/ts_manual.pdf$, June 1996.

[55] Ed Jastrzembski. Vme trigger interface version 2. ftp://ftp.jlab.org/pub/coda/docs/pdf/manuals/VmeTIRManual.pdf, May 1997.

[56] Xiang-Dong Ji. Deeply-virtual compton scattering. *Phys. Rev.*, D55:7114–7125, 1997.

[57] S. Nanda K. McCormick. A lead fluoride calorimeter for hall a. JLAB-TN-02-030 http://hallaweb.jlab.org/publications/Technotes/technote.html.

[58] P. Kozma, P. Kozma, and R. Bajgar. Radiation resistivity of pbf-2 crystals. *Nucl. Instrum. Meth.*, A484:149–152, 2002.

[59] Bernhard Krauss. Deeply virtual compton scattering and the hermes recoil-detector. DESY-THESIS-2005-008.

[60] A.Biselli et al L. Elouadrhiri, S.Niccolai. Deeply virtual compton scattering at 6 gev with polarized target and polarized beam using the clas detector. Proposal PAC 28, 2005.

[61] D. Lachartre and F. Feinstein. Application specific integrated circuits for antares offshore front-end electronics. *Nucl. Instrum. Meth.*, A442:99–104, 2000.

[62] M. Mazouz. Left arm s1 and s2 efficiency. Internal note to be released, February 25th 2005.

[63] L. Merminga and Y. Derbenev. Elic: A high luminosity and efficient spin manipulation electron-light ion collider based at cebaf. *AIP Conf. Proc.*, 698:811–815, 2004.

[64] M. D. Mestayer et al. Construction update and drift velocity calibration for the clas drift chamber system. *Nucl. Instrum. Meth.*, A367:316–320, 1995.

[65] M. D. Mestayer et al. The clas drift chamber system. *Nucl. Instrum. Meth.*, A449:81–111, 2000.

[66] Robert Michaels. Single arm trigger. http://hallaweb.jlab.org/equipment/daq/strig.ps, October 20th 2004.

[67] L. Morand et al. Deeply virtual and exclusive electroproduction of omega mesons. *Eur. Phys. J.*, A24:445–458, 2005.

[68] Ludyvine Morand. *Mesure de l'électroproduction de mésons omega à grand transfert d'énergie-impulsion.* PhD thesis, Université Paris 7 DENIS DIDEROT, Jussieu, 2003.

[69] Laurent Mossé. *Etude de la diffusion Compton Virtuelle dans le régime profondement inelastique pour le dispositif experimental a COMPASS.* PhD thesis, Université Paris-Sud XI, Orsay, 2002.

[70] Motorola. Mvme5100 single board computer installation and use. http://www.motorola.com/content/0,,5654,00.html, July 2003.

[71] Carlos Mu noz Camacho. *Diffusion Compton pronfondément virtuelle dans le Hall A au Jefferson Laboratory.* PhD thesis, Université Paris-Sud VI, 2005.

[72] Carlos Mu noz Camacho. *Diffusion Compton pronfondément virtuelle dans le Hall A au Jefferson Laboratory.* PhD thesis, Université Paris-Sud VI, 2006.

[73] Voica A. Radescu. Differential cross section results from nutev. 2004.

[74] A. V. Radyushkin. Scaling limit of deeply virtual compton scattering. *Phys. Lett.*, B380:417–425, 1996.

[75] Marat Rvachev. Effective use of jlab hall a hrs acceptance with r-functions. http://hallaweb.jlab.org/publications/Technotes/files/2001/01-055.ps.

[76] B. Seitz. The hermes recoil detector: A combined silicon strip and scintillating fibre detector for tracking and particle identification. *Nucl. Instrum. Meth.*, A535:538–541, 2004.

[77] Rainer Stamen. Measurement of deeply virtual compton scattering at hera. DESY-THESIS-2001-057.

[78] S. Stepanyan et al. First observation of exclusive deeply virtual compton scattering in polarized electron beam asymmetry measurements. *Phys. Rev. Lett.*, 87:182002, 2001.

[79] VITA. The vmebus handbook, fourth edition, 2005.

[80] Michel Garcon Volker Burkert, Latifa Elouadrhiri. Deeply virtual compton scattering with clas at 6 gev. Proposal PAC 19, 2001.

[81] Windriver. Vxworks user manual 5.3.1.

[82] Windriver. Vxworks 5.3.1 programmers guide, 2005.

RESUME Cette thèse décrit une expérience de Diffusion Compton Virtuelle dans le régime profondément inélastique (DVCS). Elle s'est déroulée de septembre à décembre 2004 dans le Hall A au Jefferson Laboratory. Un faisceau d'electrons polarisés de 5,757 GeV interagit avec une cible d'hydrogène liquide. L'électron diffusé, le photon réel produit et le proton de recul sont détectés respectivement par un spéctromètre de haute résolution, un calorimètre constitué de cristaux de fluorure de plomb, et un ensemble de scintillateurs. Ces deux derniers ont été conçus pour fonctionner à une luminosité élevée ($10^{37} cm^{-2} s^{-1}$) permettant de signer les événements DVCS sans ambiguité. Une électronique dédiée a été développée et mise en place : un système d'échantillonnage permettant de résoudre l'empilement de signaux parasites sur les signaux physiques, et un module de déclenchement basé sur la coïcidence électron-photon. Des données ont été enregistrées pour trois points cinématiques correspondant à trois valeurs de la masse du photon virtuel : $Q^2 = 1.5 GeV^2, 1.9 GeV^2, 2.32 GeV^2$. Les données de ce dernier point ont permis d'extraire un résultat préliminaire pour la section efficace d'électroproduction exclusive de π^0 sur le proton.

MOTS-CLES : Diffusion Compton Virtuelle profonde (DVCS), Distribution de partons géneralisées (GPDs) , Système d'échantillonnage, acquisition de données, calorimètre, fluorure de plomb (PbF2), Hall A, Jefferson Laboratory, pion, électroproduction, diffusion profondément inélastique

Summary The Hall A Deeply Virtual Compton Scattering (DVCS) experiment used the 5.757 GeV polarized electron beam available at Jefferson Laboratory and ran from september until december 2004. Using the standard Hall A left high resolution spectrometer three kinematical points were taken at a fixed $x_{bjorken} = 0.32$ value for three Q^2 values : 1.5 GeV^2, 1.91GeV^2, 2.32 GeV^2. An electromagnetic Lead Fluoride calorimeter and a proton detector scintillator array designed to work at a luminosity of $10^{37} cm^{-2} s^{-1}$ were added to ensure the exclusivity of the DVCS reaction. In addition to the new detectors new custom electronics was used : a calorimeter trigger module which determines if a electron photon coincidence has occured and a sampling system allowing to deal with pile-up events during the offline analysis. Finally the data from the kinematic at Q^2=2.32 GeV^2 et s=5.6GeV^2 allowed to get a preliminary result for the exclusive π^0 electroproduction on the proton.

Keywords : Deeply Virtual Compton Scattering (DVCS) , Generalized parton distributions (GPDs), sampling electronics, data acquisition, calorimeter, lead fluoride (PbF2), Hall A, Jefferson Laboratory, Deep Inelastic Scattering (DIS), pion, electroproduction